Outflow properties of Class I objects in Ophiuchus

Minor research project

Nienke van der Marel

Supervisors:
Dr. L. Kristensen, Dr. R. Visser and Prof.dr. E.F. van Dishoeck

July 2010

Abstract

We present a search for molecular outflows for Stage 1 sources in the Ophiuchus star forming region, in order to confirm the reliability of a new classification method for young stellar objects and to explore the outflow activity. With the HARP-B instrument at the James Clerk Maxwell Telescope, 17 sources were mapped in 2'x2' regions in ^{12}CO J=3-2. The broad line wings of this CO line are the tracers of molecular outflows. For 13 sources, molecular outflows were detected and energetic properties such as momentum fluxes were derived. The other sources were confused by outflows from nearby sources. The correlation between envelope mass and momentum flux, representing the outflow strength, was confirmed, implicating a decline of outflow strength with evolution. The well-known correlation of momentum flux with bolometric luminosity could however not be extended down to the three lowest luminosity sources ($L_{\rm bol} < 0.5 L_{\odot}$) in this study, for which the momentum flux remained constant. This implies that the accretion rate is not directly related to the outflow strength, as concluded in previous works. The distribution of the outflow directions suggests a scenario with star formation in two separately triggered events, propagating from the north west to the south east, as suggested by previous studies. The outflows were compared to studies of H_2 knots, Herbig Haro objects and disks, where available. In addition to the targeted sources, seven new outflows were found which could not be assigned to a young stellar object. In combination with submillimeter and Spitzer observations, candidate sources were selected.

1 Introduction

Molecular outflows are distinctive for the earliest phases of star formation. In this study we present the results of an outflow study of Class I objects in the star forming region Ophiuchus, in order to better understand the star formation process.

1.1 Star formation

Although people have been observing the stars for thousands of years, the understanding of their origin is actually much more recent. Only in the last century, after it was discovered that stars are not 'eternal' but are born, live and die afterwards, astronomers started to study the conditions and environments in which they form.

Star formation starts in the dense molecular clouds of gas and dust in the interstellar medium (e.g. Lada 1999). Parts of the clouds may contract gravitationally by small density perturbations and form substructure with clustered prestellar cores. During this contraction, the density increases until it is high enough for nuclear fusion to start: a star is born. Until the star enters the main sequence, the core or protostar is called a young stellar object (YSO). Observations of YSOs are significantly different from main-sequence star observations because of the surrounding gas and dust from which the YSO is and was formed. Dust in particular obscures the stellar core in the optical and reradiates the energy at longer wavelengths.

YSOs are generally divided into four classes, designated 0, I, II and III, primarily based on their spectral energy distribution (SED). These classes also roughly represent different phases in the YSO evolutionary track. In Class 0 and I the source is still deeply embedded and accreting mass from the surrounding envelope. YSOs from Class II and III are already pre-main-sequence stars, where the surrounding material has nearly disappeared and the source is visible in the optical spectrum. In Class II (also called the T Tauri stage or Herbig Ae/Be stage for more massive stars) the star is still surrounded by a gas-rich circumstellar disk, which turns into a gas-poor debris disk in the Class III phase. In the Class 0 and Class I phase the central core is still growing from the accretion of circumstellar material. Class 0 objects are distinguished from Class I in that they are more embedded and extincted, have much lower temperatures (typically tens of K versus several hunderds of K) and more collimated bipolar molecular outflows (next section, see also Arce & Sargent (2006)).

Observational classification is done with the observed infrared spectral slope, $\alpha_{\rm IR}$, from 2 to 24 μm or the bolometric temperature $T_{\rm bol}$. Details on the limiting values can be found in Greene et al. (1994). A fifth class has recently been introduced: the flat-spectrum source, which is basically the transition between Class I and Class II. Another, newer classification is based on ratios between $M_{\rm disk}$, $M_{\rm env}$ and $M_{\rm star}$ and is therefore relies on physical parameters instead of observational. This classification has been gradually introduced by e.g. Whitney et al. (2003) and Robitaille et al. (2006). The new classification is numbered Stage 0 to 3; Stage 0 and 1 contain the embedded sources, but do not correspond directly to Class 0 and I. Stage 1 sources are most problematic to uniquely identify, because $\alpha_{2-24\mu m}$ and $T_{\rm bol}$, used to classify Class I and II cannot distinguish edge-on disks from embedded sources or face-on embedded sources from T Tauri stars. This is due to confusion by an edge on disk or obscuration by foreground layers of the source (Crapsi et al. 2008; van Kempen et al. 2009c).

To aid classification of Stage 1 sources, this study focuses on bipolar molecular outflows, a prominent component of a Class 0 and Class I source (Andre et al. 2000).

1.2 Bipolar molecular outflows

Molecular outflows were, like many astronomical discoveries, detected by coincidence. In the first high-resolution observations of star forming regions, it was quite a surprise that outflow motions were measured near young stellar objects instead of the expected strong infall from the accretion process (Snell et al. 1980). The molecular outflow is actually bipolar, which is clearly visible by blue-shifted and red-shifted emission features. Infall occurs simultaneously, but because the velocity differences in the outflow are large over a much larger area, outflows are more easily detected (Bachiller & Tafalla 1999). Quadrupolar outflows are known as well, see e.g. Avery et al. (1990). The molecular outflow is the swept up gas along cavity outflow walls.

An important property of an outflow is its collimation (ratio between major and minor axes of the flow): Class 0 YSOs usually have highly collimated outflows, while outflows from Class I objects are much less collimated. The outflow of a Class 0 object follows the shape of the driving force, which is thought to be an optical jet or wind. Evolving further, the outflow angle will open up and the swept-up material slows down, as the driving force disappears (Arce & Sargent 2006). The outflow is therefore also an evolutionary parameter: outflows in Class 0 sources have proven to be much stronger than in Class I objects (Bontemps et al. 1996).

Another interesting property for the study of evolution is the ratio between infall (accretion) and outflow. Bipolar outflow models predict a direct proportionality between accretion and ejection which declines with evolution, $\dot{M}_{\rm jet}/\dot{M}_{\rm acc} \sim 0.1 - 0.3$ with $V_{\rm jet} \sim 100$ km s^{-1} (Bontemps et al. 1996).

Another morphological aspect is the spatial distribution of the gas inside the lobes: a cavity is visible in the lobe, strongly suggesting a wind pushing away material (Bachiller & Tafalla 1999). Outflows are generally thought to be driven by jets and wide angle winds (see also next paragraph). For high resolution observations, the flow angle can be measured and related to the age of the outflow (Richer et al. 2000).

The origin of the jets is still unclear. The correlation found between the bolometric luminosity $L_{\rm bol}$ and outflow force $F_{\rm CO}$ (Cabrit & Bertout 1992) suggests that a single mechanism is responsible for the production of the outflows. Energy is probably not conserved (it is radiated away), but momentum conservation does exist: momentum of the outflow equals the momentum of the invisible agent (wind) (Bachiller & Tafalla 1999). Outflows can carry away angular momentum that would otherwise prevent accretion (Hogerheijde et al. 1998). Several models are discussed by Arce & Sargent (2006) and Richer et al. (2000). A second correlation, between $L_{\rm bol}$ and $M_{\rm env}$, was interpreted as an evolutionary effect reflecting a progressive decline of outflow activity during the accretion phase (Bontemps et al. 1996). Outflows have significant influence on their environment, both the close environment (envelope and core) as well as the surrounding cloud. Shock chemistry provides new tracers for outflow properties as well (Bachiller & Perez Gutierrez 1997; Arce & Sargent 2006).

Molecular outflows are generally studied by spectral maps of low-J CO lines. The line wings, tracing the high-velocity CO material, represent the outflow material. CO is an excellent tracer of outflows because it traces the swept up gas at lower temperatures, while H_2 traces shocked gas with $T >$1000 K.

1.3 Ophiuchus

The ρ Ophiuchus molecular clouds are some of the nearest star forming regions and contain many Class I and II sources. The distance is 120±4 pc (Loinard et al. 2008). The cloud is divided into several filaments: main filaments L1688, L1689 and L1709 and complementary clouds L1712, L1729, L1740, L1744, L1755 and L1765. The filaments are further divided in CO "clumps", labeled with an R number, e.g. R27 to R52 can be found in L1709. Several isolated clumps do not belong to a Lynds filament, e.g. R1 to R20. Maps of these divisions can be found in Loren (1989). Furthermore, L1688 is divided into six regions: Oph-A to Oph-F. The large-scale structure with identification of clumps was first mapped by Loren (1989) with J=1-0 ^{13}CO emission. Loren estimated the total mass as 3050 $M_\odot$ and dimensions in the order of 10 pc. Tens of YSOs have been identified since (Wilking et al. (2008) and references therein).

1.4 Ophiuchus outflow studies

Class I outflows in Ophiuchus have been studied extensively and energetic properties have been derived for many sources. Ophiuchus is a star forming region where most of the star formation is not isolated, but clustered. Therefore the YSOs (and their outflows) are very close together and may even be overlapping along the line of sight. In the next paragraph we give a chronological overview of outflow studies in Ophiuchus, in the second paragraph additional studies of the YSOs in Ophiuchus are listed.

Bontemps et al. (1996) performed a large survey study of the ^{12}CO 2-1 line of Class 0 and Class I YSOs in Ophiuchus, Taurus and Perseus, from our sample (see Section 2) Elias 29, IRS 43, IRS 44, WL 6 and WL 12, and assigned an outflow status to all of these except WL 6. However, this outflow status for WL 6 was assigned later (Sekimoto et al. 1997) with ^{12}CO 2-1 and ^{12}CO 1-0 lines in a study of X-ray emitting protostars, also including Elias 29, IRS 44 and IRS 46 and Class II source WL 10. Kamazaki et al. (2001) discovered an outflow for the intermediate Class I-II source CRBR 2324.1-1619 near GSS30 with ^{12}CO 1-0 observations, and further extended this with ^{12}CO 3-2 observations of outflows, also for VLA 1623 (Class 0) and Elias 32 (Kamazaki et al. 2003). Ceccarelli et al. (2002) and Boogert et al. (2002) extensively studied and modeled the outflow and envelope properties of Elias 29. Bussmann et al. (2007) mapped a much bigger region around Elias 29 in ^{12}CO 3-2 and discovered an outflow for LFAM 26 as well. Gurney et al. (2008) observed nine sources in Ophiuchus (e.g. Elias 33 and GSS 30) in rotational transitions of ^{12}CO, ^{13}CO, C^{18}O and C^{17}O, determined several outflow and infall properties, and produced contour maps. Zhang & Wang (2009) used data from IRAC observations and ^{13}CO 1-0 emission data from the FCRAO telescope in order to study the spatial distribution of young stellar objects and outflows in Ophiuchus and concluded that most of the mid-infrared outflows are concentrated in the L1688 dense core region and that star formation is propagating from the northwest to the southeast in the cloud. Earlier outflow studies for Ophiuchus, between 1989 and 1991, were summarized (Cabrit & Andre 1991) but none of the observed Class I sources could be assigned an outflow status due to low spatial resolution observations.

Additional information on the sources from earlier studies can be found in several publications. Many of these are summarized in Wilking et al. (2008), but some are listed here in particular. Van Kempen et al. (2009c) used HCO$^+$ 4-3 and C^{18}O 3-2 lines, 850 μm dust maps and 350 μm maps together with $\alpha_{\rm IR}$, $L_{\rm bol}$ and $T_{\rm bol}$ to infer $N_{\rm H_2}$, masses and evolutionary stage. They also included data on the foreground layers of five sources including LFAM 26, IRS 44 and IRS 37. Leous et al. (1991) observed several sources in free-free emission (6 cm) and calculated the flux $S_{\rm 6cm}$, which is related to the ionized wind of the jet, forcing the molecular outflow (Cabrit & Bertout 1992). Jørgensen et al. (2009) observed the HCO$^+$ 3-2 and HCN 3-2 lines and 1.1 mm continuum with the SubMillimeter Array for e.g. WL 12, Elias 29, IRS 43, IRS 54 and IRS 63 at much higher spatial resolution in order to obtain information on the disks and the envelope and compare it with model results. Beckford et al. (2008) studied 20 sources in the near infrared for polarization, amongst other Elias 29, 32 and 33, IRS 43, 44, 54 and 63 and WL 3 and 6. Andre & Montmerle (1994) observed young stellar objects of Class I, II and III in Ophiuchus (from our sample GSS 30, WL 6, WL 12, WL 17, IRS 37, IRS 43, IRS 44, IRS 54 and RNO 91) in 1.3 mm continuum and calculated their circumstellar masses in order to better understand the evolution process. Furuya et al. (2003) observed e.g. Elias 29, WL 6, IRS 43, IRAS 16253-2429 and IRS 63 in a multi-epoch 22 GHz H_2O maser survey and concluded that H_2O maser emission can be used as a probe for protostellar jets, although they are more closely related to 100 AU scale thermally ionized jets than to the 10^4 to 10^5 AU scale CO outflows.

1.5 Goals

In this report, the molecular outflows for the Stage 1 sources as classified by van Kempen et al. (2009c) in Ophiuchus are studied with high-resolution ^{12}CO 3-2 observations. For about half of these sources bipolar outflows have been detected in previous works, but not with the high spatial resolution from the new HARP-B array receiver at the JCMT. One of the goals is to determine whether all of these embedded sources show outflow activity. This would confirm the reliability of the new classification method and in general explore the earliest phases of star formation. In particular the physical properties of these outflows will be studied and plotted versus envelope mass and bolometric luminosity, in order to analyse the effect of lower envelope masses and lower luminosities on the outflow strength. Furthermore, the outflows will be compared with other outflow studies, with recently published disk studies, star formation direction and triggering, and studies of Herbig Haro objects and H_2 knots, further refining the processes involved in molecular outflows. The outline of the report is as follows. In Section 2 and 3, the sample selection and observations are presented. The actual data reduction is discussed in Section 4. Section 5 present the results, including the physical properties of the outflows. The implications on outflow evolution, classification and star formation activity in Ophiuchus are discussed in Section 6. The main conclusions are summarized in Section 7.

2 Sample selection

Of the known YSO population in Ophiuchus, 17 objects were selected for our sample. Out of the complete sample selection of van Kempen et al. (2009c) of 41 sources with potential Class I classification ($\alpha_{2-24\mu m} > 0.3$ and $T_{\rm bol} < 650$ K), only 17 were identified as truly embedded sources, from which four were actually classified as late Stage 1. These sources (IRS 63, IRS 54, WL 6 and WL 17) are in transition to the T Tauri Stage 2 phase because they have little envelope left ($M_{\rm env} \sim 0.05 M_\odot$). Van Kempen et al. (2009c) used a new classification based on molecular emission of HCO^+ 4-3 and $C^{18}O$ 3-2, with HCO^+ tracing dense gas in the inner regions of protostellar envelopes and $C^{18}O$ tracing the nearby environment including foreground layers. In combination with continuum dust emission, van Kempen et al. (2009c) set limits for Stage 1 and 2. Note that IRAS 16253-2429 was erroneously named IRAS 16285-2355 in van Kempen et al. (2009c). In addition RNO 91 was included, which is known as a T Tauri star with an extended outflow (Arce & Sargent 2006). Except for RNO 91 and IRS 63, all sources are located in the L 1688 ridge. The final source sample can be found in Table 1 and in Figures 1 and 2. In these maps, the 850 μm SCUBA map is used as background. The outflows as observed in this study are indicated by blue and red arrows (blue and red lobes). We also found 7 outflows which could not be assigned to any of the sample sources. These outflows are named UFO (unidentified flowing object) throughout this study and indicated on the map. The positions as found in van Kempen et al. (2009c) were used where available. For RNO 91, the coordinates from Arce & Sargent (2006) were taken. IRS 46 was not listed in Table 1, since it was classified as Stage 2. Since an outflow was detected for this source, it was added to the sample afterwards.

3 Observations

3.1 Gas line ^{12}CO 3-2 maps

All sources in the sample were observed in the J=3-2 line of ^{12}CO (345.796 GHz) with the HARP-B instrument at the James Clerk Maxwell Telescope (JCMT). The high spectral resolution mode of 0.026 km s^{-1} of the ACSIS back-end was used. The velocity range around the central frequency was -50 to +60 km s^{-1}. The observations were carried out at 17th, 19th and 20th June 2008 under weather conditions with an atmospheric optical depth $\tau_{\rm 225GHz}$ ranging from 0.073 to 0.12. The unreduced spectra had a typical rms noise of $\sigma_{\rm rms}$ = 0.4 K in 0.1 km s^{-1} bins. The sources were mapped in 2'x2' regions by 16 receivers arranged in a 4x4 pattern to capture the full extent of the outflows. The fields were mapped with the jiggle position switch observing mode resulting in 15″ spatial resolution. The maps were resampled with a pixel size of 7.5″. A position switch of 60′ or 150′ was used. For the sources observed at June 19th, the reference off position accidentally coincided with emission, resulting in negative absorption peaks in the spectra. The Class 0 source IRAS 16293-2422 was used as a line calibrator. The main-beam efficiency was taken as 0.7 and pointing errors were within 2″. Two receivers were broken at the time of observation, resulting in lack of data in the south east corner and the north north west (see also the velocity color maps in Figure 3; the pixels without data are shown

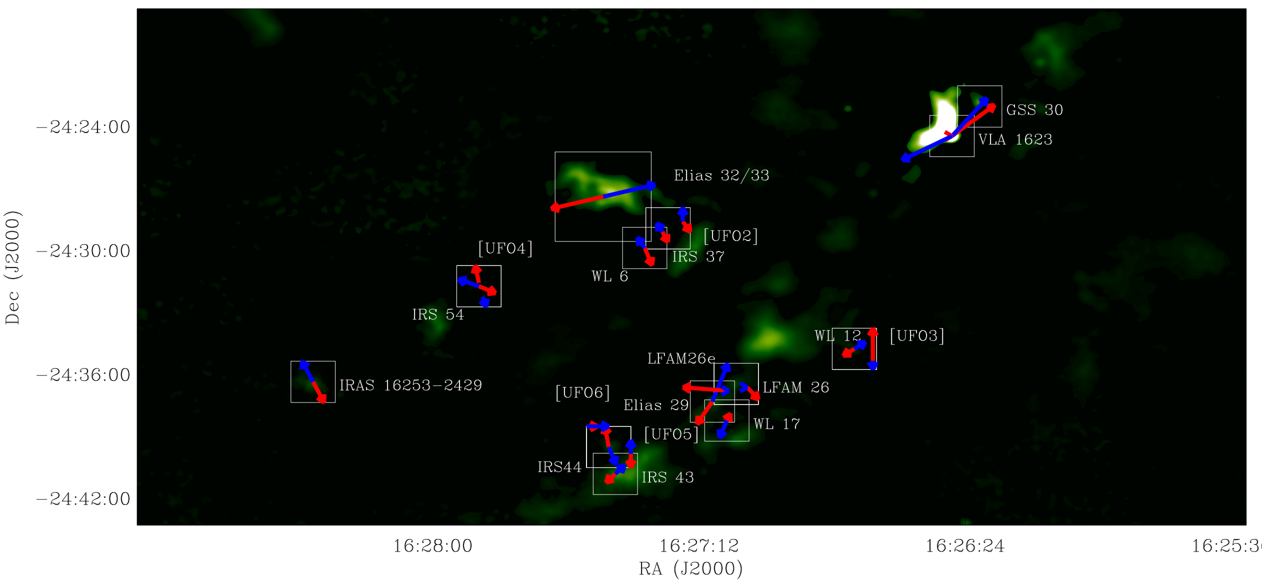

Figure 1: The L1688 core in Ophiuchus. In the background the 850 μm SCUBA map (Johnstone et al. 2000; Di Francesco et al. 2008) is shown. The locations of all observed maps are shown by white squares, labeled with the sources within. The blue and red arrows indicate the direction and extent of respectively the blue and red outflow of that source. UFOs (newly detected outflows without a driving source) are drawn as well. The extent of VLA 1623, as observed by Yu & Chernin (1997) is indicated.

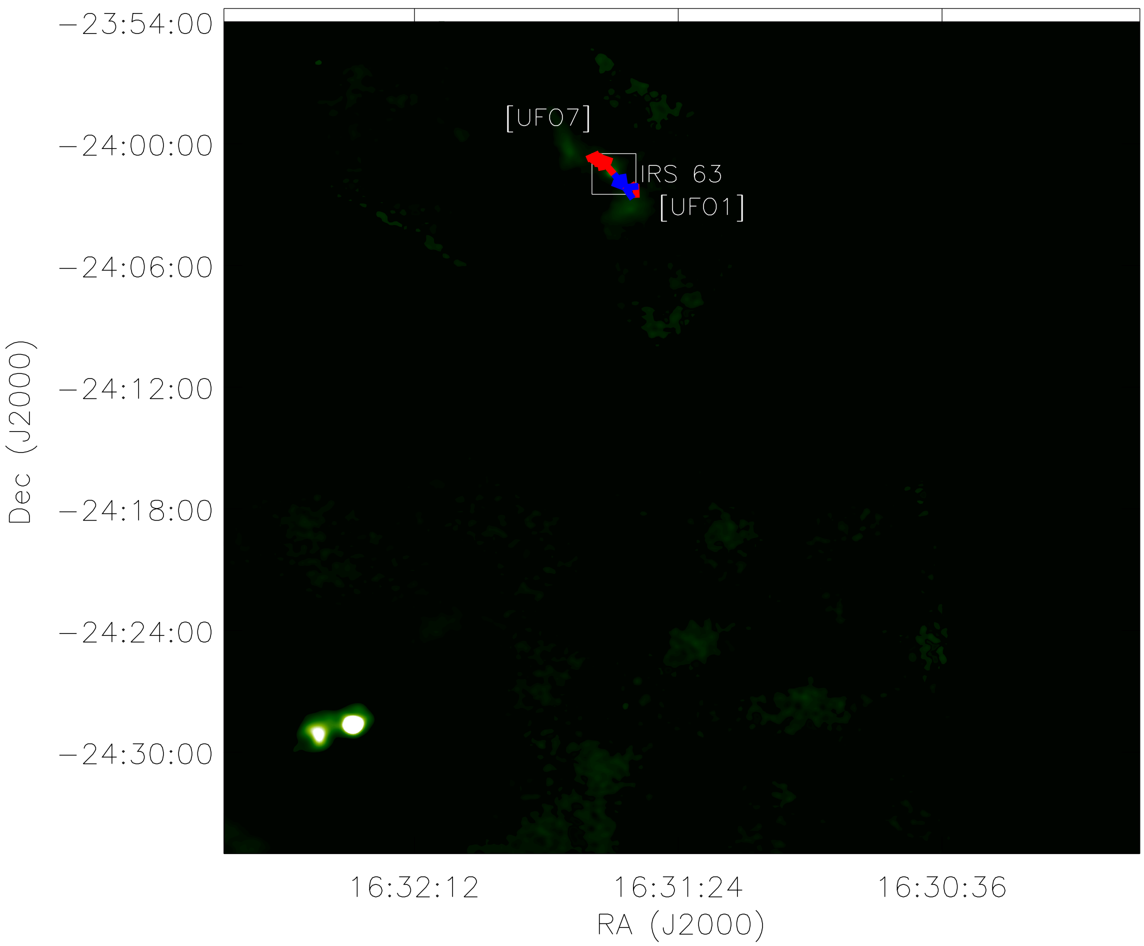

Figure 2: The environment of IRS 63. In the background the 850 μm SCUBA map (Johnstone et al. 2000; Di Francesco et al. 2008) is shown. The location of the observed map is shown by a white square. The blue and red arrows indicate the direction and extent of respectively the blue and red outflow of the source. The UFO is drawn with narrower arrows and labeled as well.

Table 1: Sample of Stage 1 sources in Ophiuchus.

Source	Alternative names	Coordinates (J2000)	
		RA	Dec
GSS 30-IRS1	GSS 30,Elias 21	16:26:21.4	-24:23:04.1
GSS 30-IRS3	LFAM 1	16:26:21.7	-24:22:51.4
WL 12	GY 111	16:26:44.0	-24:34:48
LFAM 26	GY 197,CRBR 2403.7	16:27:05.3	-24:36:29.8
WL 17	GY 205	16:27:07.0	-24:38:16.0
Elias 29	WL15,GY 214	16:27:09.6	-24:37:21.0
IRS 37	GY 244	16:27:17.6	-24:28:58
WL 3	GY 249	16:27:19.3	-24:28:45
WL 6	GY 254	16:27:21.8	-24:29:55
IRS 43	GY 265,YLW 15	16:27:27.1	-24:40:51
IRS 44	GY 269	16:27:28.3	-24:39:33.0
Elias 32	IRS 45,VSSG 18	16:27:28.6	-24:27:19.8
Elias 33	IRS 47,VSSG 17	16:27:30.1	-24:27:43
IRS 54	GY 378	16:27:51.7	-24:31:46.0
IRAS 16253-2429		16:28:21.6	-24:36:23.7
IRS 63	GWAYL 4	16:31:35.7	-24:01:29.5
RNO 91		16:34:29	-15:47:01

black). Some sources are separated by less than 30″ and therefore mapped in a single image. This is the case for Elias 32 and Elias 33, IRS 37 and WL 3 and GSS30-IRS1 and GSS30-IRS3, IRS 44 and IRS 46, respectively. Only for the latter case the two sources could be analyzed separately, due to the small separations. In addition, RNO 91 and Elias 33 were observed in February and September 2007 respectively with HARP-B, in the raster position switch observing mode. These sources were mapped in 4′x4′ regions. The maps were resampled with a pixel size of 12″ because many pixels in the original image contained no data. Along the edges many resampled pixels still contain no data, shown in black in Figure 3. Atmospheric optical depth values were 0.09 for RNO 91 and 0.05 for Elias 33. The rms noise $\sigma_{\rm rms}$ for the unreduced spectra was 0.35 and 0.2 K for 0.026 km s^{-1} bins, respectively.

3.2 Additional data

For the majority of the sample HCO^+ 4-3 and $C^{18}O$ 3-2 spectra from the central source position were obtained from the data set used by van Kempen et al. (2009c). These observations were carried out with the HARP-B and RxB receivers at the JCMT. The RNO 91 HCO^+ and $C^{18}O$ spectra were obtained from the JCMT data archive (not previously published). The 850 μm continuum data of the Ophiuchus region, obtained within the scope of the COMPLETE project using the SCUBA instrument on the JCMT were used for the overview map in Figure 1 (Johnstone et al. 2000; Di Francesco et al. 2008).

4 Data reduction and methods of analysis

4.1 First reduction

Each dataset for each source contained 16x16 CO spectra, in a 2′x2′ map. Data were reduced using the STARLINK package GAIA, CLASS and IDL. All spectra are baseline subtracted with baseline polynomials up to degree 2 in the spectrum outside the window [-20,20] km s^{-1}. For GSS 30 the baselines were subtracted outside the window [-20,40] because of a high-velocity feature (~ 28 km s^{-1}) in the spectrum. All spectra were binned to a velocity resolution of 0.11 km s^{-1} to decrease the rms noise level to typical $\sigma_{\rm rms}$ values of 0.19 K, using Hann smoothing.

4.2 Line wings and integration limits

Ophiuchus is more complicated than other nearby star forming regions, due to presence of multiple clouds and sheets with gas velocites within a few km s^{-1}, studied by van Kempen et al. (2009c). The spectra show a broad central profile around 4 km s^{-1}, resulting from the envelope emission, and extended line wings at the outflow positions. The most relevant characteristic of the spectral profile for this study are these line wings at the red and/or blue side of the central profile, since they are tracing the outflow material. Line wings were detected in all spectral maps. First, we made outflow maps of the integrated CO wing emission in blue-shifted and red-shifted velocity intervals. The integration limits are given in Table 2 and were derived as follows (Hogerheijde et al. 1998). The outer limits for the red and blue wings respectively are defined as the maximum velocity where the signal is still above the $\sigma_{\rm rms}$ level. Color maps showing these velocities can be found in Figure 3. These maps already give a very good indication of the location and extent of the outflow. Per source, the highest velocity values for blue and red respectively are taken as the outer integration limits for the whole map. The inner limits for red and blue respectively are derived from the ^{12}CO 3-2 position-velocity diagrams in Figure 4. In these plots, the spectra are plotted in contour as function of position, with the position along the outflow direction, based on visual inspection of the outflow maps. Contours are drawn at $3\sigma_{\rm rms}$ intervals, starting at $\sigma_{\rm rms}$. The vertical bar structure shows the general velocity profile of the envelope, while the spectra with wings are shown by the high velocity 'bumps' along the bar. The edges of the vertical bar are taken as the inner integration limits, since these are the velocities where the outflow emission blends in with the envelope emission. In the lower right corner the outflow direction or position angle is given, which is defined as the angle between the line from south to north through the center and the outflow axis, measuring from north to east (Arce & Sargent 2006). These values are also listed in Table 5. No position-velocity diagrams were made for GSS 30, Elias 33 and RNO 91. The GSS 30 map showed only outflow activity from the nearby Class 0 source VLA 1623 (see next section) and the outflows of Elias 33 and RNO 91 covered the entire map, so that a cut through the outflow direction would not show the inner limits of the envelope profile. The GSS 30 spectra show a very high velocity emission feature at 28 km s^{-1} next to the red wing in the central southern part of the spectral map. In five maps, new bipolar outflows which could not be assigned to IR sources were detected. In this report they are named UFO (unidentified flowing object) and further discussed in Section 6.6.

Integration limits were derived for these UFOs with the same method as described above. For some of the maps, other off-source spectra were used than those along the outflow direction, because the originals would show emission from other sources or odd emission. Since the wings often blend in with the envelope emission, the integrated intensities may overestimate the actual outflow emission. A thorough analysis, where the central profile was fitted by a Gaussian and subtracted before integration, shows that for all sources this difference is usually within a factor 1-1.5 and in a few cases still no more than a factor 3.0, so within our error margins as discussed in Section 5.5. Bontemps et al. (1996) used in their analysis of ^{12}CO 2-1 spectra a subtraction method by averaging the off-source spectra over a circle outside the outflow and subtracting this mean from each outflow spectrum. The spatial differences in the spectral profiles of our data are too large to properly use this method, because of the presence of foreground layers and nearby presence of other sources.

The outflow maps are presented in Figure 7. The maps have a pixel size of 7.5″, except for the maps Elias 33 (RASTER) and RNO 91 (RASTER), which have a pixel size of 12″ and are also larger. Con-

Table 2: Integration limits, σ levels and v_{LSR} as determined from HCO^+ emission.

Source	$v_{\rm source}$ (km s^{-1})	$\sigma_{\rm rms}$ (K)	Blue limits (km s^{-1}) outer	inner	Red limits (km s^{-1}) inner	outer	σ_{blue} (K km s^{-1})	σ_{red} (K km s^{-1})
Elias 29	4.6	0.21	-4.1	1.4	7.0	11.3	0.19	0.17
Elias 33	4.5	0.20	-6.6	1.3	5.8	9.9	0.22	0.16
GSS 30	4.6	0.17	-9.5	1.0	6.0	30.3	0.22	0.33
IRAS 16253-2429	4.0	0.22	-1.3	0.6	6.0	9.2	0.12	0.15
IRS 37	4.2	0.18	-1.4	0.7	6.2	8.0	0.10	0.09
IRS 43	3.8	0.27	-3.8	0.2	6.3	10.6	0.21	0.22
IRS 44	3.8	0.18	-4.3	0.0	7.0	16.6	0.15	0.22
IRS 46	3.8	0.18	-3.4	0.5	6.5	10.2	0.13	0.13
IRS 54	4.1	0.16	-7.1	1.3	7.0	12.2	0.18	0.14
IRS 63	2.7	0.20	-7.0	1.3	4.2	6.7	0.22	0.12
LFAM 26	4.2	0.18	-4.4	1.3	7.0	11.2	0.17	0.14
RNO 91	0.5	0.19	-9.4	-0.6	2.0	5.0	0.22	0.13
WL 6	4.0	0.21	-3.0	0.6	6.2	14.3	0.16	0.23
WL 12	4.3	0.24	-2.0	1.5	6.2	9.9	0.18	0.18
WL 17	4.6	0.17	0.0	1.2	7.0	9.6	0.07	0.11
Elias 33 (raster)	4.5	0.22	-5.7	1.0	5.7	14	0.22	0.25
RNO 91 (raster)	0.5	0.26	-9.0	-0.6	2.0	5.0	0.24	0.18
UFO 1 (near IRS 63)	2.3	0.20	-1.7	1.0	3.8	7.0	0.13	0.14
UFO 2 (near IRS 37)	3.7	0.18	-4.1	0.6	6.2	8.9	0.15	0.12
UFO 3 (near WL 12)	4.3	0.24	0.3	1.5	6.2	8.7	0.10	0.15
UFO 4 (near IRS 54)	4.1	0.16	0.3	1.8	6.5	9.2	0.12	0.12
UFO 5 (near IRS 44)	3.8	0.18	-1.6	0.5	6.5	9.8	0.10	0.12
UFO 6 (near IRS 44)	3.8	0.18	-2.1	0.5	-	-	0.11	-
UFO 7 (near IRS 63)	2.3	0.20	-	-	3.8	6.0	-	0.1

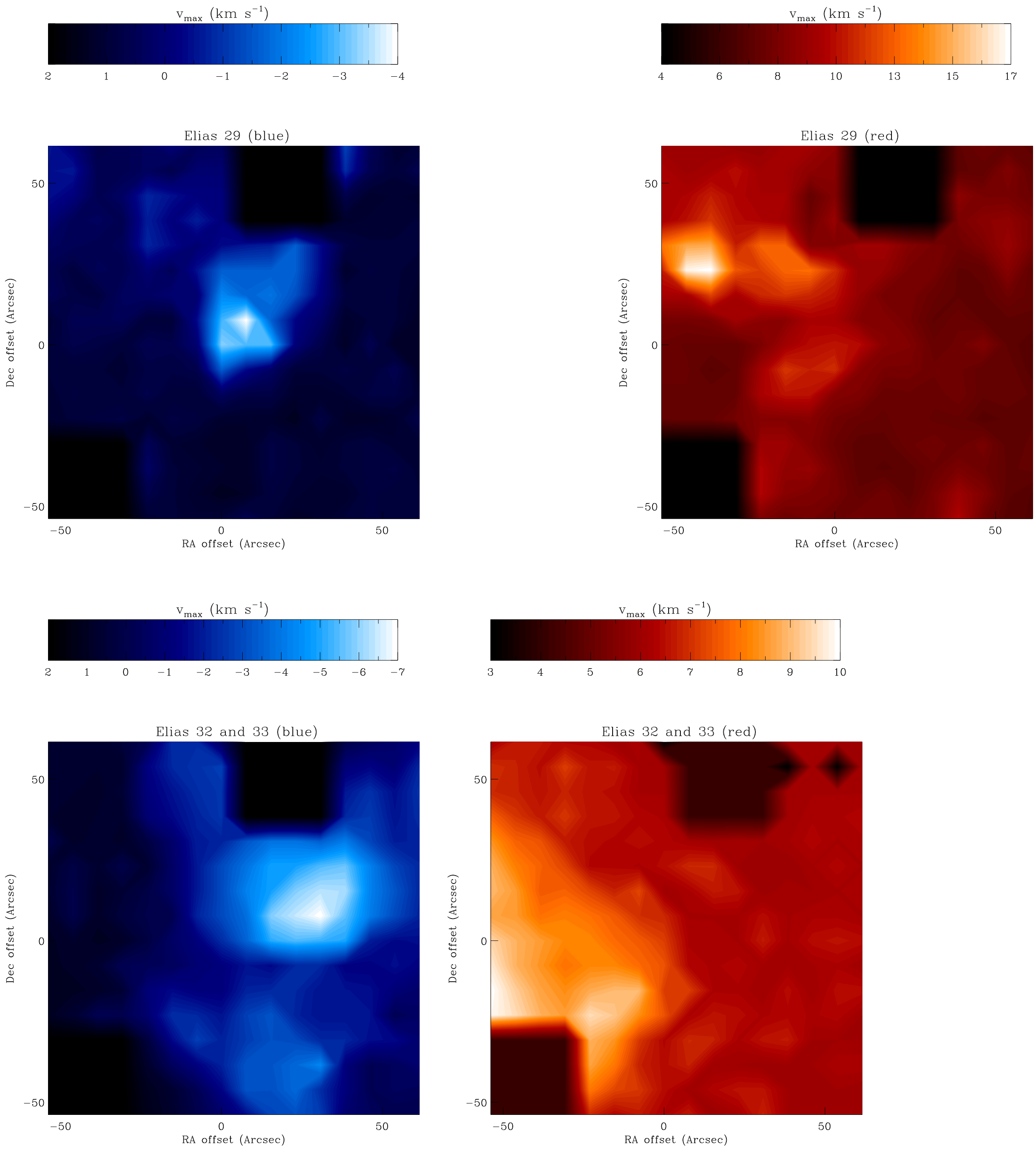

Figure 3: Color maps of the outer velocity limits both at the blue and the red side of the spectral profile, where the signal is still above σ_{rms} level. The left maps show the blue velocities, the right maps the red velocities. Each map consists of 60 levels, each normalized to its own minimum and maximum values. The brighter parts indicate emission at high velocities: possible outflow detection.

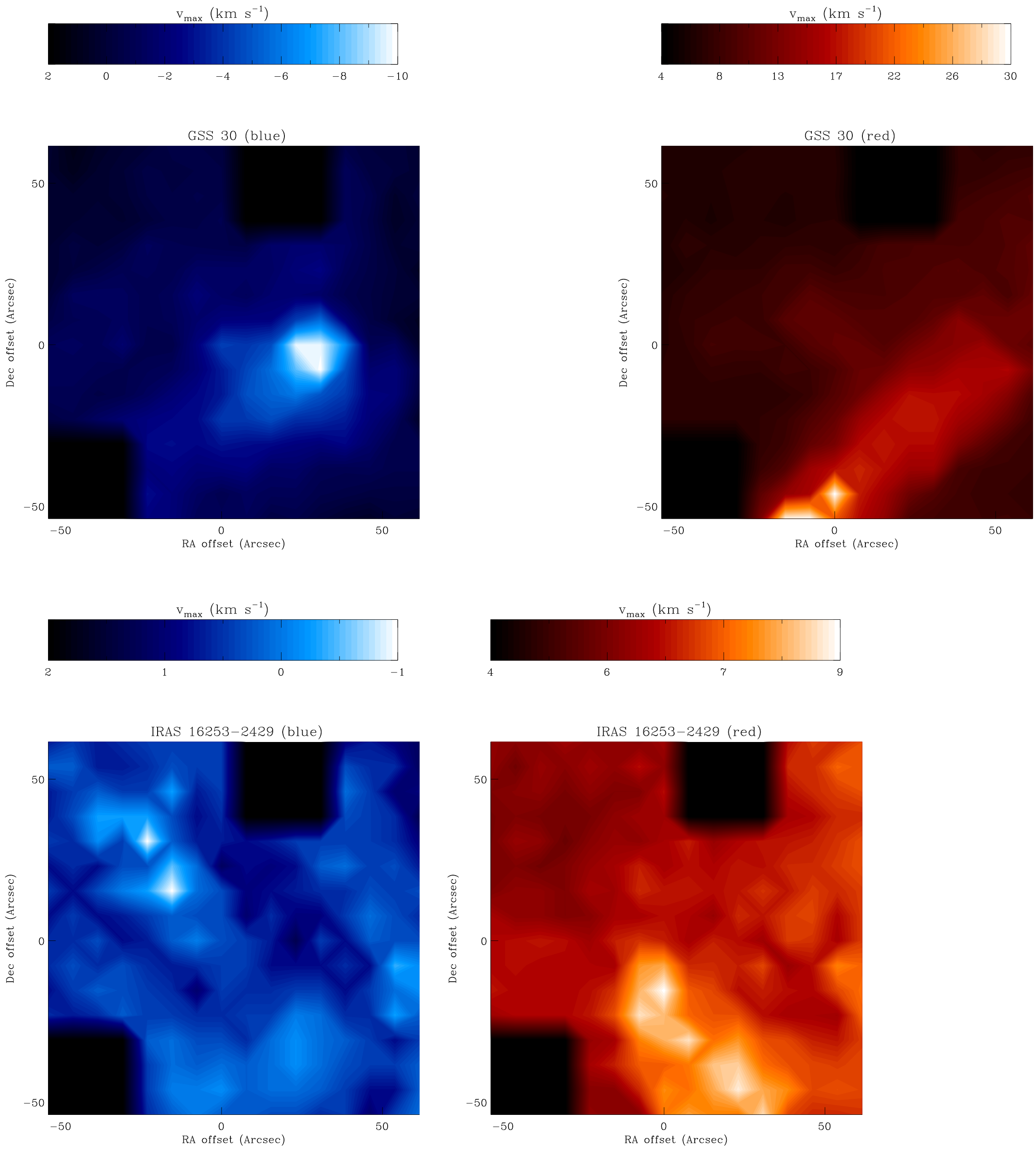

Figure 3: Color maps of the outer velocity limits - Continued

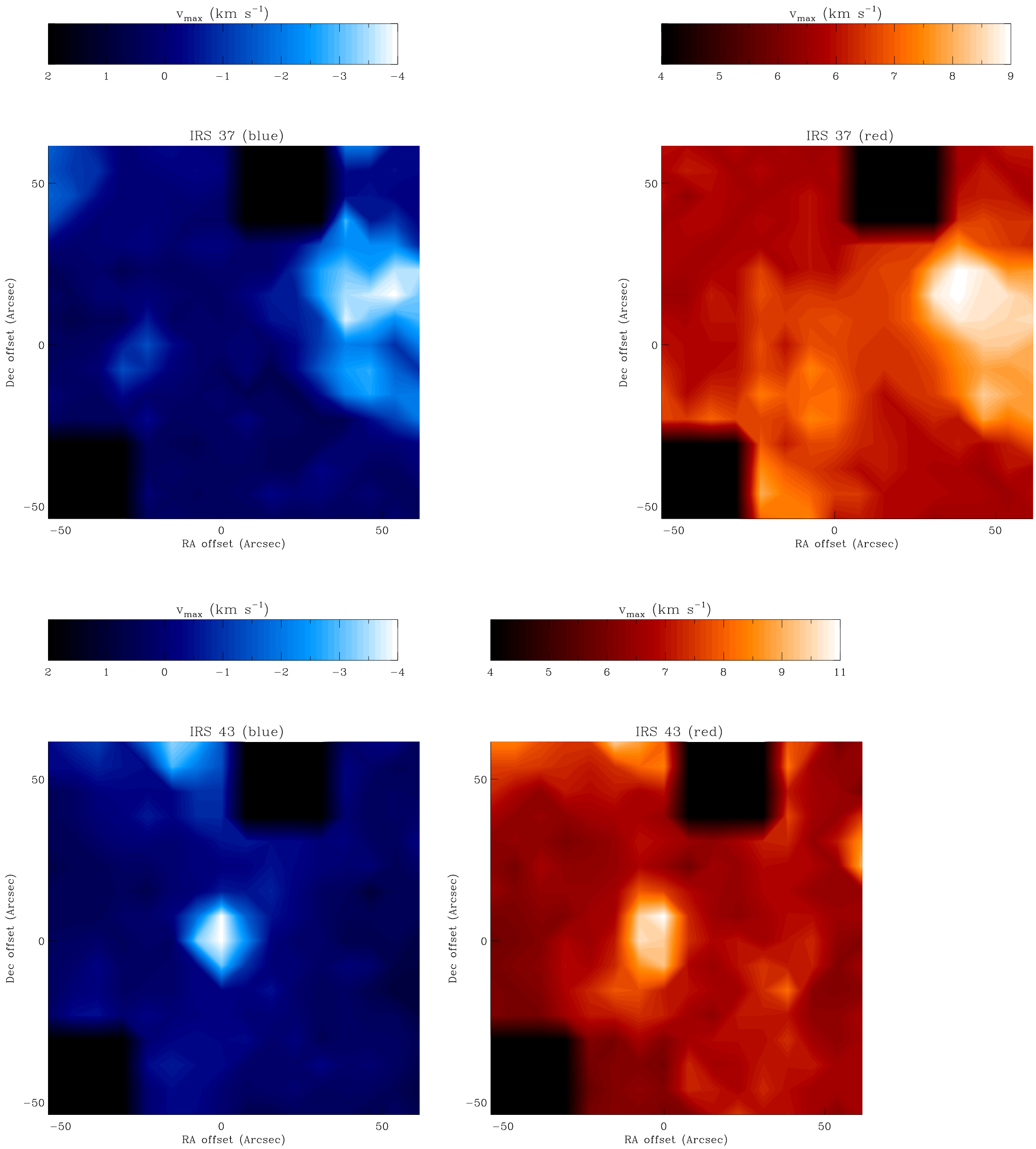

Figure 3: Color maps of the outer velocity limits - Continued

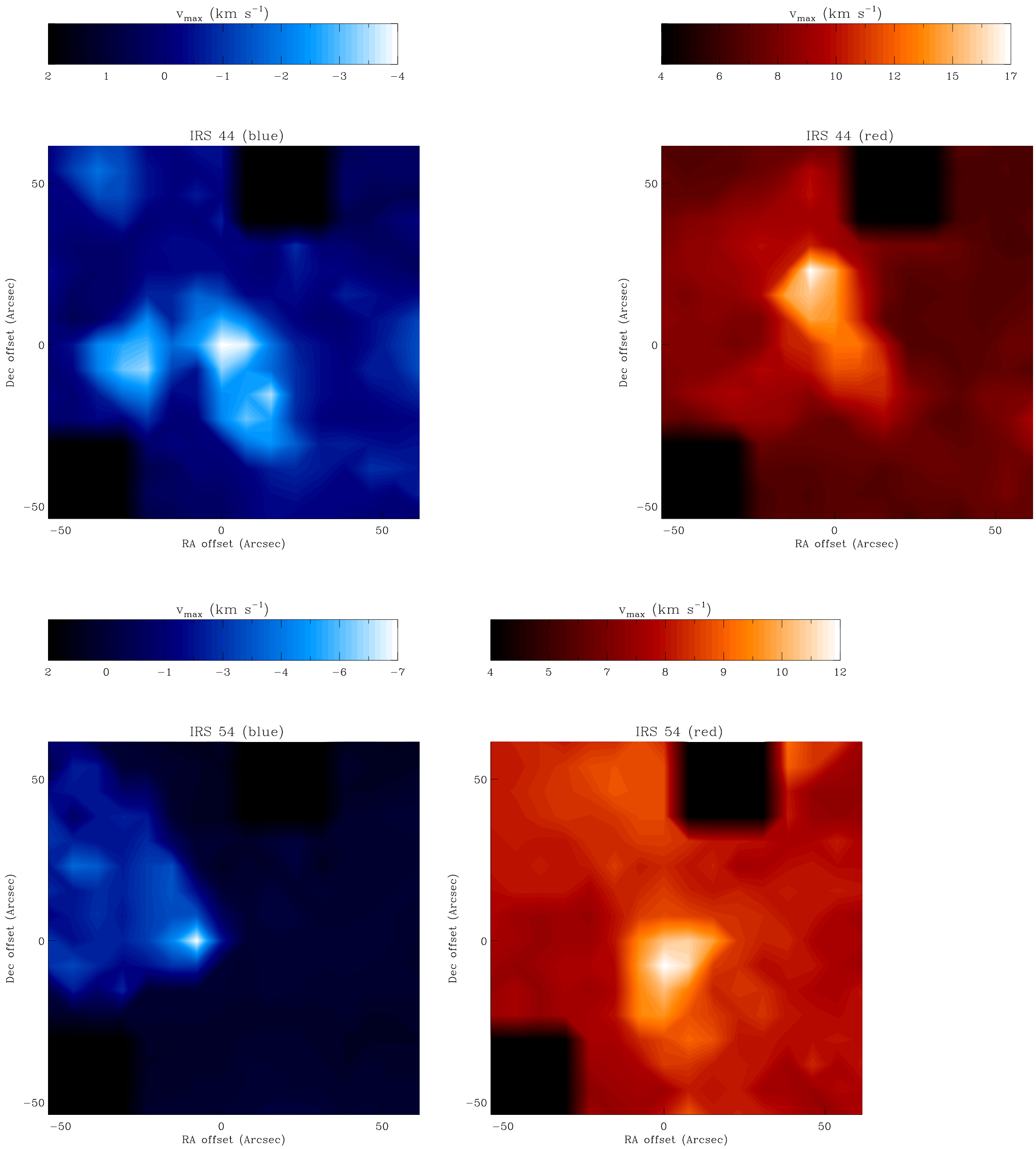

Figure 3: Color maps of the outer velocity limits - Continued

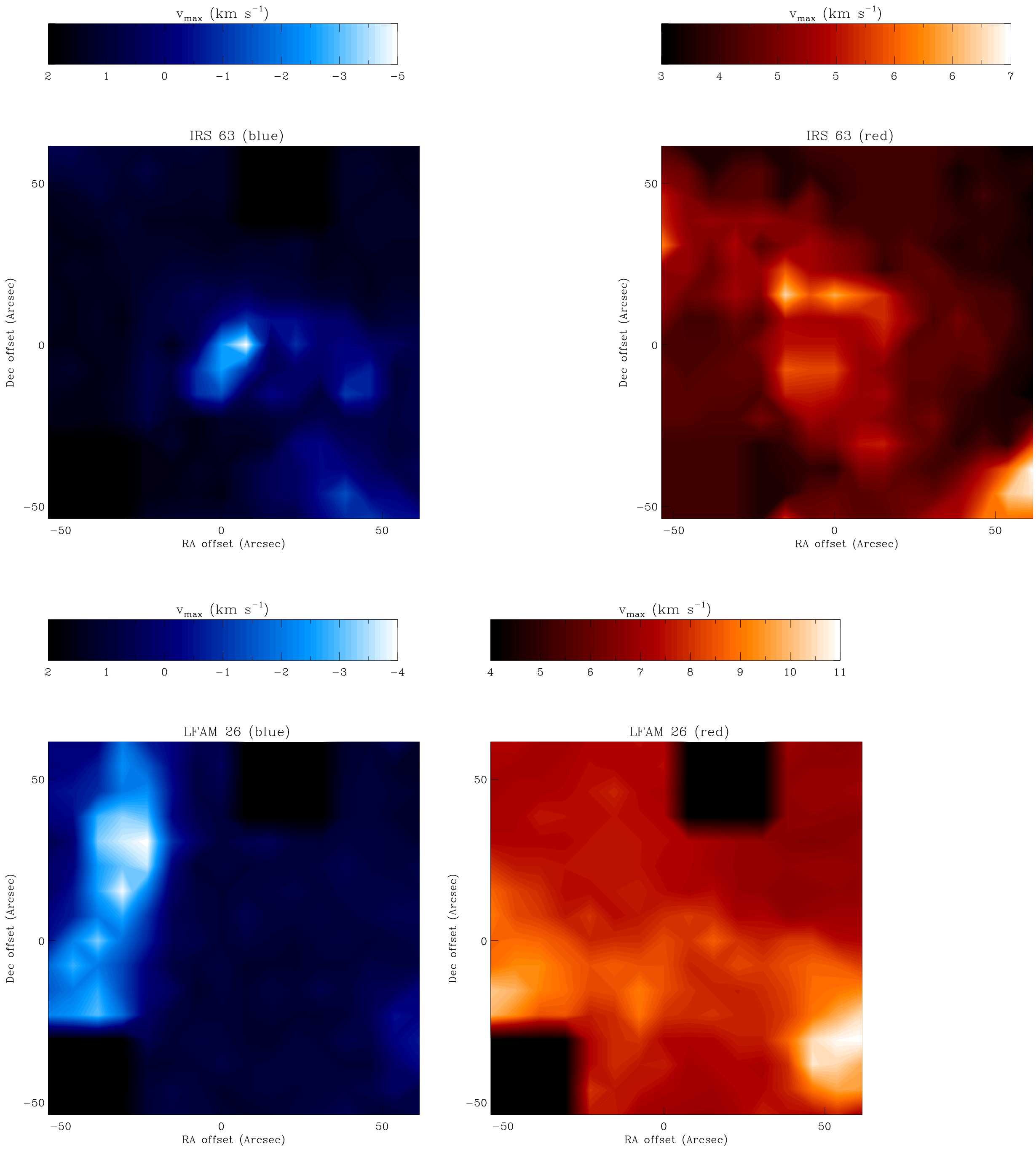

Figure 3: Color maps of the outer velocity limits - Continued

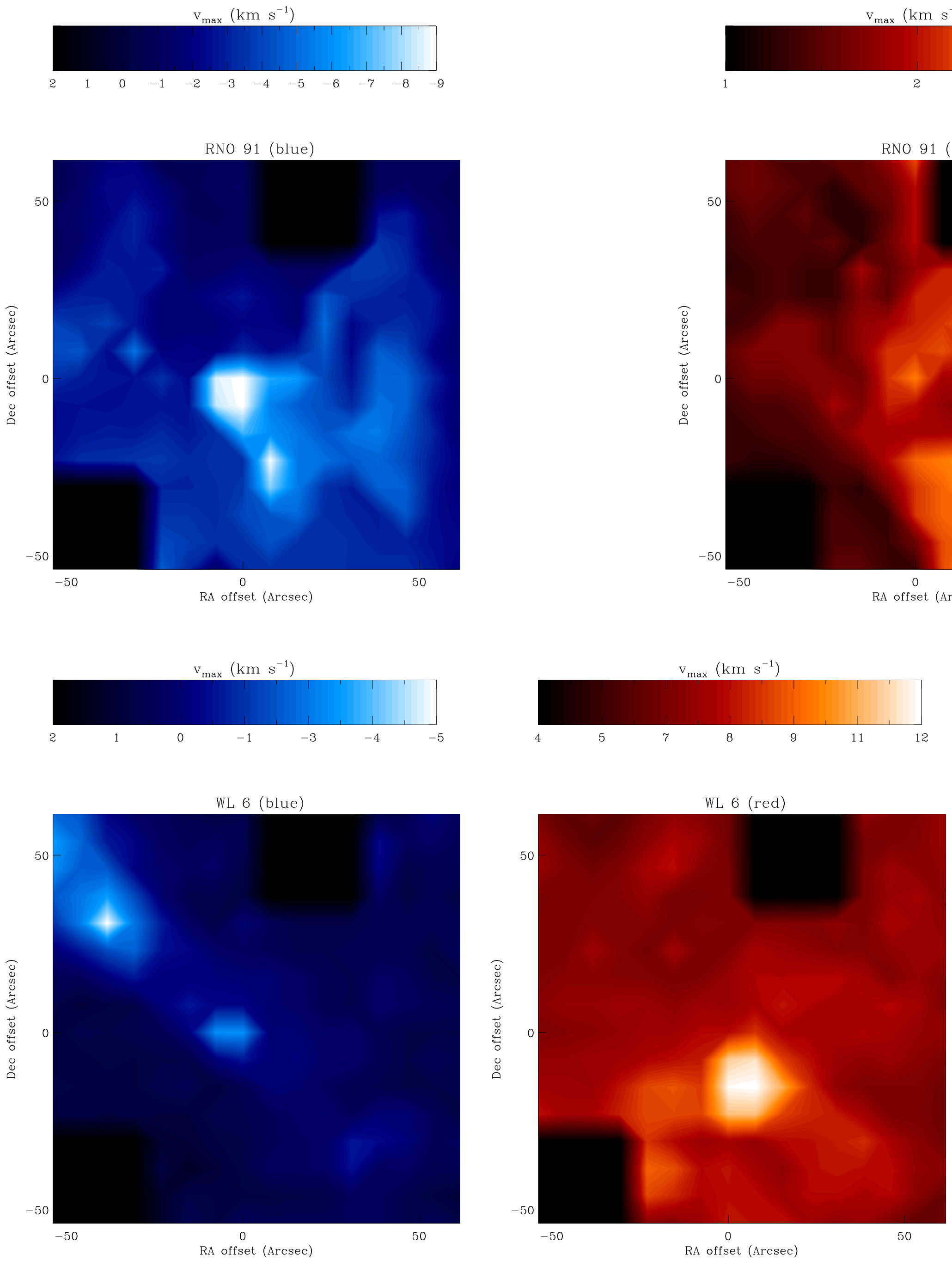

Figure 3: Color maps of the outer velocity limits - Continued

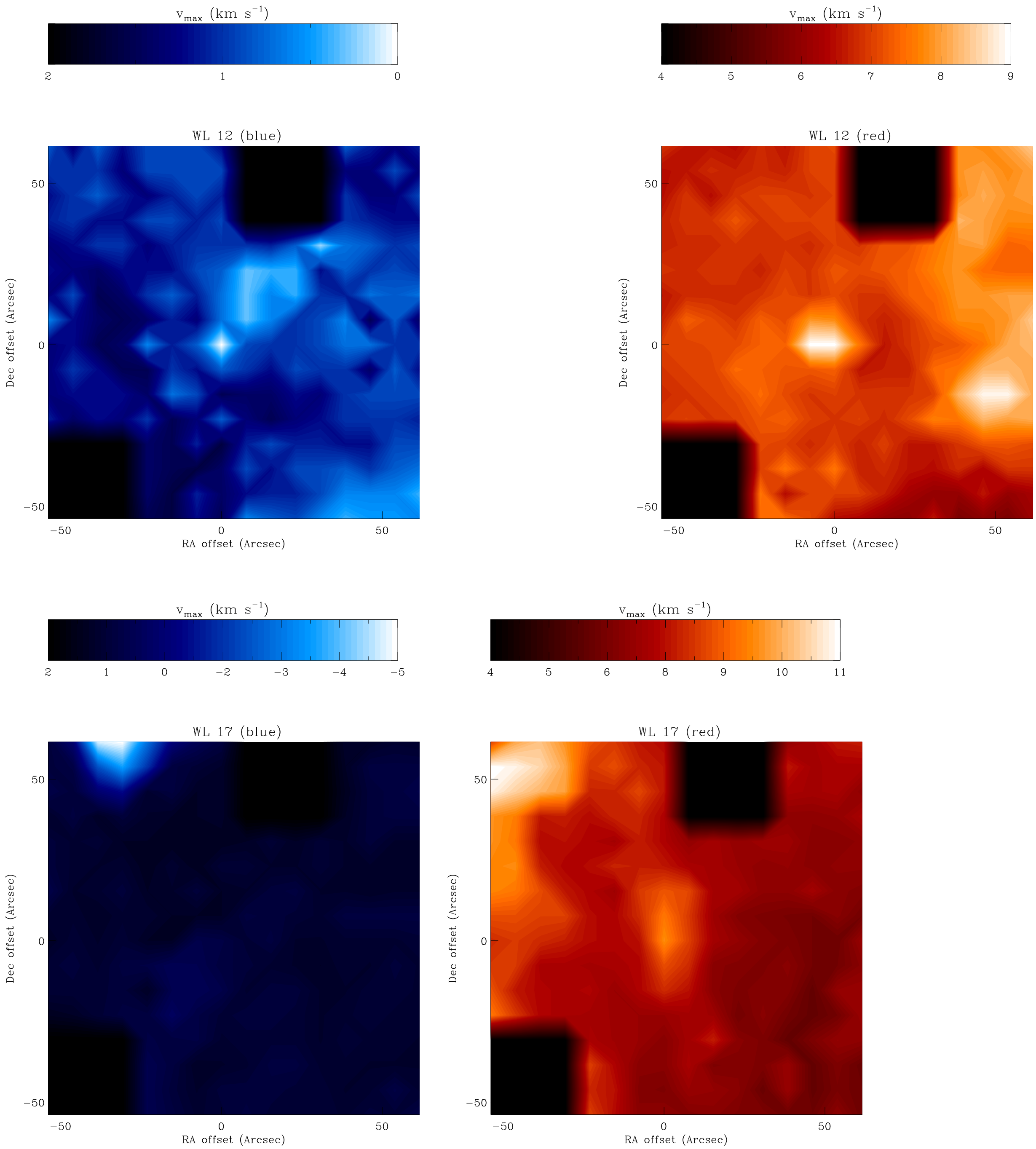

Figure 3: Color maps of the outer velocity limits - Continued

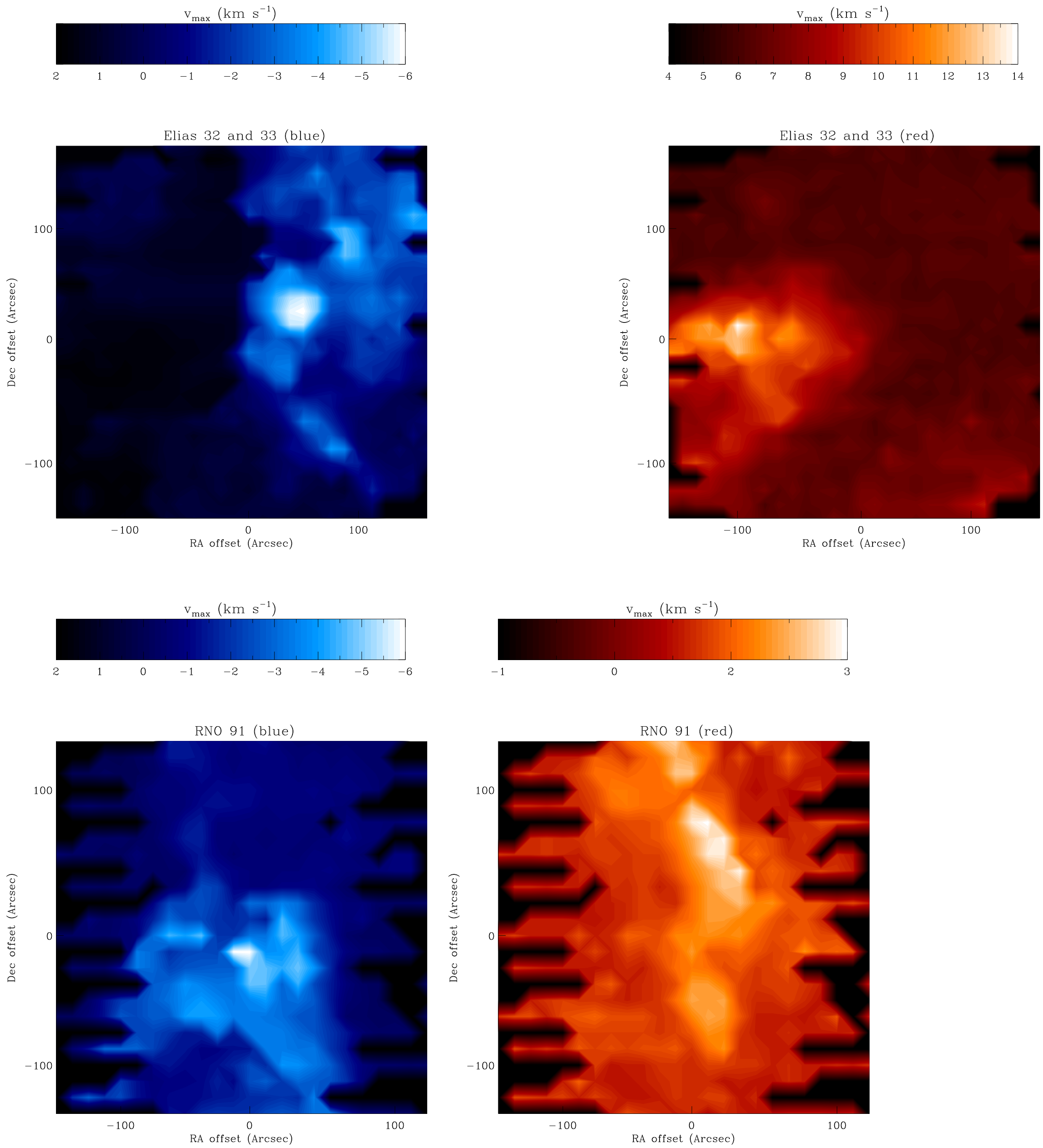

Figure 3: Color maps of the outer velocity limits - Continued. These maps are based on observations in the raster observing mode with a larger spatial coverage.

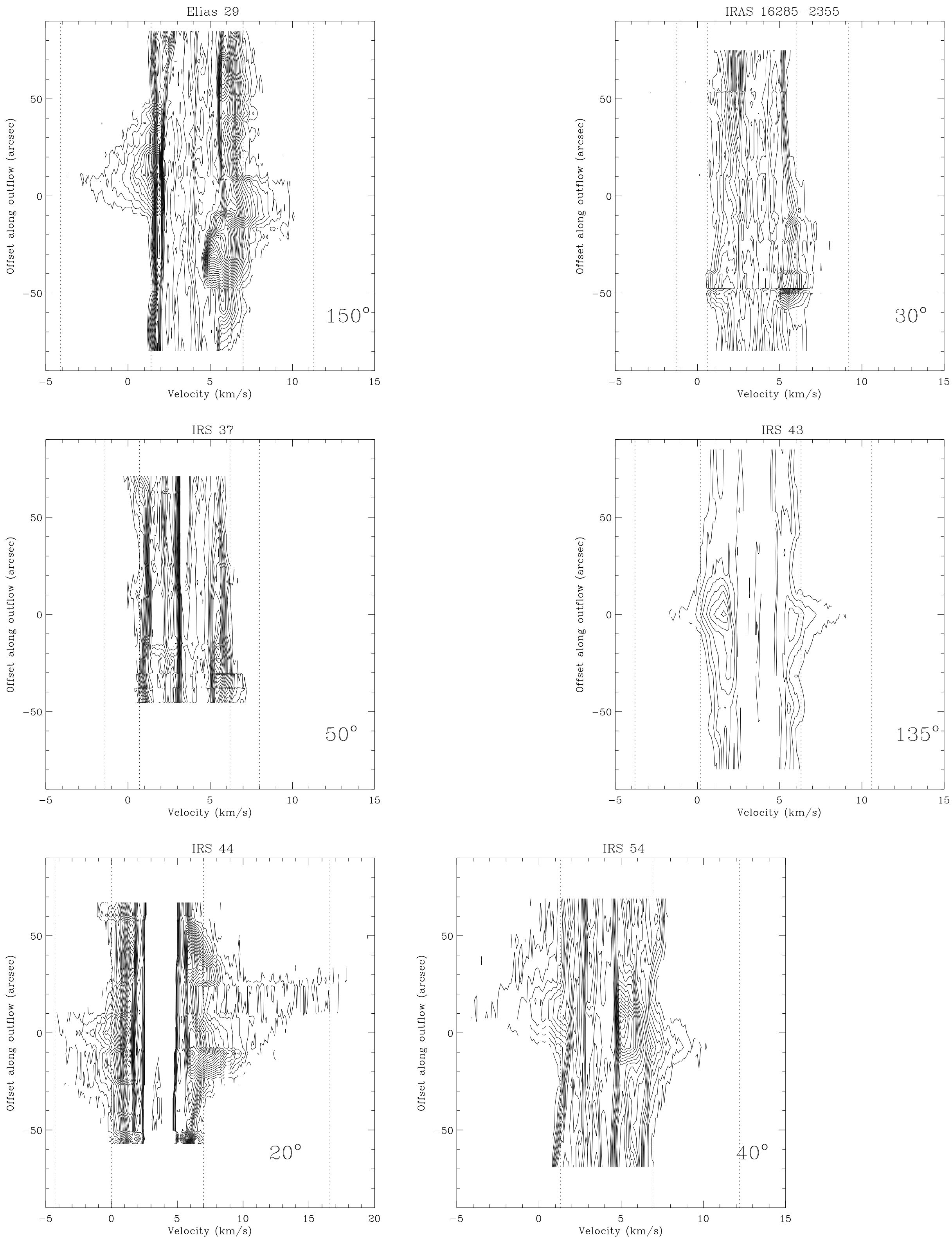

Figure 4: Position-velocity diagrams of the ^{12}CO emission along the outflow direction. Contours are drawn at $3\sigma_{rms}$ intervals, starting at σ_{rms}. In the lower right corner the position angle is given. No position-velocity diagrams were made for GSS 30, Elias 33 and RNO 91.

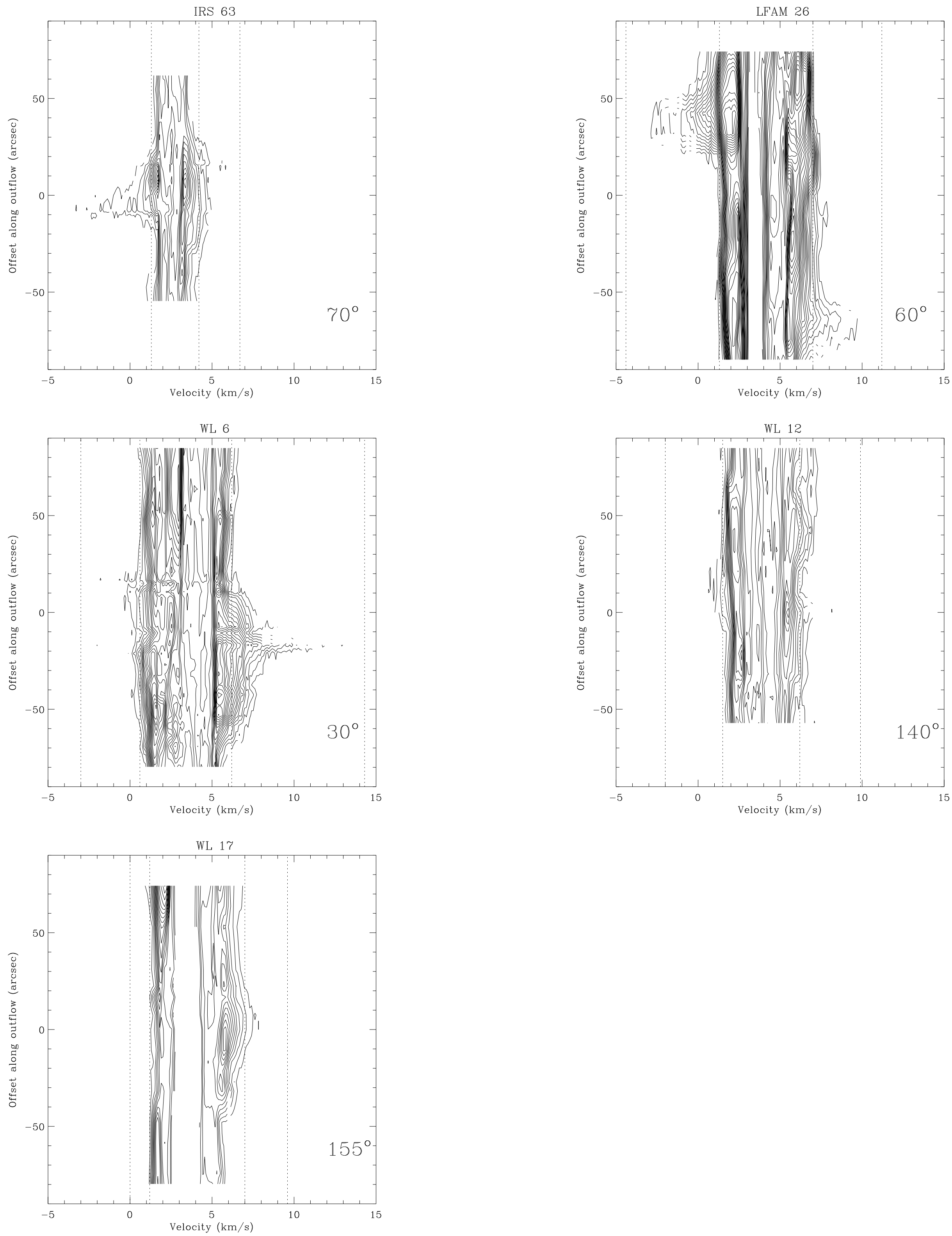

Figure 4: Position-velocity diagrams of the ^{12}CO emission along the outflow direction - Continued.

tour levels are taken at 3σ level, unless defined differently in the lower right corner (start level and step size), with σ defined as:

$$\sigma = 1.2 \cdot \sigma_{\rm rms} \cdot \sqrt(\Delta u \cdot \Delta v) \tag{1}$$

where $\sigma_{\rm rms}$ is the rms noise on the antenna temperature T, Δu is the velocity interval of the integration and Δv is the velocity resolution. σ is the noise level of the integrated intensity, which is given in Table 2 separately for the blue and the red.

4.3 Physical parameters

Outflow physical parameters are mass M, size $R_{\rm CO}$ and maximum velocity $v_{\rm CO}$, each for both the blue and the red parts of the outflow. These parameters are not further corrected for inclination; an inclination correction factor will be applied to the energetic quantities derived from these parameters (see Section 5.3). Because the ^{12}CO 3-2 line wing is assumed optically thin (see Section 5.3), the mass can be calculated from the column density $N_{\rm CO}$. The column density of the upper level u, N_u in cm^{-2}, is defined as:

$$N_u = \frac{8\pi k \nu^2 \int(T_{\rm mb} dv)}{hc^3 A_{ul}} \tag{2}$$

$$= \beta \frac{(\nu[\rm GHz])^2 \int(\rm T_{mb} dv)[\rm Kkms^{-1}]}{A_{ul}} \tag{3}$$

with $\beta \sim 1937$, $\int(T_{\rm mb}dv)$ the integrated intensity of the line wing, and A_{ul} the Einstein A coefficient for the transition $u-l$. For the calculation of the total mass, all spectra with a line wing integrated intensity $> 3\sigma$ are considered as part of the outflow (based on visual inspection of the contour map). The relevant spectra are summed and the total spectrum is integrated with the derived integration limits described above. This results in the column density for the entire outflow lobe. Assuming local thermodynamic equilibrium, the total column density is:

$$N = Q(T) N_u [g_u \exp(-E_u/kT)]^{-1} \tag{4}$$

with $Q(T)$ the partition function, g_u the degeneracy of the upper level, E_u the energy of the upper level, k the Boltzmann constant and T the kinetic temperature. A kinetic temperature of 100 K was assumed. However, any temperature between 20 and 150 K gives a factor within 40% of the factor at 100 K, as can be seen in Figure 5. The other numbers were taken from CDMS. Finally, the mass is calculated by:

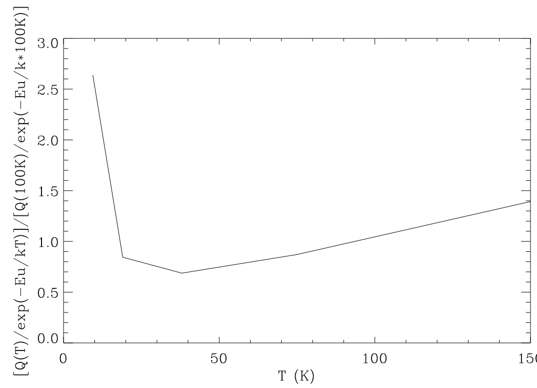

Figure 5: The factor used to calculate the total column density from the column density at level J=3 as function of temperature, i.e. $Q(T)(g_u \exp(-E_u/kT])^{-1}$, as function of temperature, relative to this factor at 100 K (assumed in this study). For any temperature between 20 and 150 K this factor is within 40% of the factor at 100 K.

$$M = NA \left[\frac{\rm H_2}{^{12}\rm CO}\right] \cdot 2.4 m_{\rm H} \tag{5}$$

with M the mass, A the physical size of the actual region covered in a pixel and m_H the mass of a hydrogen atom. The ratio $\left[\frac{\rm H_2}{^{12}\rm CO}\right]$=1.5·10^4 and a factor 2.4 was used instead of 2 to take helium into account in the mass calculation as well (the mass percentage of helium in the Universe is 10%).

Figure 6 shows an overview of CO spectra for each source: the strongest blue and red wings, an off-source spectrum and the average outflow spectrum are plotted for each source. Integration limits are overplotted. This figure provides a good overview of the spectral profiles of each outflow source.

The velocity $v_{\rm CO}$ is the maximum velocity extent from the line center (Cabrit & Bertout 1992) and is defined as the outer velocity limit (which is the max-

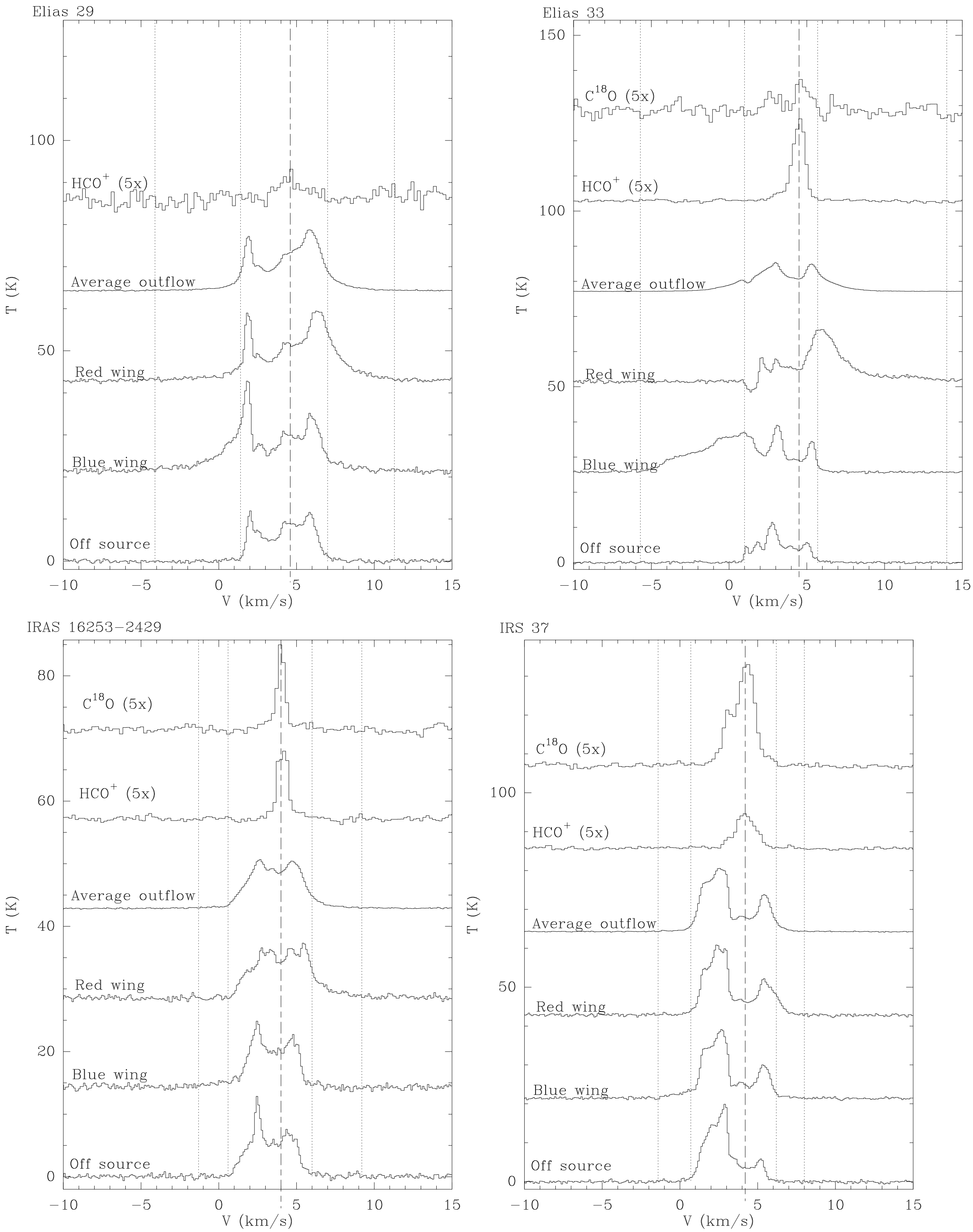

Figure 6: Overview of relevant outflow spectra. Each diagram shows from top to bottom $C^{18}O$ (where available), HCO^+ and ^{12}CO: the average outflow spectrum, the strongest red wing spectrum, the strongest blue wing spectrum and an off-source spectrum. $v_{\rm source}$ (dashed line) and the integration limits (dotted lines) are indicated. HCO^+ and $C^{18}O$ data taken from van Kempen et al. (2009c) and the JCMT Data Archive.

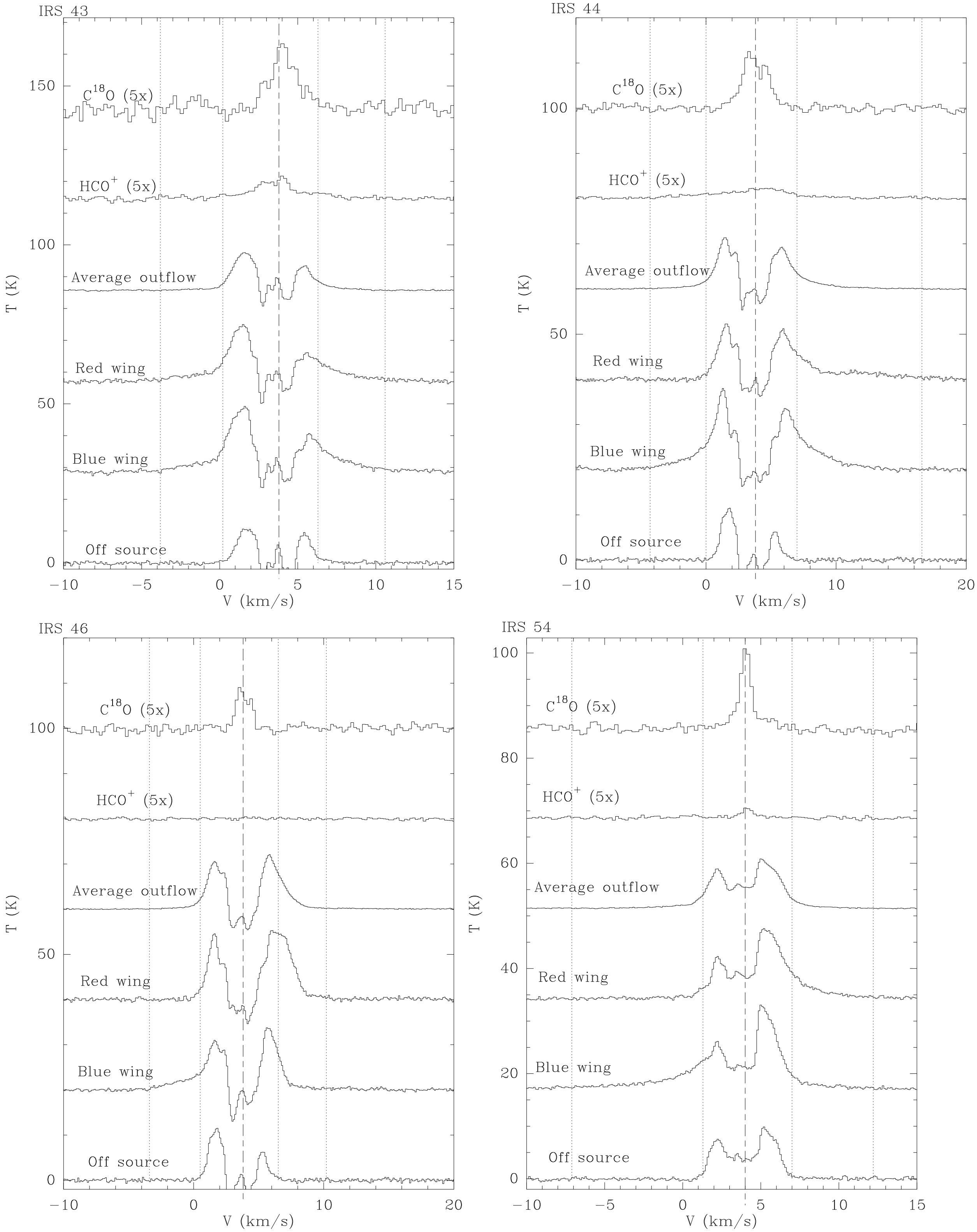

Figure 6: Overview of relevant outflow spectra - Continued

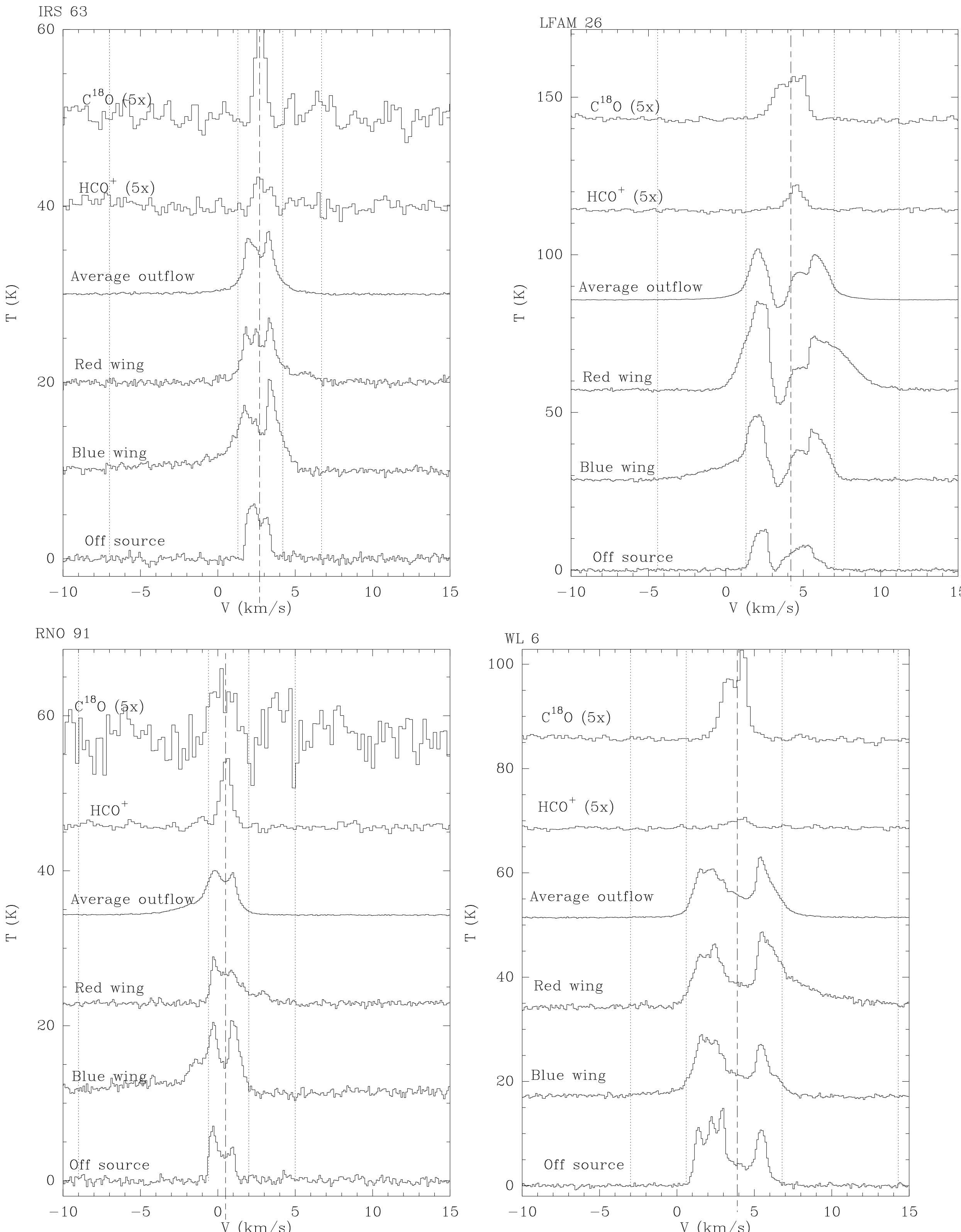

Figure 6: Overview of relevant outflow spectra - Continued

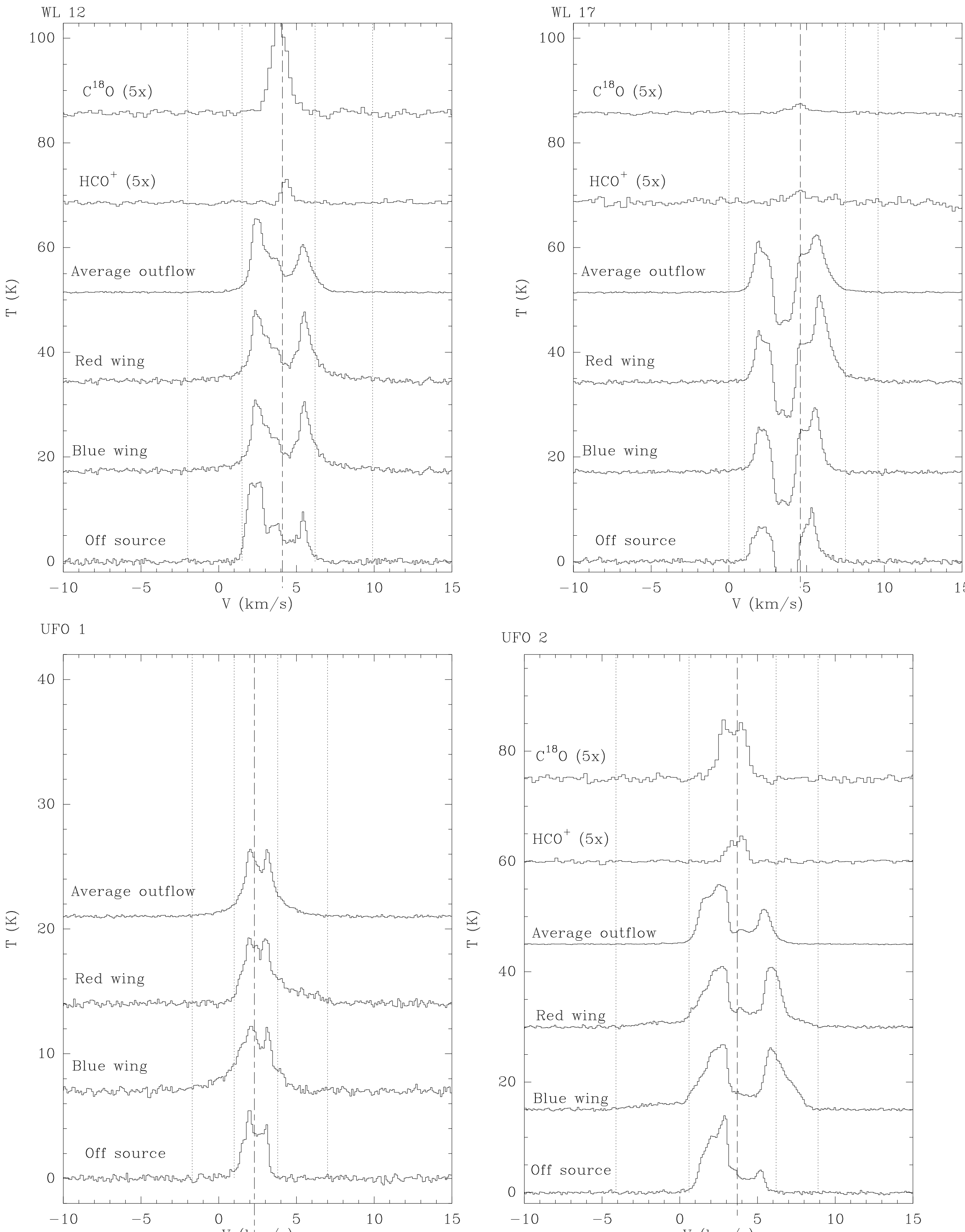

Figure 6: Overview of relevant outflow spectra - Continued

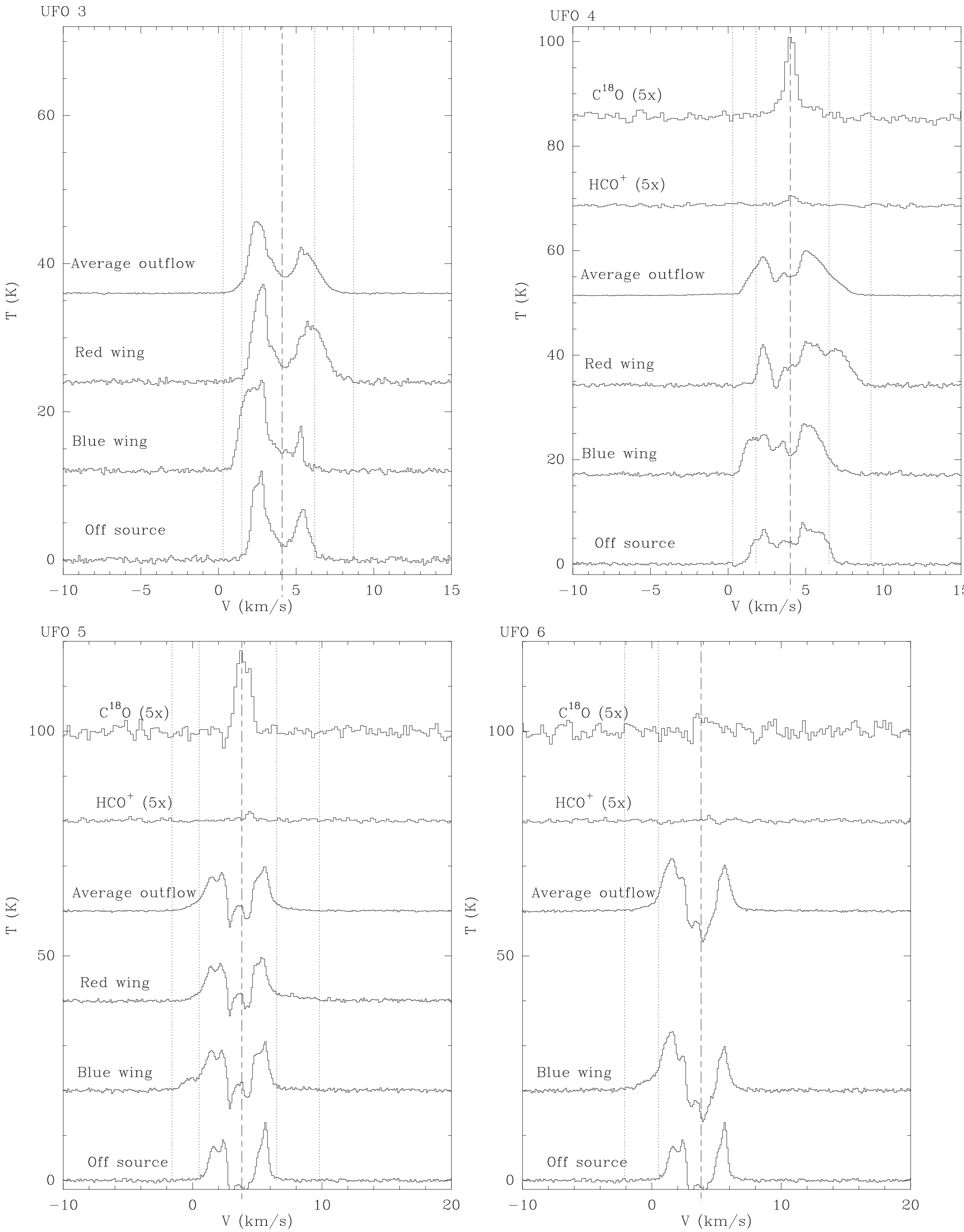

Figure 6: Overview of relevant outflow spectra - Continued

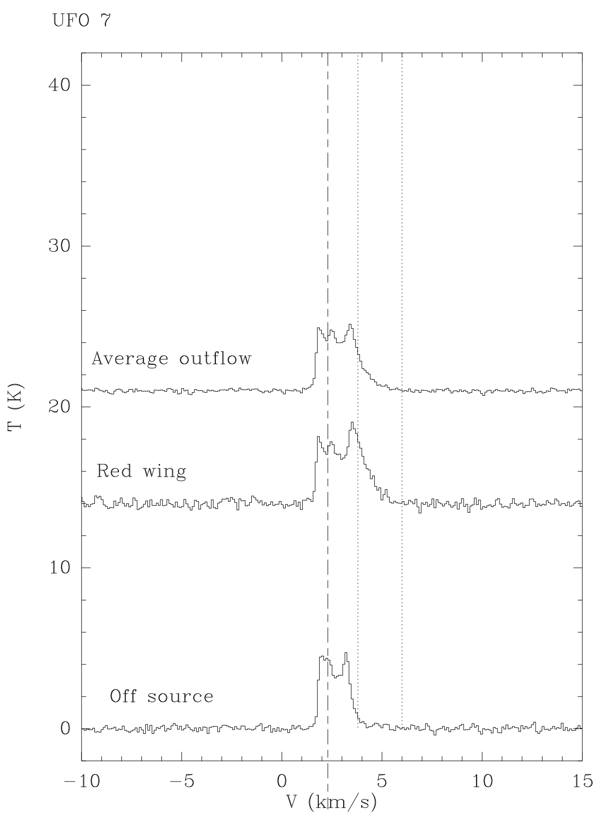

Figure 6: Overview of relevant outflow spectra - Continued

imum outflow velocity) minus the line center velocity. Since the line center is not easy to derive from the ^{12}CO 3-2 lines, because the central profile contains narrow absorption features and sometimes multiple emission features, HCO$^+$ 4-3 and C^{18}O 3-2 emission lines are used (where available), since these are characterized by narrow, Gaussian-like emission profiles. Spectra from central positions of the data set as used by van Kempen et al. (2009c) are fitted to determine the central velocity $v_{\rm source}$. Values can be found in Table 2. The spectra are also added to the overview spectra in Figure 6.

The size $R_{\rm CO}$ or extent of the outflow is defined as the maximum flow extension from the central star by visual inspection of the outflow maps, in Figure 7 (Cabrit & Bertout 1992). Unlike Cabrit & Bertout (1992), values for both a blue and a red outflow size are assigned, because the environment influences the outflow extent significantly. The value of $R_{\rm CO}$ expressed in AU is calculated assuming a distance to Ophiuchus of 120 pc (Loinard et al. 2008). The actual dimensions of a pixel (7.5″x7.5″) are 900 AUx900 AU and in the raster images the dimensions (12″x12″) are 1440 AU x 1440 AU. Note that the diffraction limited beam is still 15″.

5 Results

5.1 Spectral profile

The spectra show a strong, broad central profile around 4 km s^{-1}, often consisting of several emission peaks, caused by foreground layers. The environment was studied in more detail in C^{18}O by van Kempen et al. (2009c), who derived properties of foreground layers for e.g. LFAM 26, IRS 44 and IRS 37. At the outflow positions, broad line wings are detected (up to 15 km s^{-1} in the red and -10 km s^{-1} in the blue), which were integrated in the data reduction. The spectra are furthermore characterized by narrow absorption features, which are interpreted as self-absorption. However, in some cases the absorption is below zero, which is clearly not self-absorption. The maps with Elias 32 and Elias 33, IRS 37, IRS 43, IRS 44, LFAM 26, WL 17 and IRS 54 all show negative absorption peaks in part or all of their spectra in the central profile around 4 km s^{-1}. This is caused by emission in the reference off position, mentioned in Section 3.1. All but IRS 54 were observed on June 19th. Since the absorption peaks only show in the main envelope spectral profile, they do not interfere with the outflow wings and do not have to be taken into account in our calculations. Some spectral maps, e.g. IRS 54 and Elias 29, locally show extra emission features at high velocities (typically +/- 3-4 km s^{-1} with respect to the $v_{\rm src}$) in the wing velocity interval. These features do not interfere with the outflow location, but they do show up in the contour maps.

5.2 Outflow maps

The outflow maps in Figure 7 clearly show outflow activity in most of the sources, but other features, usually caused by the presence of nearby sources, are observed as well. IR source positions are at 0,0 or marked (for multiple sources). Most outflows fit in the 2′x2′ region, except for Elias 32/33, RNO 91, Elias 29, LFAM 26 and IRAS 16253-2429. The first two are also observed in the raster mode in 4′x4′ maps, covering a larger part of the outflow. In two cases, the red and blue lobes overlap with the pixels from the broken receivers, causing a likely underestimate of the total mass.

Local emission features, possibly caused by foreground emission layers, are hereafter named 'odd emission', since they do not belong to the outflow of the central source, considering their morphology. Alternative explanations, like chopping into an absorption position, deflected outflow, instrumental effects and other emission lines are all ruled out. Chopping into absorption is very unlikely, a deflected outflow would need to be deflected at least twice and then end up moving in the plane of the sky, instrumental effects would be visible in the other data as well and other strong emission lines are not present at this frequency. Spectra of these odd emission features are given in Figure 8. An entirely new interpretation of this odd emission was the overlap of outflows from other sources into the

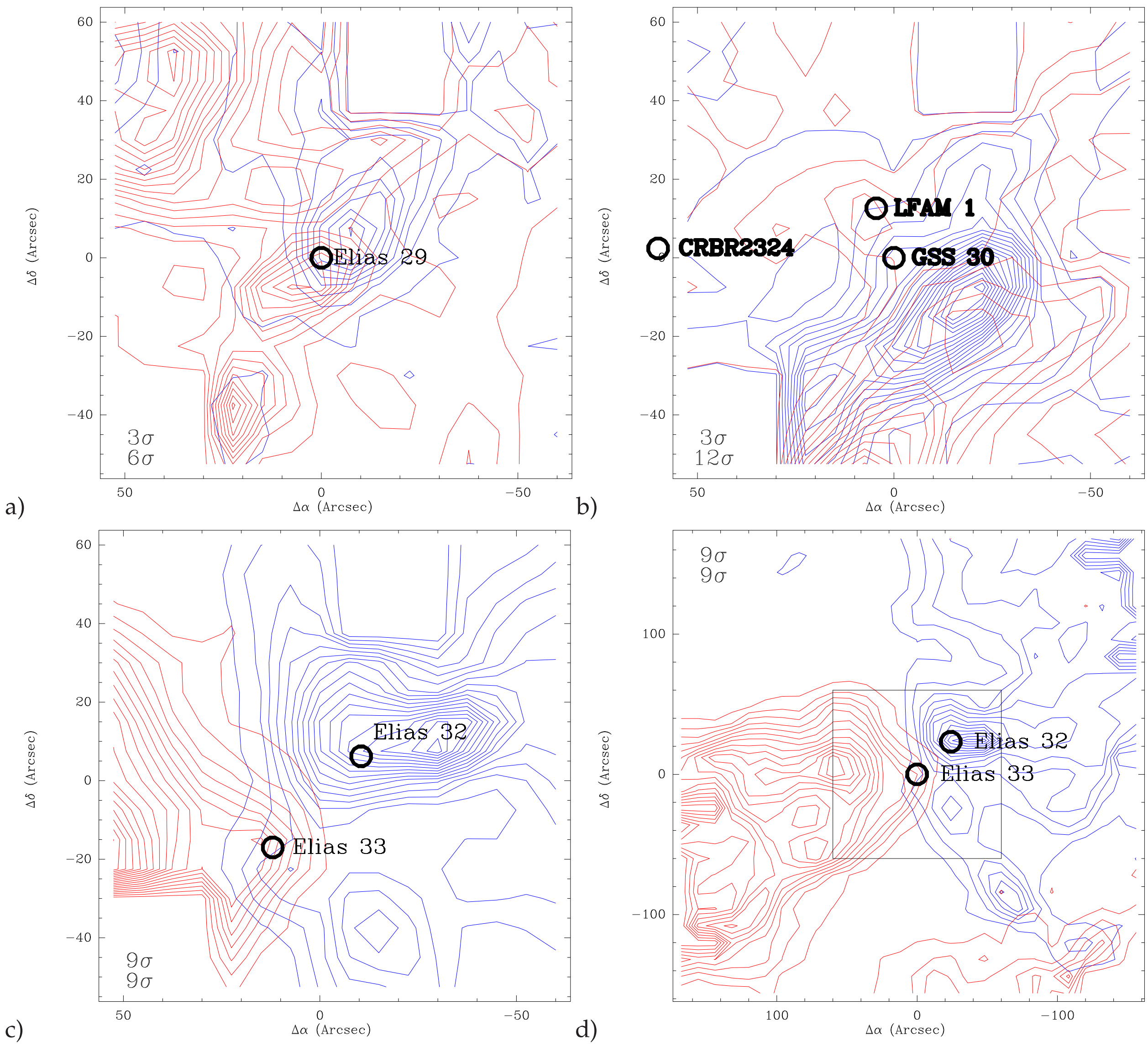

Figure 7: Outflow maps of all sources. Contours are drawn based on the integrated intensities of the line wings. In the lower left corner, the starting level and the step size of the contours is given. If two values are given for the step size, the first and second are the blue and red step, respectively. Figures a-d are Elias 29, GSS30 and Elias 33 (jiggle and raster observation). The box in panel d (raster observation) indicates the size of panel c (the jiggle observation).

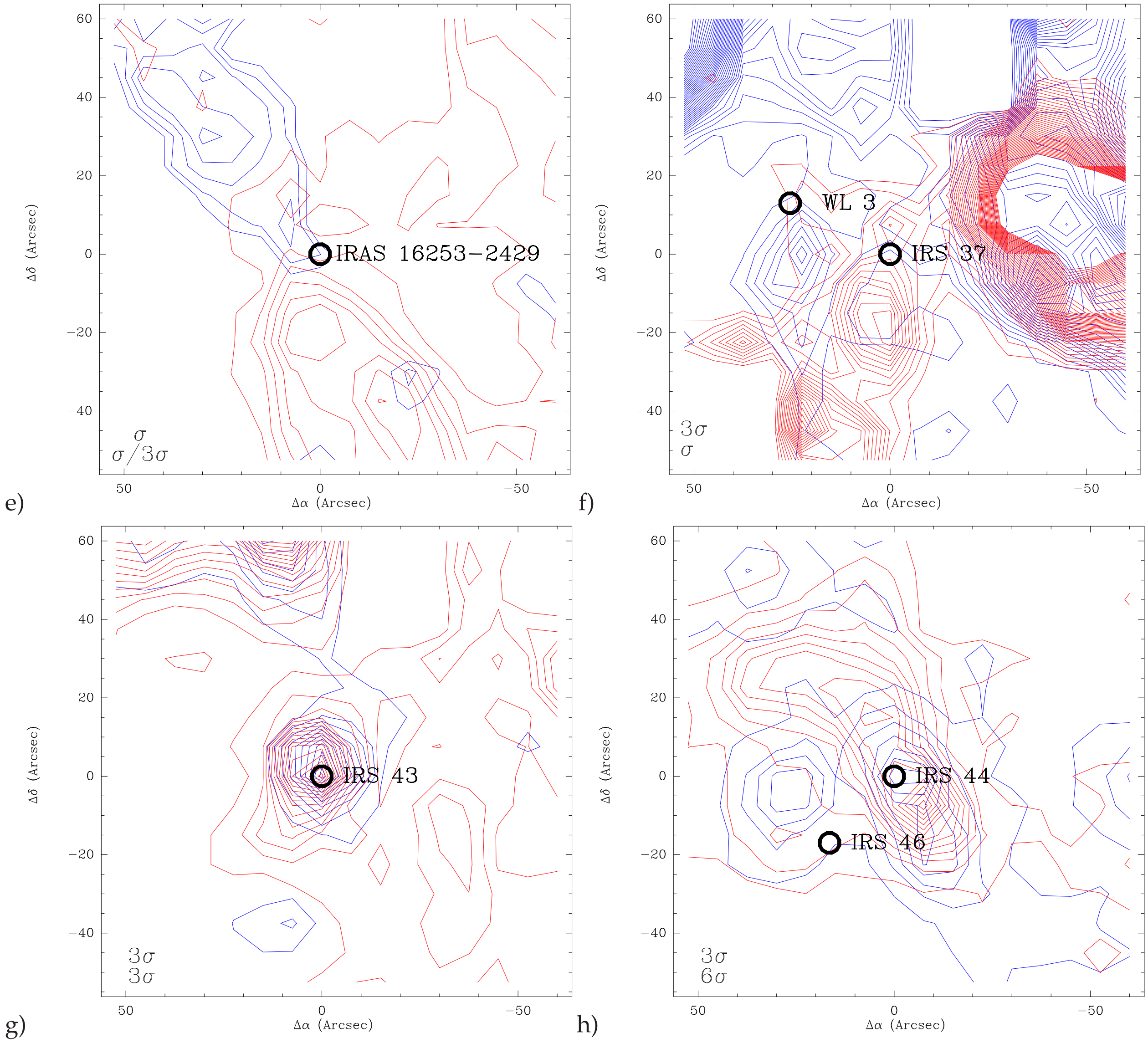

Figure 7: Outflow maps of all sources - Continued. Figures e-h are IRAS 16253-2429, IRS 37, IRS 43 and IRS 44.

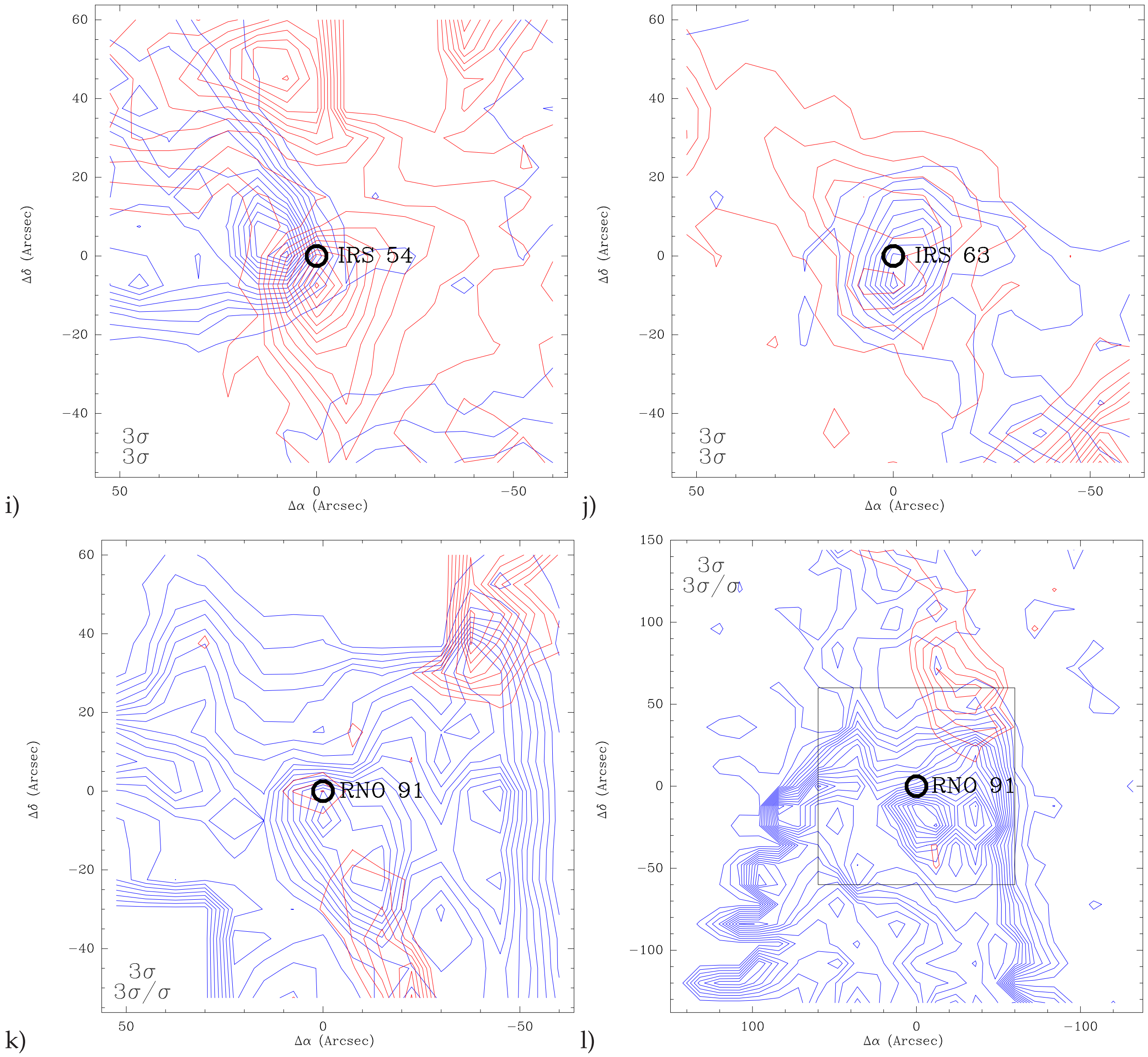

Figure 7: Outflow maps of all sources - Continued. Figures i-l are IRS 54, IRS 63 and RNO 91 (jiggle and raster observation). The box in panel l (raster observation) indicates the size of panel k (the jiggle observation).

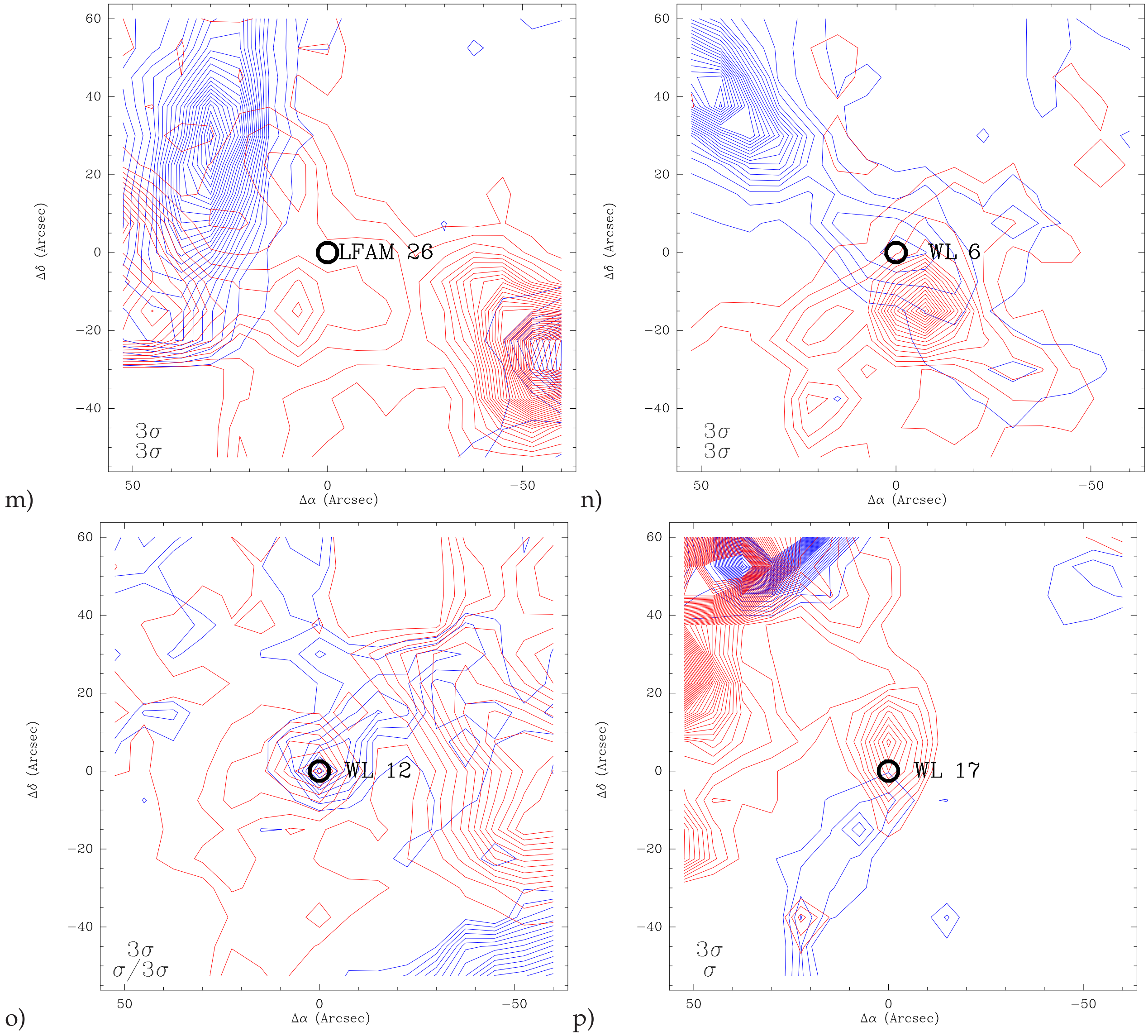

Figure 7: Outflow maps of all sources - Continued. Figures m-p are LFAM 26, WL 6, WL 12 and WL 17.

maps. This interpretation is used throughout the remaining part of the report.

Seven possible new outflows which could not be assigned to an IR source (UFOs) were discovered in the contour maps near known Class I sources with outflows. Spectral maps are given to show the local changes in the spectra. Spectral overviews of these UFOs are given in Figure 6.

We will now discuss each outflow map individually, and describe the outflow activity in the region.

- The first map in Figure 7 shows the outflow of Elias 29 in the center. Both the red and the blue lobe suffer from the missing data due to the broken receivers, so that the mass of the outflow is probably underestimated. A blob of red odd emission is detected in the north east. Spectra of this odd emission are given in Figure 8. An explanation for the odd emission different than foreground layers is a red lobe from LFAM 26 extending into this map. Bussmann et al. (2007) made large-scale observations of the Elias 29 region, and concluded that the Elias 29 blue lobe was much larger than previously thought (see also Figure 9 and 10). The blue lobe in the LFAM 26 map would actually belong to Elias 29, and the bipolar outflow of LFAM 26 consists of two very extended mainly red lobes in two opposite directions (east and west). The eastern red lobe is the red odd emission in the Elias 29 map. The observed wing velocities are consistent with this explanation, but a bipolar outflow with red lobes in opposite directions is quite unlikely considering our view of the origin of a bipolar outflow. Small blue line wings are detected in these two red lobes as well, supporting evidence for a quadrupolar outflow. The reason that the connection between the Elias 29 and LFAM 26 maps is not so clear in these results is that two of the receivers were broken at the time of the observations, as seen in the velocity maps, just at the positions where the two maps and especially the outflow lobes start overlapping. Besides, the LFAM 26 observations suffer from negative absorption seriously inflicting the cen-

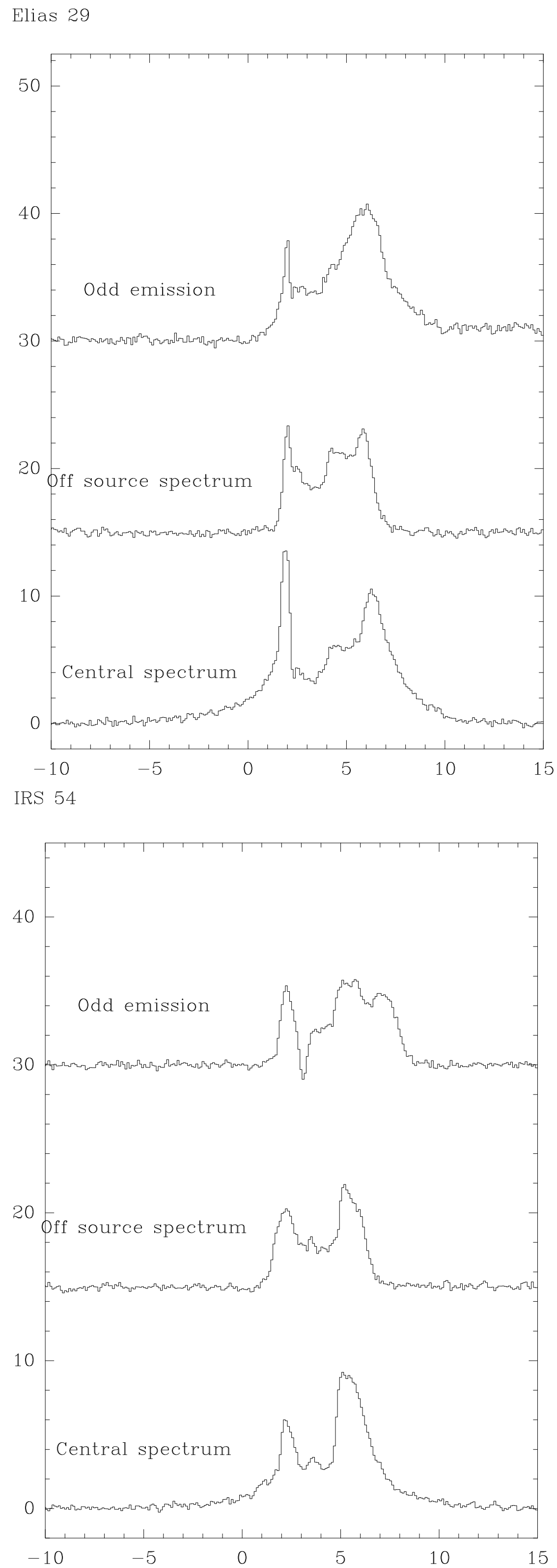

Figure 8: Spectra of odd emission from the Elias 29 and IRS 54 map. The spectra are taken from the north east of the Elias 29 map and the central north and central south of the IRS 54 map.

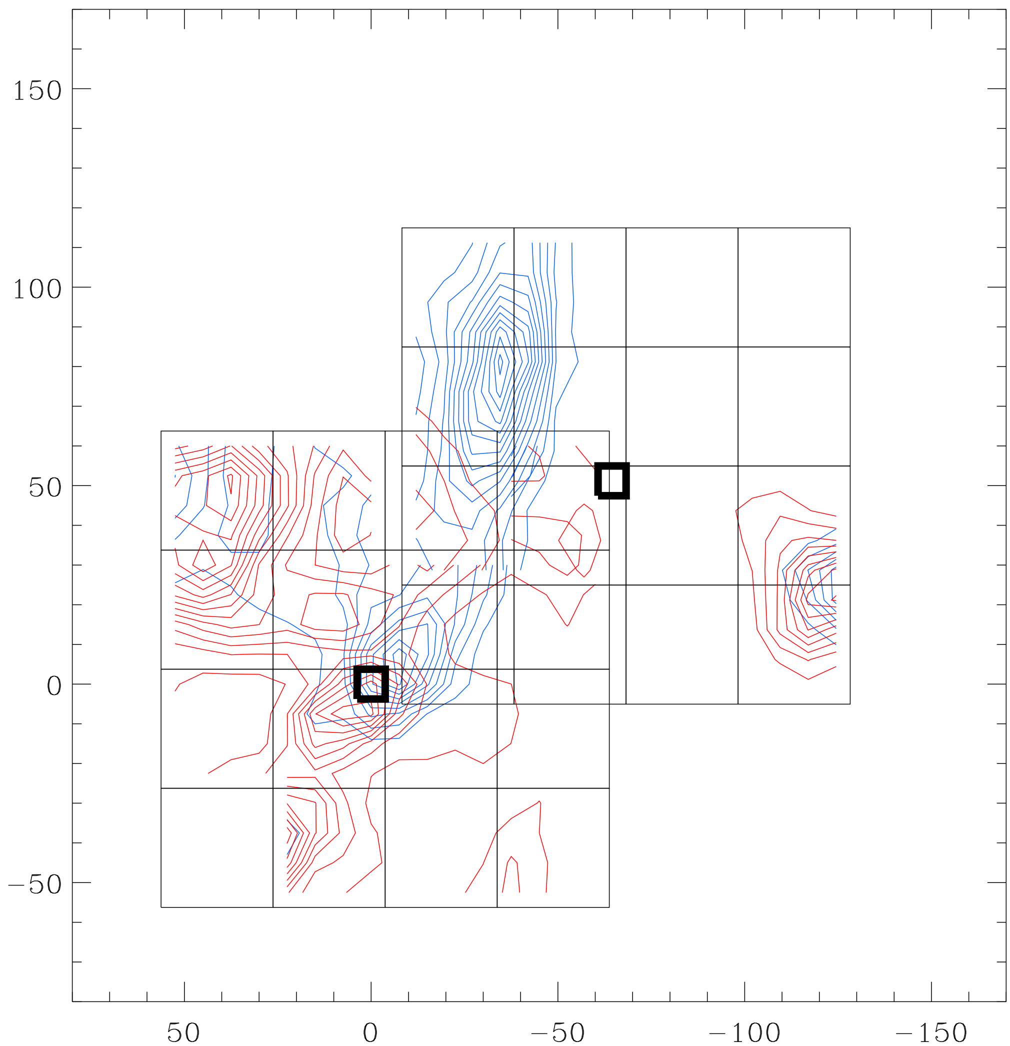

Figure 9: The region of Elias 29 and LFAM 26, as mapped in our observations, with the Elias 29 map in the south east and the LFAM 26 map in the north west. Contours are drawn with the same levels as in Figure 7. The thick black squares mark the location of the sources. The blue lobe in the LFAM 26 may belong to the Elias 29 outflow, and the odd red emission in the Elias 29 map may belong to the eastern red lobe of LFAM 26.

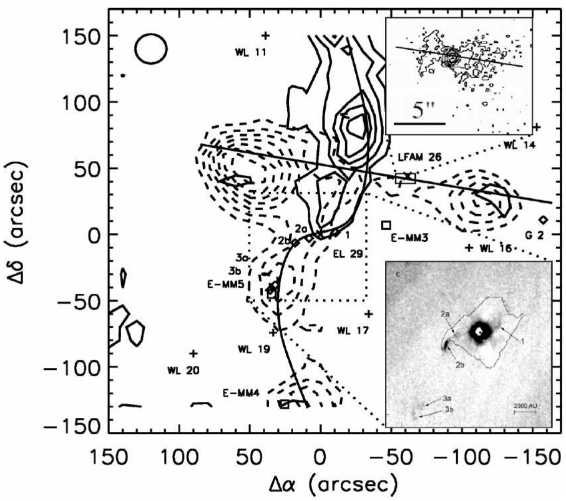

Figure 10: The region of Elias 29 and LFAM 26, taken from Bussmann et al. (2007) (Figure 2). Solid lines are used for the blue integrated emission, dashed lines for red emission.

tral profile, making it harder to see the analogies with the spectra in the Elias 29 map. Figure 9 shows where the contours overlap, supporting the statements above. Figure 2 taken from Bussmann et al. (2007) is shown in Figure 10. The elongated direction of the blue lobe in the LFAM 26 map is another argument favoring this scenario. This scenario is hereafter named scenario 2. Scenario 1 is Elias 29 having a bipolar outflow with the blue lobe blending in with the blue lobe from LFAM 26, and LFAM 26 having a bipolar outflow as well. For either explanation, there is a large cavity between the source position of LFAM 26 and the outflow material, suggesting a large inclination angle. Both scenarios are adopted in our analysis. Very large CO maps with high spatial resolution are crucial to be conclusive about the interpretation of these two outflow sources.

- Elias 32 and 33 (both located in the same map) have a separation of only 32″, so it is not very clear to which one the observed outflow belongs. The jiggle map is further confused by the lack of data in the south east corner due to the broken receiver. The raster map provides a better map, also because the outflow is now completely covered. Since Elias 33 is somewhat closer to the center of the outflow (the line where the edges of the blue and red outflow meet), the outflow was assigned to this source. This is further discussed in Section 6.3.

- The map with GSS 30-IRS1 and IRS3 is very complex, since the two sources are only 13″ separated, which is less than two pixel elements in this resolution. Besides, CRBR 2324.1-1619 is located just outside the map at the east side, still only 60″ separation. Furthermore, the Class 0 source VLA 1623, which has a very extensive collimated outflow (15′ from north west to south east; Dent et al. (1995); Yu & Chernin (1997)) the outflow is located to the south east of GSS 30 (J2000 coordinates 16:26:26.26, -24:24:30.01) and the outer parts of its outflow are overlapping with the GSS 30 map. No definitive conclusions can be drawn from the map concerning the outflows of the GSS 30 sources. An interferometry study of this region shows local wing emission in HCO^+

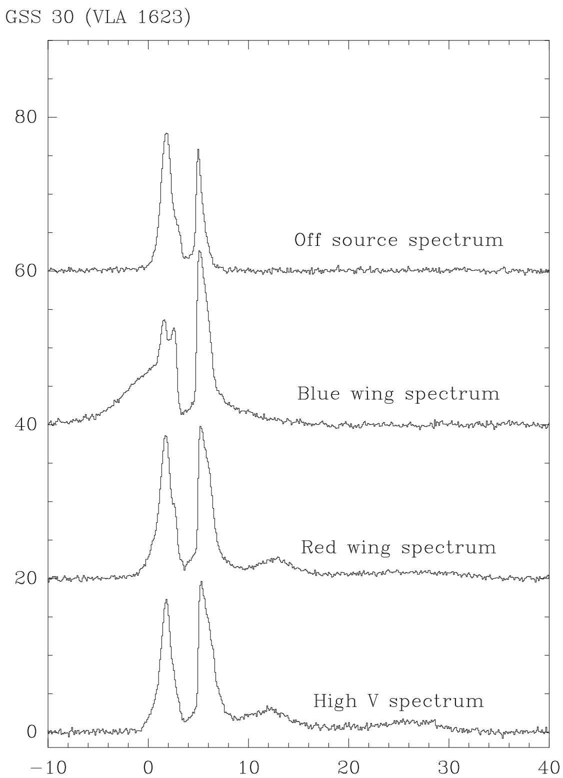

Figure 11: Spectrum with high velocity emission in the GSS 30 map, originating from the Class 0 source VLA 1623.

lines for GSS 30-IRS1 (Jørgensen et al. 2009), but this is not detected in our study. The high velocities and high intensities of the wings indicate that these belong to VLA 1623. In the south, a strong feature shows up in the integrated intensity map, caused by the very high velocity emission feature at 28 km s^{-1}, which is most likely a high-velocity bullet (Bachiller & Tafalla 1999). An overview of spectra in Figure 11 shows this feature in comparison with the normal wings.

- IRAS 16253-2429 is a nice isolated outflow without any signs of other features. The outflow could not be covered within the 2'x2' map, so the values for the size and mass will be lower limits. In a 1.2 mm continuum survey, the Class 0 source MMS126 was identified at nearly the same position as IRAS 16253-2429 (Stanke et al. 2006). Stanke et al. studied additional CO observations and concluded that the outflow, due to the collimated outflow shape, belonged to MMS126, being a Class 0 source. However, the small outflow strength is more typical for a Class I object. Since the outflow properties fit a Class I source just as well, the outflow is associated with IRAS 16253-2429 in this study.

- The map with IRS 37 and WL 3 is centered on IRS 37. The center of the detected outflow in the east is closer to IRS 37 and therefore likely associated with this source. Since WL 3 is very close by, its outflow if existent is completely confused with the one from IRS 37. The red lobe is somewhat hard to determine due to the missing spectra in the south east. In the west a feature shows up with strong blue and red wings, but no IR source is known at this location. This outflow is hereafter referred to as UFO 2. The center of this outflow is about 45" west of the central position, with coordinates 16:27:15.6, -24:28:35.5. A spectral map is given in Figure 14. In the north east blue emission from the Elias 33 outflow shows.

- IRS 43 has a clear nearly pole-on outflow. In the north east, the outer part of the IRS 44 outflow shows up.

- IRS 44 has a bipolar outflow with a non-bipolar morphology. Since the Class II source IRS 46 is located 20" to the north east of IRS 44, it is most likely that the morphology is due to confusion of two outflows, one belonging to IRS 46 (north-south orientation) and one belonging to IRS 44 (north-north-east, south-south-west orientation). It is possible to divide the spectral map in the two parts by a vertical line through a point 10" east of IRS 44, based on the shape of the line wings (see Figure 12 and 6). The wings of IRS 46 are very strong and narrow

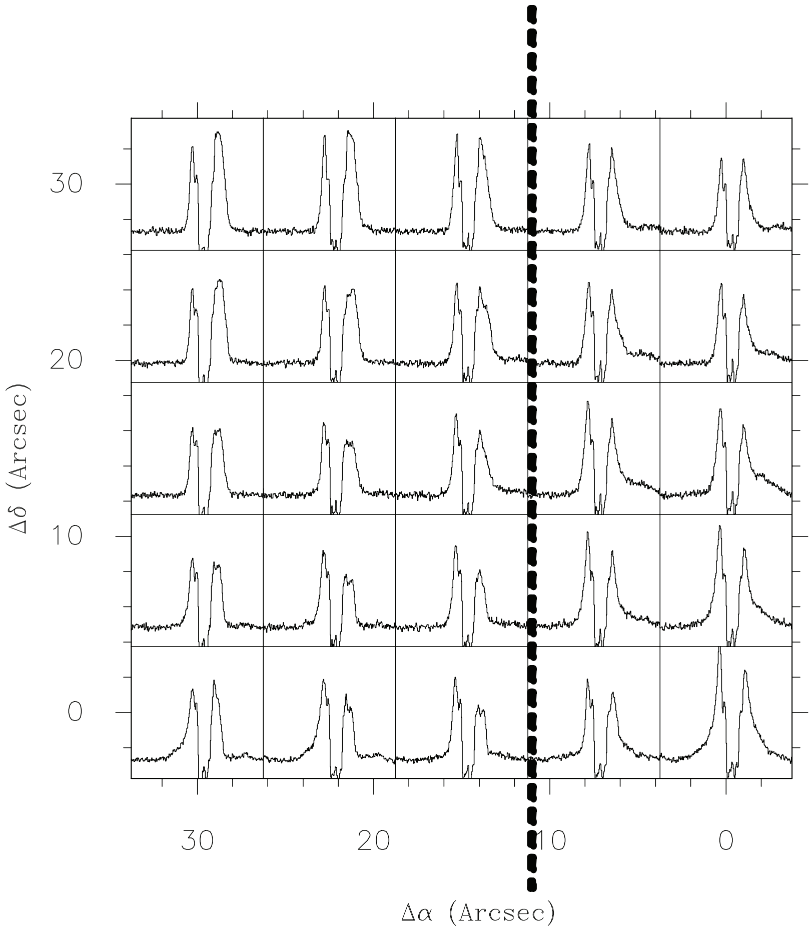

Figure 12: The separation of the two outflows in the IRS 44 spectral map, based on the shape of their spectral wings. The velocity on the horizontal axis ranges from -10 to 15 km s^{-1}, the temperature scale is -2 to 12 K. The wings of IRS 46 (east side) are very strong and narrow (low velocity), while the wings of IRS 44 (west side) are broad and weak compared to the main profile. See also Figure 6 for velocity ranges.

(low velocity), while the wings of IRS 44 are broad and weak compared to the main profile. Due to the small separation of the two sources the outflows are still confused and the spectra mixed up, so this division may underestimate the actual outflow masses. In the south west, a third outflow shows up, with both a red and a blue lobe. No IR source is known at this location, this outflow is hereafter named UFO 5. In the north east, a separate red lobe shows up, again without a known IR source in the neighbourhood. This outflow is hereafter named UFO 6.

- IRS 54 has a bipolar outflow. The blue outflow may not be completely covered and therefore the size underestimated. In the north is a blob of red odd emission, partly hidden by the missing data of the broken receiver, and in the south a blob of blue odd emission. Spectra of the odd emission are given in Figure 8. Although the two lobes are separated by 60", their bipolar structure and similar spectral wings suggest instead of odd emission a second bipolar outflow, originating from about the same position as IRS 54. The large separation may be caused by an inclination nearly along the plane of the sky. This outflow is hereafter named UFO 4. Since its position is about the same as IRS 54, the latter may actually be a binary, or two protostars located along the line of sight.

- IRS 63 is a very isolated source and shows a clear bipolar outflow at the central position. In the south west a feature shows up with strong blue and red wings, but no IR source is known at this location. This outflow is hereafter referred to as UFO 1. The profile of the contours suggest that the central position is beyond the borders of the map, so it is located at least 85" south west of IRS 63. Possible coordinates are 16:31:32.8, -24:03:16.9. A red lobe shows up in the north east, again without a known IR source close by. This outflow is hereafter named UFO 7. A spectral map is given in Figure 13.

- RNO 91 is an isolated source, but the integrated intensity map is very confused. The raster map (right) is clearer than the jiggle map (left) because the blue outflow is quite extended, even the 4'x4' raster map seems not to cover the entire outflow in the south. The red outflow on the other hand is very small. The contours near the edges of the raster map are oddly shaped due to the lack of data in the outer pixels, see the black parts in Figure 3. The outflow is not centered on the source position. Together with the difference in size of the two lobes this indicates that RNO 91 is surrounded by a complex envelope.

- WL 6 has a clear bipolar outflow at the central position. In the north east the outer part of the blue Elias 33 outflow shows.

- WL 12 has a pole-on bipolar outflow. In the east a feature shows up with strong blue and red wings, but no IR source is known at this location. The intensity of these wings is very high, but the bipolar morphology indicates that it is not foreground emission This outflow is hereafter referred to as UFO 3. The center of this outflow is about 50" west and 35" south of the central position, with coordinates 16:26:40, -24:35:27. A spectral map is given in Figure 15.

- WL 17 has a faint outflow, the blue lobe even fainter than the red lobe. In the north east corner, the outflow of Elias 29 shows. Due to the negative absorption it is difficult to determine whether odd emission is present.

The overlap between maps and outflows is shown in Figure 1 of the L1688 core in Ophiuchus, where

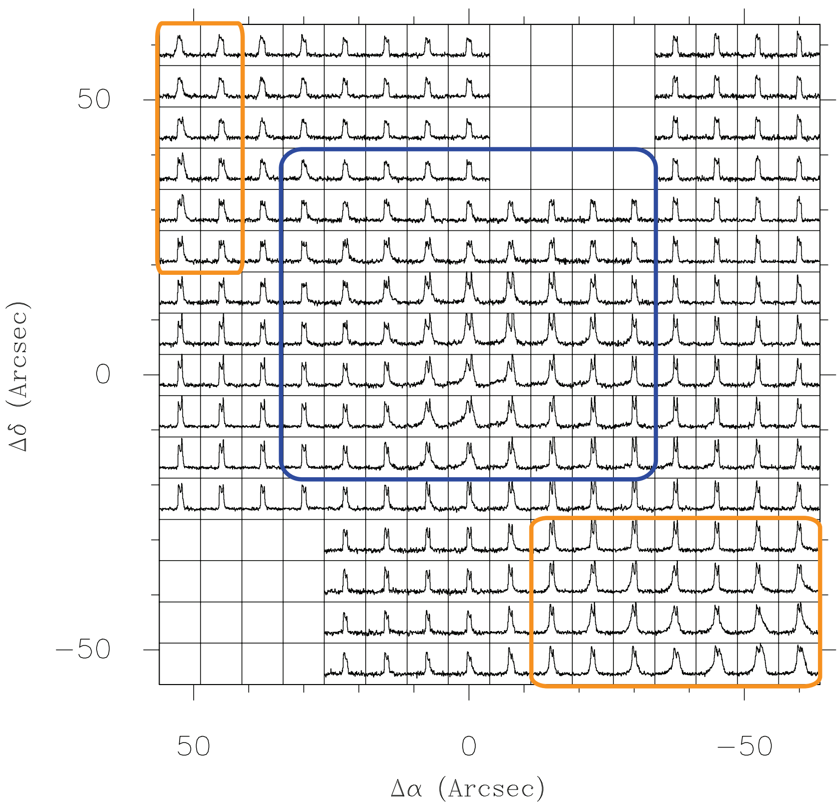

Figure 13: Spectral map of the IRS 63 region showing UFO 1 in the south west and UFO 7 in the north east. The velocity on the horizontal axis ranges from -5 to 10 km s^{-1}, the temperature scale is -2 to 6 K. The outflow spectra of IRS 63 are encircled in blue, the UFOs are encircled in orange.

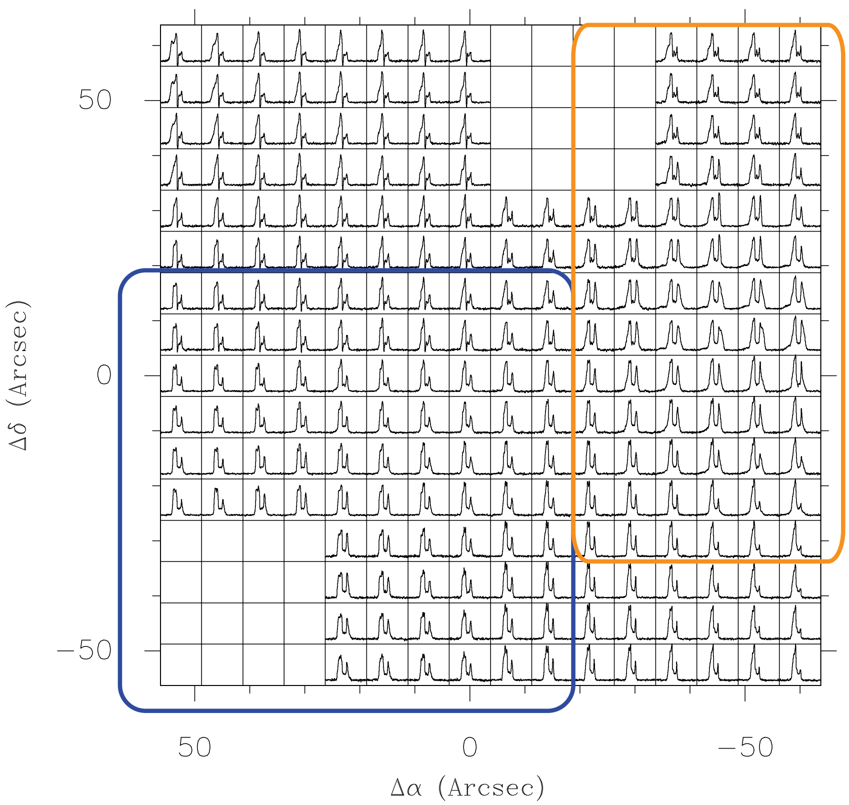

Figure 14: Spectral map of the IRS 37 region showing UFO 2 in the west. The velocity on the horizontal axis ranges from -5 to 15 km s^{-1}, the temperature scale is -2 to 14 K. The outflow spectra of IRS 37 are encircled in blue, the UFO is encircled in orange.

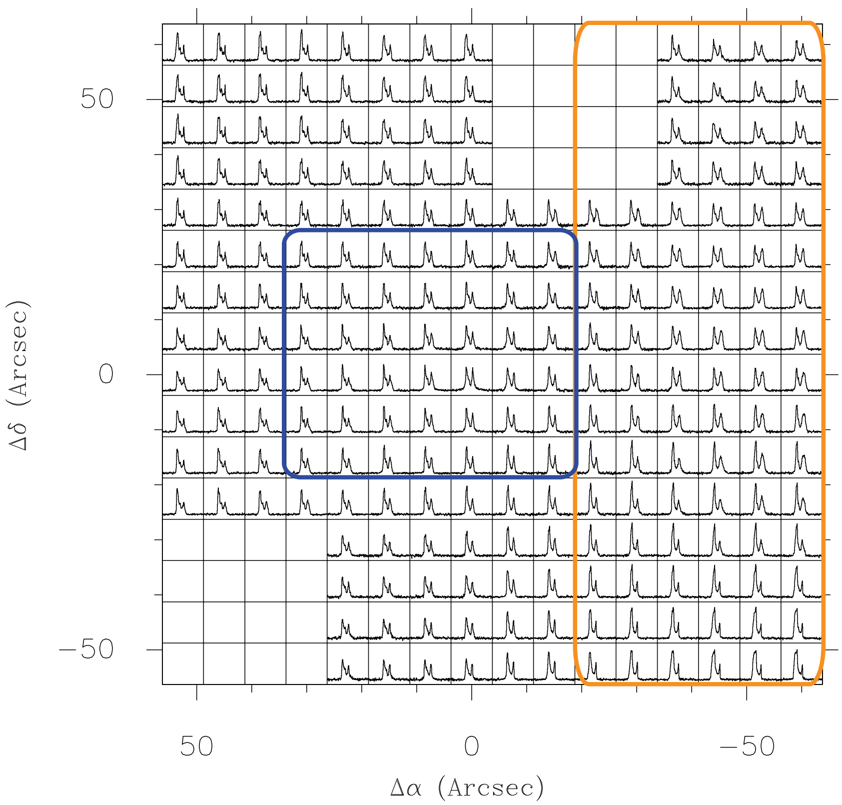

Figure 15: Spectral map of the WL12 region showing UFO 3 in the west. The velocity on the horizontal axis ranges from -5 to 15 km s^{-1}, the temperature scale is -2 to 14 K. The outflow spectra of WL 12 are encircled in blue, the UFO is encircled in orange.

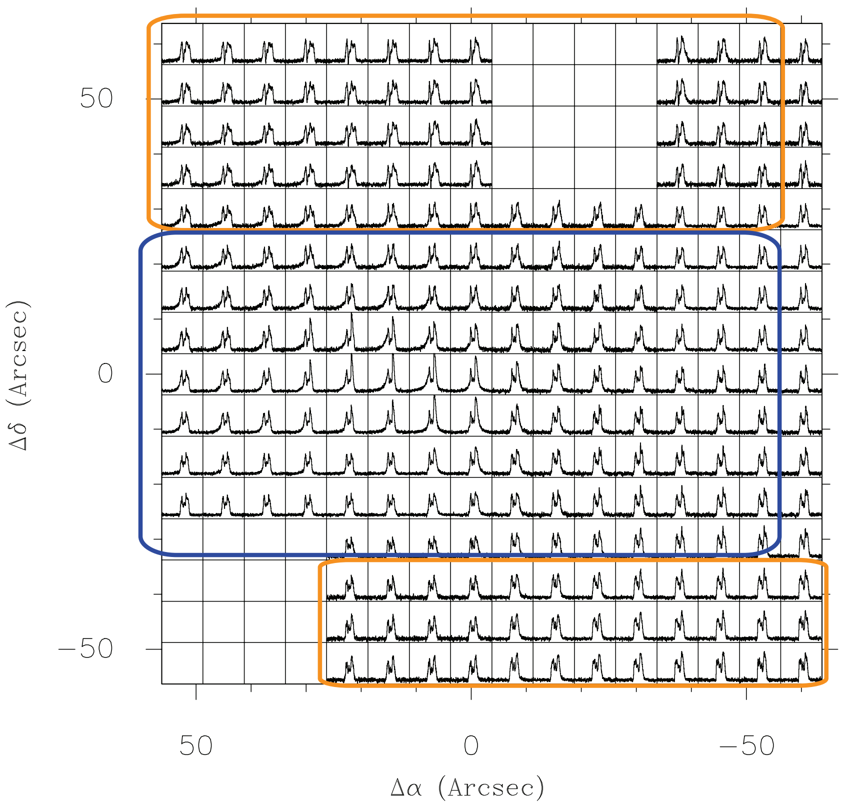

Figure 16: Spectral map of the IRS 54 region showing UFO 4 in the north (red wing) and the south (blue wing). The velocity on the horizontal axis ranges from -10 to 15 km s^{-1}, the temperature scale is -1 to 10 K. The outflow spectra of IRS 54 are encircled in blue, the UFO lobes are encircled in orange

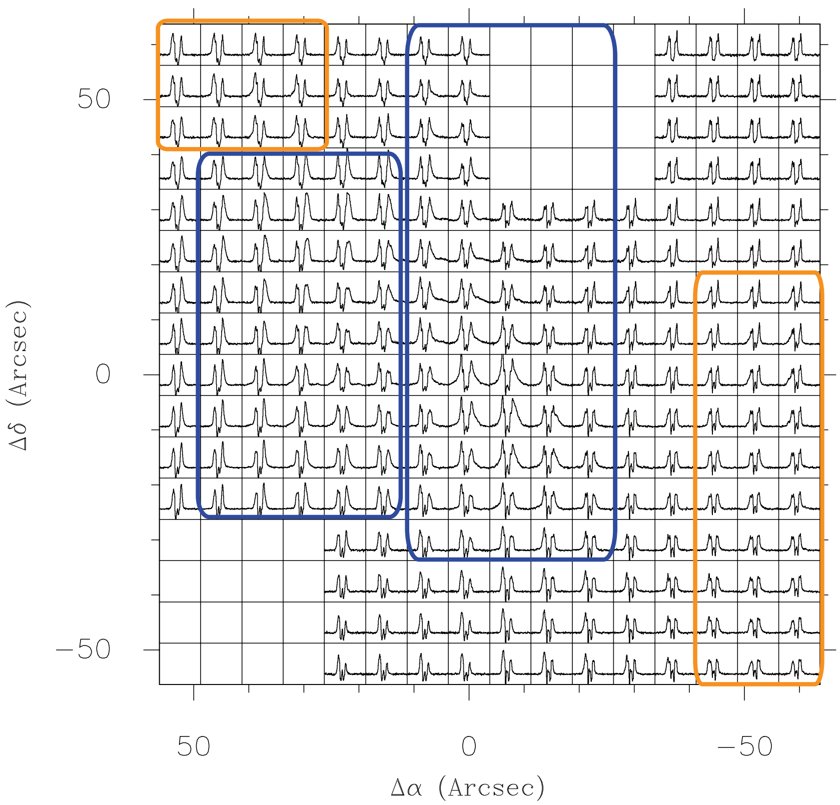

Figure 17: Spectral map of the IRS 44 region showing UFO 5 in the west and UFO 6 in the north east (only blue wing). The velocity on the horizontal axis ranges from -5 to 15 km s^{-1}, the temperature scale is -4 to 12 K. The outflow spectra of IRS 44 and IRS 46 are encircled in blue, the UFOs are encircled in orange

each square represents the actual size of each spectral map and the red and blue arrows show the direction and extent of the red and blue outflows respectively. VLA 1623 is added as well, based on figures in Yu & Chernin (1997). The background shows the 850 μm SCUBA map as published by Johnstone et al. (2000) and Di Francesco et al. (2008). RNO 91 and IRS 63 lie outside the borders of this map. An individual 850 μm SCUBA map with the outflow arrows overplotted is presented in Figure 2.

Based on the outflow maps in Figure 7, an outflow status can be assigned to each source, which is listed in Table 3. The acronyms in column Outflow status are "B" for bipolar outflow and "C" for confusion whether an outflow can be assigned because of the presence of nearby sources. References are given in case the outflow was assigned before and "New" if no earlier outflow assignment was given. Four new outflows were identified, nine were confirmed from previous observations.

Table 3: Outflow status for the 17 sources in this sample.

Source	Outflow status[a]	References[b]
Elias 29	B	1,3
Elias 32/33[c]	B	5
GSS 30-IRS1[d]	C	-
GSS 30-IRS3[d]	C	-
IRAS 16253-2429	B	New
IRS 37	B	New
IRS 43	B	1
IRS 44	B	1
IRS 46	B	New
IRS 54	B	New
IRS 63	B	1[e,f]
LFAM 26	B	3
RNO 91	B	2,4
WL 3	C	-
WL 6	B	6
WL 12	B	1[e]
WL 17	B	New

a Outflow status: "B" for bipolar outflow and "C" for confusion whether an outflow can be assigned because of the presence of nearby sources. Of these latter sources, only WL 3 was not studied for an outflow before, GSS 30 and Elias 32/33 were assigned confused before.

b References: [1] Bontemps et al. (1996), [2] Arce & Sargent (2006), [3] Bussmann et al. (2007), [4] Cabrit & Andre (1991), [5] Kamazaki et al. (2003), [6] Sekimoto et al. (1997)

c Due to the small separation of Elias 32 and 33, it is not clear to which source the outflow belongs. Elias 33 was assigned as the driving source in this study.

d Confusion with the outflow from the Class 0 source VLA 1623.

e IRS 63 is named L1709B (name of the core) or 16285-2355 in Bontemps et al. (1996).

f IRS 63 and WL 12 were not recognized as bipolar in Bontemps et al. (1996).

5.3 Orientation and correction factors

Position angles of the outflows are derived from the maps and are listed in Table 5. For IRS 37, IRS 44 and WL 6 the lobes are not exactly opposite, so assigning a position angle is less meaningful. Position angles are especially useful in searches for disks, which are orientated perpendicular to the outflow direction. Other morphology properties such as collimation (length divided by width) and opening angle strongly depend on inclination and could not be determined for lack of accurate values of the inclination angle.

The mass of the outflow should be corrected for the optical depth $\tau_{\rm wing}$, by a factor $\frac{\tau}{1-e^{-\tau}}$ (Bontemps et al. 1996). The optical depth is determined with the abundance ratio between isotopologues X, e.g. [^{12}CO]:[^{13}CO] = 70 (Wilson & Rood 1994), and the intensity ratio $r = ^{12}$CO/^{13}CO, for the same J transition line. If the line is optically thin, r is equal to X, but if the line is optically thick, r is equal to $X/\tau(^{12}\mathrm{CO})$, which determines τ (Bachiller & Tafalla 1999). Depending on the available data, one can decide on assuming optical thin line wings, resulting in a lower limit for the outflow mass, or calculating the opacity and applying the correction, which will even result in an upper limit for the outflow mass, because τ changes with position and velocity (Cabrit & Bertout 1990; van Kempen et al. 2009a). Typical values for $\tau_{\rm wing}$ for low-J ^{12}CO in other outflow studies range from <1 (optically thin) up to 18.4 (Hogerheijde et al. 1998; Cabrit & Bertout 1992). Bontemps et al. (1996) decided on a mean correction factor of 3.5 on their entire sample assuming all wings optically thick in ^{12}CO 2-1 observations, based on the mean $\tau_{\rm wing}$ value found by Cabrit & Bertout (1992) on another sample. The only available isotopologue CO data for the Ophiuchus sample is C^{18}O (van Kempen et al. 2009c), but this is inconvenient for determining the optical depth because it is typically 550 times less abundant than ^{12}CO (Wilson 1999) and wings are not visible in any of the spectra. The line wings are assumed to be optically thin, so all the calculated masses and derived physical properties are lower limits.

The inclination of an outflow, which is defined as the angle between the outflow direction and the line of sight (Cabrit & Bertout 1990), is roughly estimated from the morphology of the contour maps and the position-velocity diagrams (Figure 4). For the UFOs, no inclination could be derived because they were not spatially covered by the maps. The inferred inclinations are given in Table 5. Cabrit & Bertout (1990) modeled these output diagrams for four different configurations, with inclination angles of 10°, 50° and 70° and a cone opening angle of 30° and 60° (latter only for i=50°). For i >70°, the velocity component along the line of sight becomes so small that no outflow emission is detected. In the follow-up paper, Cabrit & Bertout (1992) described the effects of inclination to $R_{\rm CO}$ and $v_{\rm CO}$ and concluded these parameters cannot be corrected by simple factors, because of the strong dependence on opening angle and velocity field. Correction factors for the energetic parameters (see next section) could be derived. A different approach with a mean inclination correction factor, for lack of complete CO maps, was used by Bontemps et al. (1996), but this is less accurate than the method described above, as further discussed in Section 6.

5.4 Energetic parameters

A set of energetic parameters was derived (Cabrit & Bertout 1990, 1992) and used in several outflow studies (Bontemps et al. 1996; Hogerheijde et al. 1998; Hatchell et al. 2007; van Kempen et al. 2009b). The most important are the momentum flux or force $F_{\rm CO}$ along a flow and the kinetic luminosity $L_{\rm kin}$, defined as:

$$F_{\rm CO} = \frac{MV_{\rm CO}^2}{R_{\rm CO}} \quad (6)$$

$$L_{\rm kin} = \frac{\frac{1}{2}MV_{\rm CO}^3}{R_{\rm CO}} \quad (7)$$

These energetic parameters are very convenient because they can be estimated even with incomplete maps of the outflow (Bontemps et al. 1996). Since outflows from low-mass YSOs are thought to be momentum-driven (Cabrit & Bertout 1992), the outflow force should be conserved along the outflow direction. The outflow force is a very important parameter in evolutionary studies of star formation, as will be discussed extensively in the next section. For both parameters, correction factors for inclination are derived (Cabrit & Bertout 1992). In addition to the correction factors in Table 1 in Cabrit & Bertout (1992), the velocity component was corrected in the calculation of $F_{\rm CO}$ and $L_{\rm kin}$ in case the inclination angle is high (70°) with an additional factor $1/cos(i-\theta)$, with θ the opening angle, which is usually taken as 30°. The corrected values are given in Table 5. Other outflow parameters are the dynamical time $t_{\rm D}$ and the mass outflow rate $\dot{M}$, defined as:

$$t_D = R_{\rm CO}/v_{\rm CO} \quad (8)$$

$$\dot{M} = M/t_{\rm d} \quad (9)$$

The dynamical time is a very rough estimate because it assumes that both $R_{\rm CO}$ and $v_{\rm CO}$ did not change over time and that the maximum velocity is the same everywhere. Both parameters were not corrected for inclination.

5.5 Error margins $F_{\rm CO}$

For determining the errors on the momentum flux $F_{\rm CO}$, several factors have to be taken into account:

Table 4: *Outflow parameters from ^{12}CO observations for separate blue and red lobes*

Blue lobe							
Name	$v_{\rm CO}$ (km s^{-1})	$R_{\rm CO}$ (10^{3}AU)	M (10$^{-4}M_\odot$)	$t_{\rm d}$ (10^3 yr)	$\dot{M}$ (10^{-7} $M_\odot$yr^{-1})	$F_{\rm obs}$ (10$^{-6}M_\odot$ km s^{-1}yr^{-1})	$L_{\rm obs}$ (10$^{-5}L_\odot$)
Elias 29 (scen 1)[a]	8.7	7.5	9.5	4.1	2.3	9.7	4.2
Elias 29 (scen 2)[a]	9.0	14	29	7.4	3.9	17	7.5
Elias 33	10	29	280	13	21	104	53
IRAS 16253-2429	5.3	10	1.5	9.1	0.2	0.4	0.1
IRS 37	5.6	5.0	1.6	4.3	0.4	1.0	0.3
IRS 43	7.6	3.9	2.2	2.4	0.9	3.2	1.2
IRS 44	8.1	7.7	4.1	4.5	0.9	3.5	1.4
IRS 46	7.2	5.1	3.5	3.4	1.0	3.5	1.3
IRS 54	11	10	12	4.4	2.7	14	7.7
IRS 63	9.7	6.8	4.5	3.3	1.3	6.2	3.0
LFAM 26 (scen 1)[a]	8.6	10	20	5.6	3.6	15	6.3
LFAM 26 (scen 2 east)[a]	5.1	15	2.9	14	0.2	0.5	0.1
LFAM 26 (scen 2 west)[a]	5.1	10	2.5	9.5	0.3	0.6	0.2
RNO 91	9.5	22	110	11	9.7	44	21
WL 6	6.9	4.5	2.9	3.1	0.9	3.1	1.1
WL 12	6.1	7.1	1.3	5.5	0.2	0.7	0.2
WL 17	4.6	7.5	0.3	7.7	0.0	0.1	0.0
UFO 1 (IRS 63)[b]	4.0	5.1	1.3	6.1	0.2	0.4	0.1
UFO 2 (IRS 37)[b]	7.8	7.7	6.7	4.7	1.4	5.4	2.1
UFO 3 (WL 12)[b]	3.8	7.1	2.5	8.9	0.3	0.5	0.1
UFO 4 (IRS 54)[b]	4.3	7.9	4.7	8.7	0.5	1.1	0.2
UFO 5 (IRS 44)[b]	5.4	2.7	1.2	2.4	0.5	1.3	0.4
UFO 6 (IRS 44)[b]	5.9	3.6	1.0	2.9	0.4	1.0	0.3
UFO 7 (IRS 63)[b]	-	-	-	-	-	-	-

Red lobe

Name	$v_{\rm CO}$ (km s^{-1})	$R_{\rm CO}$ (10^{3}AU)	M (10$^{-4}M_\odot$)	t_d (10^3 yr)	$\dot{M}$ (10^{-7} $M_\odot$yr^{-1})	$F_{\rm obs}$ (10$^{-6}M_\odot$ km s^{-1}yr^{-1})	$L_{\rm obs}$ (10$^{-5}L_\odot$)
Elias 29 (scen 1)[a]	6.7	9.1	13	6.5	2.0	6.4	2.1
Elias 29 (scen 2)[a]	6.7	9.1	13	6.5	2.0	6.4	2.1
Elias 33	9.5	29	380	14	27	120	57
IRAS 16253-2429	5.2	8.9	5.8	8.2	0.7	1.8	0.5
IRS 37	3.8	7.9	2.2	9.8	0.2	0.4	0.1
IRS 43	6.8	4.5	4.0	3.1	1.3	4.2	1.4
IRS 44	13	7.8	12	2.9	4.1	25	16
IRS 46	6.4	5.0	16	3.7	4.3	13	4.2
IRS 54	8.2	6.0	4.2	3.5	1.2	4.7	1.9
IRS 63	4.0	6.6	2.5	7.9	0.3	0.6	0.1
LFAM 26 (scen 1)[a]	7.0	10	9.6	6.9	1.4	4.6	1.6
LFAM 26 (scen 2 east)[a]	13	15	27	5.5	5.0	30	19
LFAM 26 (scen 2 west)[a]	13	10	9.9	3.8	2.6	16	10
RNO 91	4.5	14	6.7	15	0.5	1.0	0.2
WL 6	10	8.3	7.5	3.8	2.0	9.8	5.1
WL 12	5.8	4.6	2.0	3.8	0.5	1.5	0.4
WL 17	5.0	3.4	0.6	3.2	0.2	0.5	0.1
UFO 1 (IRS 63)[b]	4.7	4.5	2.3	4.5	0.5	1.1	0.3
UFO 2 (IRS 37)[b]	5.2	7.7	9.9	7.0	1.4	3.5	0.9
UFO 3 (WL 12)[b]	4.6	13	10	13	0.8	1.7	0.4
UFO 4 (IRS 54)[b]	5.2	7.9	12.0	7.2	1.7	4.1	1.1
UFO 5 (IRS 44)[b]	6.0	2.7	0.9	2.1	0.4	1.3	0.4
UFO 6 (IRS 44)[b]	-	-	-	-	-	-	-
UFO 7 (IRS 63)[b]	3.7	1.8	0.53	2.3	0.23	0.4	0.07

These values are not corrected for inclination.

a Scenario 1 implies that LFAM 26 has a red and blue lobe, the blue lobe of Elias 29 blends in with the blue lobe of LFAM 26. For scenario 2 (Bussmann et al. 2007), the blue lobe of Elias 29 is very extended, LFAM 26 has two opposite red lobes and faint blue lobes, possibly forming a quadrupolar outflow. All lobes are analyzed separately for this table.

b Newly discovered outflows (UFOs) not associated with an IR source. In round brackets, the IR source to which the UFO is closest is given.

Table 5: Outflow parameters from ^{12}CO observations

Name	i (°)	P.A. (°)	$t_{\rm d}^{a,b}$ (10^3yr)	$\dot{M}^{a,b}$ ($10^{-7}M_\odot$ yr^{-1})	$F_{\rm CO}^c$ ($10^{-6}M_\odot$ km s^{-1}yr^{-1})	$L_{\rm kin}^c$ ($10^{-5}L_\odot$)	$L_{\rm bol}^d$ ($10^{-1}L_\odot$)	$M_{\rm env}^d$ ($10^{-2}M_\odot$)
Elias 29 (scen 1)^e	50	150	4.1	2.3	16	6.3	25	6.2
Elias 29 (scen 2)^e	50	150	7.4	3.9	23	9.6	25	6.2
Elias 33	70	105	13	21	430	330	12	28
IRAS 16253-2429	70	30	9.1	0.2	4.1	1.7	0.6	10
IRS 37	50	50^f	4.3	0.4	1.4	0.4	3.8	1.2
IRS 43	10	135	2.4	0.9	7.4	2.7	10	17
IRS 44	30	20	4.5	0.9	29	17	11	8.0
IRS 46	50	0	3.4	1.0	17	5.5	1.9	3.3
IRS 54	50	40	4.4	2.7	19	9.7	7.8	3.1
IRS 63	30	70	3.3	1.3	6.8	3.1	13	16
LFAM 26 (scen 1)^e	70	60	5.6	3.6	37	24	0.4	4.5
LFAM 26 (scen 2)^{e,g}	70	80	14	0.2	90	90	0.4	4.5
RNO 91	50	135	11	9.7	45	21	37	1.0
WL 6	50	30^f	3.1	0.9	13	6.2	8.5	0.4
WL 12	30	140	5.5	0.2	2.2	0.6	34	4.6
WL 17	50	155	7.7	0.0	0.5	0.1	6.7	4.0
UFO 1 (IRS 63)^a	-	-	6.1	0.2	1.5	0.3	-	-
UFO 2 (IRS 37)^a	-	30	4.7	1.4	8.8	3.0	-	-
UFO 3 (WL 12)^a	-	0	8.9	0.3	2.3	0.5	-	-
UFO 4 (IRS 54)	70	20	8.7	0.5	5.2	1.3	-	-
UFO 5 (IRS 44)^a	-	0	2.4	0.5	2.6	0.7	-	-
UFO 6 (IRS 44)^a	-	-	2.9	0.4	1.0	0.3	-	-
UFO 7 (IRS 63)^a	-	-	1.8	0.23	0.4	0.07	-	-

a Not corrected for inclination.

b Average of blue and red lobe.

c Sum of blue and red lobe and inclination corrected.

d Values taken from literature (van Kempen et al. 2009c; Chen et al. 1995; Arce & Sargent 2006).

e Scenario 1 implies that LFAM 26 has a red and blue lobe, the blue lobe of Elias 29 blends in with the blue lobe of LFAM 26. For scenario 2 (Bussmann et al. 2007), the blue lobe of Elias 29 is very extended, LFAM 26 has two opposite red lobes and faint blue lobes, possibly forming a quadrupolar outflow.

f Outflow lobes not in opposite direction: position angle confused.

g The eastern and western lobes of LFAM 26 were summed or averaged.

- The line wings were assumed to be optically thin, for lack of isotope observations. If optically thick line wings were assumed, an estimate of the opacity τ is 5.4, based on the mean τ of 3.5 as found by Cabrit & Bertout (1992) for the ^{12}CO 2-1 lines, multiplied by 1.6 in order to compensate for the 3-2 instead of the 2-1 transition. An even higher mean value for $\tau_{\rm wing}$ of 7.1 was found (Hogerheijde et al. 1998) in an actual ^{12}CO 3-2 outflow study of Class I objects in Taurus, but to keep in line with other outflow studies who use the mean of 3.5 (or 5.4) this value is taken as upper limit. The values for $F_{\rm CO}$ in this study are therefore underestimated by a factor of 5.4, considering opacity.

- The correction factors for inclination as derived by Cabrit & Bertout (1992) have uncertainties as well, as shown in Figure 21. The uncertainties are large for i=30° and i=70°. However, since the determination of the inclination was only based on visual inspection of the contour maps, the same error margin was applied to i=10, 30 and 50°, because these are difficult to distinguish. The error margins of the correction factors give both upper and lower limits based on inclination. Following the absolute error values given in Cabrit & Bertout (1992), this is a factor of about 2 uncertainty for i=10, 30 and 50° and values in between 0.15 and 2.4 times the calculated value for i=70°.

- The momentum flux is independent of the spatial coverage of the outflow in the spectral map, since it depends both on the integrated spectral line wings (mass) and the radius as spatially covered. However, in the case that the outflow lobes are not completely covered due to the lack of data from the broken receivers, the entire mass of the outflow lobe can not be derived and will be underestimated. This is the case for IRS 37 and Elias 29, in both cases about 25 percent of the spectra belonging to the outflow lobe is missing and the mass will be underestimated by a factor 1.25.

- The integration limits are typically chosen so that only the wings are integrated. However, without actual subtraction of the central envelope spectral profile, some envelope material will be included in the mass derivation as well. A comparison between integrated intensities of line wings with and without subtraction of a Gaussian fit for the envelope gives about a factor of 1.5. The derived masses of the outflow lobes are therefore overestimated by a factor 1.5.

- The assumed temperature $T_{\rm ex}$ for the calculation of the column density is taken as 100 K, while it may range from 20 to 150 K. As shown in Figure 5 the error in this factor ranges from a factor 0.8 to 1.4 and puts both upper and lower limits on the momentum flux.

Clearly, the opacity and inclination factors contribute the most to the errors in the values for $F_{\rm CO}$, especially for a large inclination angle.

5.6 Relations with outflow force

In order to get a better understanding of the processes involved in star formation and the outflow driving mechanism in particular, the outflow strength is often plotted versus physical properties of the source to find correlations. Correlations indicate either a direct relation (cause and effect) or a joint cause for both parameters. Correlations are also an excellent way to see evolutionary effects.

In outflow studies, two main trends are usually explored: the momentum flux versus the mass of the envelope and the momentum flux versus the bolometric luminosity. The bolometric luminosity for Class 0/I YSOs is dominated by accretion luminosity. These plots for this study are given in Figure 18. Error bars as discussed in the section above are overplotted on the data points. In these plots and the remaining part of the report, the outflow parameters of scenario 2 as discussed above are adopted for Elias 29 and LFAM 26. The results from other studies are overplotted in different colors without error bars. The dashed lines in the plots are the best linear fits to the log-log relations per data set, the dotted lines are the linear fit for the combined data sets,

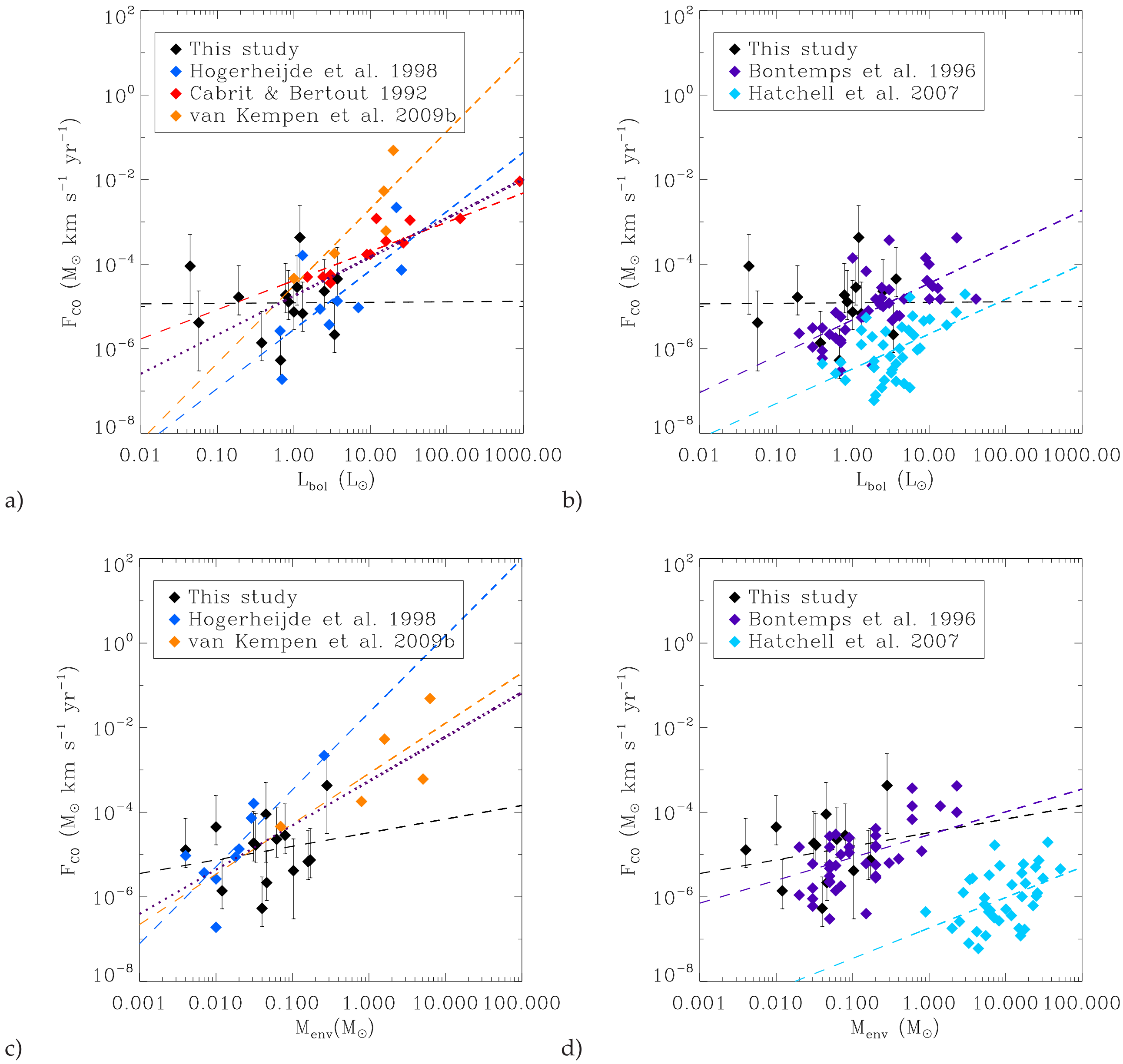

Figure 18: Correlation plots for the momentum flux $F_{\rm CO}$, bolometric luminosity $L_{\rm bol}$ and the mass of the envelope $M_{\rm env}$. Figures a and c have additional data points taken from Cabrit & Bertout (1992), Hogerheijde et al. (1998) and van Kempen et al. (2009b), where $F_{\rm CO}$ was calculated by a similar method as ours. On Figures b and d, data points from Bontemps et al. (1996) and Hatchell et al. (2007) are added, but their derivations are so different from ours that the data sets cannot be combined (see text). Data points from this study are black, data from the other studies are plotted in different colors as indicated in the legend. The dashed lines indicate the best linear fit to the data set. The dotted line indicates the best linear fit to the entire set of Class I objects.

with the exclusion of Cabrit & Bertout (1992) since these are Class 0 sources, which are known to have significantly higher momentum flux (e.g. Bontemps et al. (1996)). The plots on the left contain only data from studies where the same method of momentum flux derivation was used, i.e. Cabrit & Bertout (1992) (selection of strong Class 0 sources), Hogerheijde et al. (1998) (Taurus, Class I) and van Kempen et al. (2009b) (Chamaeleon and Corona Australis, Class I), in terms of summing integrated wing intensities and use of inclination correction factors (Cabrit & Bertout 1992). Hogerheijde et al. (1998) and Cabrit & Bertout (1992) derived the opacity of the line wings and applied a correction, while our study and van Kempen et al. (2009b) had no possiblities to derive the opacity and assumed optically thin line wings. For the latter studies the values for $F_{\rm CO}$ are therefore a lower limit. The plots on the right contain the data sets taken from Bontemps et al. (1996) (selected sample of Ophiuchus, Taurus, Perseus and other, Class 0 and I) and Hatchell et al. (2007) (Perseus, Class 0 and I), whose methods are significantly different. Bontemps et al. (1996) subtracted an average envelope spectral profile from the outflow spectra to get rid of the envelope emission in the line wings, summed only the spectra within a small radius and corrected all sources with the same inclination correction and opacity correction (means of earlier studies). Hatchell et al. (2007) did not apply any correction for inclination or opacity so their values of $F_{\rm CO}$ are strictly lower limits. Besides, they used a different method than Bontemps et al. (1996) called momentum flux beam calculation and did not subtract an envelope spectral profile, but the main difference with Bontemps et al. (1996) is the constant correction factor. Since these methods are so different, their data sets cannot be combined with the others for a trend over a larger span of $L_{\rm bol}$ and $M_{\rm env}$.

The well-known relationship between momentum flux and bolometric luminosity is not that evident from the results of our study. The best linear fit through our datapoints is:

$$\log(F_{\rm CO}) = -4.9 + 0.11\log(L_{\rm bol}) \tag{10}$$

The fits for the other datasets on the other hand indicate a strong correlation, with $\log(F_{\rm CO}) \propto \log(L^k_{\rm bol})$, with k 1.4 for Hogerheijde et al. (1998), 1.8 for van Kempen et al. (2009b), 0.7 for Cabrit & Bertout (1992) and 0.9 for both Bontemps et al. (1996) and Hatchell et al. (2007). The three data points with $L_{\rm bol} < 0.5L_\odot$ from our dataset (IRAS 16253-2429, LFAM 26 and IRS 46) are clearly outliers from the stronger correlation, because exclusion of these three points results in:

$$\log(F_{\rm CO}) = -5.0 + 0.86\log(L_{\rm bol}) \tag{11}$$

This strong change of correlation indicates that the relation is not constant over the entire luminosity range, but 'flattens' at the lowest luminosities. The uncertainty in this fit is comparable to the individual fits ($\chi^2 < 6.0$), indicating a good agreement between our results and the ones from literature for $L_{\rm bol} > 0.5L_\odot$. The best fit for the combined data set of the three studies (dotted line) is:

$$\log(F_{\rm CO}) = -4.8 + 0.92\log(L_{\rm bol}) \tag{12}$$

The results from Cabrit & Bertout (1992) are excluded since these are Class 0 sources. Due to the large sample, the effect of the three low-luminosity outliers on the fit becomes very small, resulting in a much tighter correlation than just our sample. However, the significance of the momentum flux for low luminosity objects should be explored.

A second well-known relationship is the correlation between envelope mass and momentum flux, as given in Figure 18 c and d. Again, the results from other studies are overplotted with different colors, and linear fits are derived for each dataset. Envelope masses were not studied by Cabrit & Bertout (1992). The relationship is clearly tighter than for the $F_{\rm CO} - L_{\rm bol}$ relation and agrees reasonably well with previous works. The best linear fit through our data points is:

$$\log(F_{\rm CO}) = -4.5 + 0.32\log(M_{\rm env}) \tag{13}$$

The parameter m in $\log(F_{\rm CO}) \propto \log(M^m_{\rm env})$ is different from Hogerheijde et al. (1998) (1.8) and van Kempen et al. (2009b) (1.19) but this may be due to the small range of envelope masses or the way of calculating the envelope mass and choice of outer radius: our envelope mass calculation was based on

SCUBA 850 μm emission (van Kempen et al. 2009c), while Hogerheijde et al. (1998) and van Kempen et al. (2009b) based their envelope mass on 1.3 mm emission. The best fit for the entire sample is:

$$\log(F_{\rm CO}) = -3.3 + 1.1 \log(M_{\rm env}) \qquad (14)$$

Another correlation with the momentum flux is the free-free radio continuum emission (6 cm) (Cabrit & Bertout 1992). Unfortunately, 6 cm emission data are only available for the Oph-A region (Leous et al. 1991; Gagné et al. 2004) where GSS 30 is located, but no outflow was detected for this source, and the Oph-E,F region, the southern ridge with e.g. IRS 43, IRS 44, Elias 29 and LFAM 26 (Leous et al. 1991). For these four sources, the $F_{\rm CO}$ vs the distance-corrected $S_{\rm 6cm}$ ($S_{\rm 6cm} \cdot d^2$) is plotted in Figure 19, together with the values found by Cabrit & Bertout (1992). The data points of our study are in agreement with the correlation found by Cabrit & Bertout (1992). Note that the axes are switched compared to Figure 3 in Cabrit & Bertout (1992).

Finally, we checked for a correlation between the dense gas in the inner regions of protostellar envelopes, as traced by HCO$^+$, and the momentum flux. The integrated HCO$^+$4 $-$ 3 intensity was used as a new tool for classification in Stages (van Kempen et al. 2009c). It provides a better evolutionary parameter than $M_{\rm env}$ because the latter is easily affected by cold outer envelopes, disks and cloud material. The $\int T_{\rm mb}\, {\rm d}v$ is plotted versus $F_{\rm CO}$ in Figure 20. No data were available from other studies.

There is a very good correlation between the momentum flux and the dense gas. The best linear fit for this dataset is:

$$\log(F_{\rm CO}) = -5.2 + 0.95 \log(M_{\rm env}) \qquad (15)$$

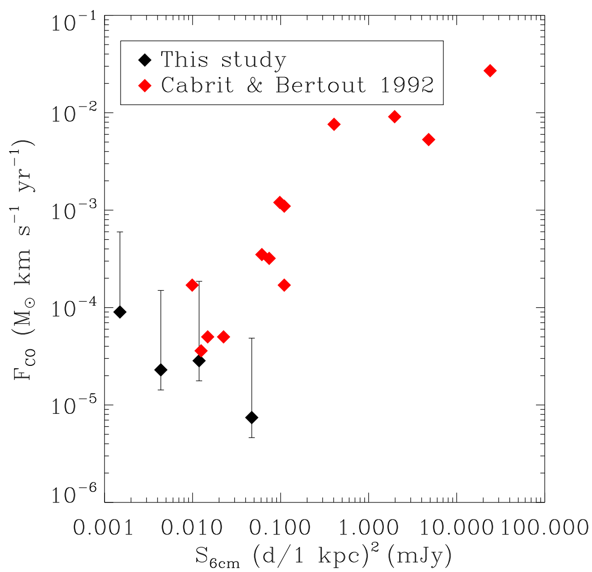

Figure 19: Distance-corrected free-free $S_{\rm 6cm}$ flux plotted versus the momentum flux. $S_{\rm 6cm}$ values were taken from Leous et al. (1991). The red data points, taken from Cabrit & Bertout (1992), are added for comparison. The results from our study confirm the correlation found by Cabrit & Bertout (1992).

6 Discussion

The results for this study in Ophiuchus provide the tools for the discussion of several aspects of outflow studies. We will first discuss the implication of the trends from the last section. Then, the entire outflow sample is described in terms of classification and triggering of star formation. Furthermore, the outflow results will be compared to results from previous outflow studies, disk studies and other outflow tracers like H_2 knots and Herbig Haro objects. A candidate search for the UFOs will be presented as well.

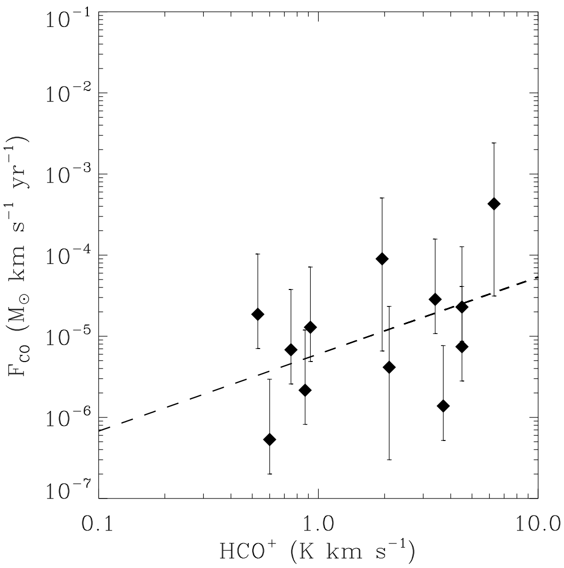

Figure 20: The momentum flux versus the integrated intensity of HCO$^+4-3$, taken from van Kempen et al. (2009c). The dashed line is the best linear fit through the datapoints. HCO$^+$ is an excellent dense gas tracer and evolutionary parameter. IRS 46 and RNO 91 were not included in this plot: the latter was not measured by van Kempen et al. (2009c), the second was undetected in HCO$^+$.

6.1 Trends and evolution

The results for the relation between $F_{\rm CO}$ and $L_{\rm bol}$ do not extend the correlation found in previous works to lower values for $L_{\rm bol}$. In the past, a correlation over a large span of luminosities was found, indicating that the driving mechanism for molecular outflows is directly related to the accretion process, since the bolometric luminosity of a YSO is thought to be dominated by accretion luminosity. It also depends on the stellar mass and the viewing angle, explaining its less tight relation with $F_{\rm CO}$ compared to the $M_{\rm env}$ relation (Hogerheijde et al. 1998). It is widely believed that outflows are momentum-driven by a jet or wind originating from the inner envelope or protostar. The most plausible energy source for this jet or wind is the gravitational energy released by accretion onto the protostar. Accordingly, the momentum flux is directly related to the accretion rate $\dot{M}_{\rm acc}$ (Bontemps et al. 1996). However, with our new results for very low luminosity objects for which the correlation with momentum flux disappears, the theory may be incorrect for these low luminosities. One possibility is so-called episodic accretion, where the accretion rate is variable with time (Evans et al. 2009), i.e., $F_{\rm CO}$ remains high while $L_{\rm bol}$ becomes low. This solution applies if the swept-up material does not slow down too quickly even when the driving force has (temporarily) disappeared.

The three outliers from the $k \sim 0.7$ correlation in the $F_{\rm CO}$-$L_{\rm bol}$ plot with $L_{\rm bol} < 0.5 L_\odot$ should also be considered as actual outliers in our data set. The sources are IRAS 16253-2429, LFAM 26 and IRS 46, for which the outflow is actually debatable. The outflow assigned to the IRAS 16253-2429 position may also belong to the potential Class 0 candidate MMS126 (Stanke et al. 2006), resulting in lack of outflow activity of IRAS 16253-2429 itself. The bolometric luminosity of MMS126 was not derived by Stanke et al. (2006) but the correlation between $F_{\rm CO}$ and $L_{\rm bol}$ is known to lie an order of magnitude above the correlation for Class I sources (Bontemps et al. 1996) so if the outflow belongs to MMS 126 it should be excluded from our Class I sample. The outflow from LFAM 26 was only partly spatially covered, as discussed in Section 5.2. Bussmann et al. (2007) covered the entire outflow region for LFAM 26 and calculated a momentum flux of only $15{\cdot}10^{-6}\mathrm{M_\odot kms^{-1}yr^{-1}}$ compared to $90{\cdot}10^{-6}\mathrm{M_\odot kms^{-1}yr^{-1}}$ in our calculation. This is further discussed in Section 6.2, but this coverage may decrease the observed mass and outflow strength and make it consistent with the general correlation. Finally, IRS 46 is not a Class I but a Class II source, and may not belong to this relationship. This is further discussed in Section 6.3.

The mass of the envelope is an evolutionary parameter, and therefore an excellent tracer of evolution of the outflow momentum flux. The correlation found for the $F_{\rm CO} - M_{\rm env}$ relation confirms previous results stating that the momentum flux decreases with evolution. This is even further confirmed by the relation with the integrated HCO^+ emission, tracing the dense gas.

The correlation between the momentum flux and the free-free $S_{\rm 6cm}$ emission gives evidence that molecular flows and radio continuum emission may be related in YSOs, since the $S_{\rm 6cm}$ emission is presumed to arise at the region of interaction between the wind and the molecular outflow. However, the limited number of extra data points provides no new information on this relation, it only gives further confirmation of the wind models described by Cabrit & Bertout (1992).

Summarizing, the evolutionary plots confirm previous results for the momentum flux, but the driving mechanism is debatable due to the weaker correlation between accretion and outflow strength.

6.2 Comparison with other outflow studies

From our sample of 17 sources, 11 sources were studied before in outflow studies. The results for the outflow force are compared in Table 6. Since five of these sources are found in the study by Bontemps et al. (1996), a separate column is added. For the other sources, the reference is given in the last column.

In order to compare the results, the methods and observation properties of these studies have to be compared as well, since several assumptions will strongly underestimate or overestimate the outflow properties. This comparison is given in Table 7, where the resolution (velocity and spatial), the map size, rms noise, assumed distance and correction factors for opacity and inclination are listed. All of these properties are explicitly given for the sources from our sample. For example, the sample used by Bontemps et al. (1996) contains many more sources mapped in several resolutions and map sizes, but only the relevant values are listed here.

The better spatial resolution and noise levels of our study in comparison to the other studies tend to result in systematically higher values for the momentum flux. This is likely due to the determination of the maximum velocity, which is squared in the momentum flux and therefore quite significant. The maximum velocity is determined as the velocity where wing emission is still visible. This is strongly influenced by the noise and spectral resolution: the velocity is underestimated for high noise and low spectral resolution. Even when the spectral resolution is high, the low spatial resolution still decreases the momentum flux, as seen in the study by Sekimoto et al. (1997). Even with an exact opacity correction and applied inclination factors, the values found are still a factor of 5-10 lower than our values. This effect is most likely due to a very rough overestimate of the size R at this resolution (34”), considering that all outflows in Ophiuchus, except VLA 1623, are small.

The distance of 160 pc, as used in all studies before 2007, decreases the momentum flux value as well for

Table 6: *Comparison of the momentum flux between this study and other outflow studies.*

Source	$F_{\rm CO}^{\rm a}$	$F_{\rm CO}^{\rm b}$	$F_{\rm CO}^{\rm c}$	References[d]
	($10^{-6} M_{\odot}$ km s^{-1} yr^{-1})			
Elias 29	23	15±0.14	9.8,2.0	1,5
Elias 32/33	430	-	150	2
IRAS 16253-2429	4.1	-	-	
IRS 37	1.4	-	-	
IRS 43	7.4	15±1.2	-	-
IRS 44	29	27±3.1	30,3.4	3,5
IRS 46	17	-	-	-
IRS 54	19	-	-	-
IRS 63	6.8	6.3[e]	-	-
LFAM 26	90	-	16	1
RNO 91	45	-	3.0	4
WL 6	13	<15	2.5	5
WL 12	2.2	6.0±0.6	-	-
WL 17	0.5	-	-	-

a Result of this study

b Result of the study of Bontemps et al. (1996)

c Result of other studies (see last column)

d References: 1.Bussmann et al. (2007), 2.Kamazaki et al. (2003), 3.Terebey et al. (1989), 4.Arce & Sargent (2006), 5.Sekimoto et al. (1997)

e IRS 63 is named L1709B (name of the core) in Bontemps et al. (1996).

Table 7: Comparison of the methods and observation properties between this study and other outflow studies.

	This study	Bontemps et al. (1996)	Sekimoto et al. (1997)
^{12}CO line	3-2	2-1	2-1, 1-0
Sources[a]	All	EL 29, GSS 30, IRS 43, IRS 44, WL 6, WL 12	
Velocity res. (km/s)	0.1	0.65(NRAO), 0.26(IRAM)	0.06
Spatial res. (″)	15	30(NRAO), 10(IRAM)	34
Map size (″x″)	120x120	60x60(NRAO), 25x25(IRAM)	68x68
$\sigma_{\rm rms}$ (K)	0.15	0.25(NRAO), 0.15(IRAM)	0.2
Opacity corr.	none	mean of CB92[b]: 3.5	derived from ^{13}CO: $\sim$3.0(2-1)
Inclination corr.	factors CB92[b]	average i=57.3: factor 2.9	factors CB92
Distance to Oph (pc)	120	160	160
Other		Average off source spectrum subtracted before integration, integration radius 45″(IRS 44), 15″(others)	

	Kamazaki et al. (2003)	Bussmann et al. (2007)	Arce & Sargent (2006)
^{12}CO line	3-2, 1-0	3-2	1-0
Sources[a]	Elias 32/33	EL 29, LFAM 26	RNO 91
Velocity res. (km/s)	0.33(3-2), 0.41(1-0)	0.4	0.3
Spatial res. (″)	14	11	5
Map size (″x″)	120x240(OphB2)	300x300	100x100
$\sigma_{\rm rms}$ (K)	0.79(OphB2)	0.4	0.08
Opacity corr.	5.4[c]	none	none
Inclination corr.	average i=57.3: factor 2.9	none	none
Distance to Oph (pc)	160	120	160
Other			

a Only the sources that were studied for our sample are listed in this table.

b CB92 = Cabrit & Bertout (1992)

c The factor 5.4 is based on the mean factor 3.5 as used in Bontemps et al. (1996), multiplied by 1.6 because the optical depth of the 3-2 transition is 1.6 times larger than the 2-1 transition of the latter (Kamazaki et al. 2003).

Bontemps et al. (1996), Sekimoto et al. (1997), Kamazaki et al. (2003) and Arce & Sargent (2006) by a factor of 1.3, but this effect is not significant compared to the effects of the inclination and opacity corrections.

The sources studied by Bontemps et al. (1996) have a systematic offset in F_{CO} of one order of magnitude due to their inclination and opacity corrections. For Kamazaki et al. (2003), this is even a factor of 15. Without this offset, all values are a factor of 10 lower than the results of this study. The subtraction of the envelope profile systematically decreases the mass and also the momentum flux in the Bontemps values, but the values are most likely too low due to spatial resolution. One really significant difference between Bontemps et al. (1996) and our study is the momentum flux for Elias 29. This is mainly due to the coverage of the outflow map, since Bussmann et al. (2007) showed that the outflow was much more extended. The reason that our value for Elias 29 is still a factor of 2.5 higher than Bussmann et al. (2007), is probably the inclination correction. The partial coverage of our maps of Elias 29 only underestimates the momentum flux. The same arguments apply for the LFAM 26 source in the Bussmann study.

Clearly, the choice for inclination correction factors influences the outcome of momentum flux calculations. The method proposed by Bontemps et al. (1996), with a factor $f(i) = \frac{\sin i}{\cos^2 i}$ may significantly overestimate the momentum flux. This formula is based on the assumption that the actual velocity is $v_{\mathrm{CO}}/\cos i$ and the actual size $R_{\mathrm{CO}}/\sin i$, a simple projection effect. The choice of one single inclination value for the entire sample removes any accuracy for pole-on configurations. According to Cabrit & Bertout (1992), the inclination correction cannot be applied as a simple projection effect. First of all, the R_{CO} is not a narrow line, but a conical shape, so that the projection effect becomes smaller than $\cos i$. The flow velocity is even more complex, since outflows do not have a uniform velocity, neither directional nor as function of distance from the source. Two extremes can be chosen as the flow velocity: the maximum velocity extent the v_{CO}, as used in this study or the intensity-weighted velocity $< V >$. Since the latter is not easy to derive, Cabrit & Bertout (1992) derived correction factors with error estimates based on outflow models for calculations where v_{CO} is characterized as flow velocity. The correction factors with their errors and the $f(i)$ function are plotted in Figure 21. The correction factors by Cabrit & Bertout (1992) provide a more accurate correction than those by Bontemps et al. (1996), because they take the shape, velocity profile and opening angle into account.

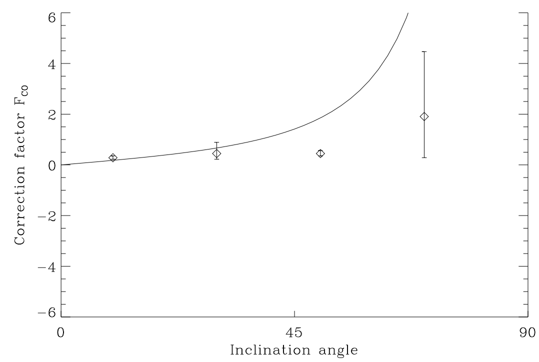

Figure 21: The inclination correction factors for the momentum flux, taken from Cabrit & Bertout (1992) (diamonds) and Bontemps et al. (1996) (line), the latter being a function $f(i)$. For the latter, an average inclination angle of 57° is used, resulting in a factor of 2.9. The correction factors from Cabrit & Bertout (1992) are clearly smaller than the $f(i)$ function for i >45°.

In order to compare and combine outflow studies, similar methods have to be applied, since results from the studies discussed in this section can differ more than one order of magnitude. Since opacity and inclination cause the largest uncertainties in the momentum flux, it is essential to derive these properties as accurate as possible.

6.3 Classification stages

All 16 sources classified as Stage 1 in van Kempen et al. (2009c) and the T Tauri star RNO 91 have been studied for outflow detection, with four classified as transitional towards Stage 2 (WL 17, WL 6, IRS 54

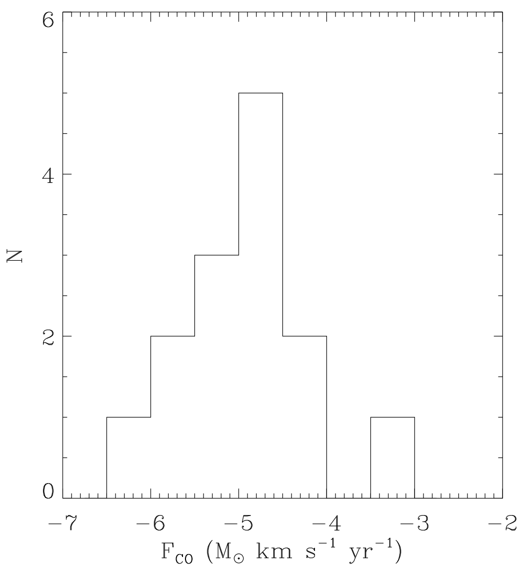

Figure 22: Histograms of momentum flux for all detected outflows.

and IRS 63). Out of this sample, all sources show a bipolar outflow activity, except for those that are so close to another YSO that their outflows are confused (GSS 30-IRS 1 and GSS 30-IRS 3 by VLA 1623; WL 3 and IRS 37; Elias 32 and 33). From the transitional sources, only the outflow WL 17 is clearly weak compared to the rest of the sample. The momentum flux does not reflect this transitional phase. Also the comparison with the two studied Stage 2 sources, IRS 46 and RNO 91, does not reflect a significant decrease of momentum flux, since these two sources have momentum fluxes higher than the mean of the entire sample. A study of Class 0, I and II objects (three of each) by Arce & Sargent (2006) and the comparison of three Class I and one Class II objects by Sekimoto et al. (1997) do not show a significant decrease of momentum flux in the Class II phase. Although the momentum flux decreases with evolution during the Class 0 and Class I phase, this decline does not appear to continue. The opening angle widens with evolution, causing the shape to become irregular for the Class II phase (Arce & Sargent 2006), making it more difficult to define an actual momentum flux, since the size is less clear. In contrast, IRS 46 seems to have quite a regular bipolar shape, although the opening angle could not be determined.

The spread in the outflow momentum flux for Stage 1 objects in Ophiuchus is broad (see the histogram in Figure 22) compared to a similar histogram for Perseus (Hatchell et al. 2007), ranging over four orders of magnitude. However, with exclusion of the strongest and the weakest source (Elias 33 and WL 17, respectively) the width of the distribution is only two orders of magnitude, just like the Perseus Class I distribution with their exclusion of high momentum flux sources. Hatchell et al. (2007) noted that the three high Class I sources in their sample lie in confused regions and therefore their flows may be overestimated. The exclusion of Elias 33 in our sample is not unreasonable, as discussed in the next paragraph. The outlier WL 17 cannot be explained. The spread of the momentum flux for sources with the same evolutionary state can be explained by physical reasons. The momentum flux is likely influenced by the amount of available material (e.g. the clump in which the protostar is formed) during the time that the driving wind or jet is active, the efficiency of the transfer of momentum from the wind to the ambient material, and the presence of other nearby outflows. The episodic jet ejection (Hatchell et al. 2007) may also be able to explain the spread. The swept-up molecular outflow smooths out any variability on timescales of $\sim$100 years according to the current models, but modification of these theories with our new results on the $F_{\rm CO} - L_{\rm bol}$ relation may extend these time scales, so that the effects are not smoothed out over such a short time scale and will actually be detectable. The histogram peaks at $10^{-5} M_\odot$ km s^{-1}yr^{-1}, while this peak is only $10^{-6.5} M_\odot$ km s^{-1}yr^{-1} for the Class I sources in Hatchell et al. (2007). This can partly be explained by the systematic underestimate by lack of inclination correction. Besides, the observations were of lower quality, with the large distance for Perseus (320 pc). Also, only 73% of the total sample of 51 sources show outflow activity according to this study.

The sources for which no outflow could be detected due to confusion with another nearby source should be explored a little further. Except for the GSS sources, which are clearly completely overlapped with the strong collimated VLA 1623 outflow, it is not trivial to determine which of the two sources is the driving force of the outflow. In this study, the driving source is determined based on morphology. The sources may even both have an outflow, which are blended in with each other or along the same line of sight. In that case, the total outflow mass (and the momentum flux) should be split up in a certain ratio, since the line wings form the sum of the line wings of two separate outflow. This suggestion applies to Elias 33, considering its very strong momentum flux compared to its stellar properties (envelope mass, bolometric luminosity). A better look at the spectrum (see Figure 6) shows a double structure in the line wings, especially the blue wing, with a high intensity inner wing and a lower intensity outer wing. Although this is possible for one single outflow with episodic jets, it may also indicate a sum of separate wings. There is however no accurate way to actually split these line wings into separate outflows since they are strongly blended with each other and with the envelope profile. For IRS 37 and WL 3, the momentum flux is not exceptionally strong, but the envelope mass for both is also >10 times smaller than Elias 33, suggesting a much more evolved YSO. Taking the evolution into account still does not suggest an exceptionally high momentum flux. The outflow is however confused due to the missing data in the south east corner. Observations without this lack of data will improve the possibilities to assign this outflow to either one of the sources.

Since all Stage 1 sources in Ophiuchus show outflow activity, the new classification provides a very good tool for characterizing young stellar objects, although the transitional phase (Stage 1 to Stage 2) is not reflected in the outflow strength. For YSOs grouped closely together, confusion of outflows results in a smaller amount of detections.

6.4 Comparison with disk studies

In star formation models, the outflow direction is perpendicular to the disk, since the jet which is driving the outflow is assumed to originate from the spinning up of the magnetic field by the rotating disk (Matsumoto & Tomisaka 2004). In the last decade, very high spatial resolution observations revealing the disk structure of early phase YSOs became available. The outflow results of this study were compared. IRS 46 has an outflow with a high inclination, consistent with an edge-on disk, as was determined by SED fitting to a disk model (Lahuis et al. 2006). Jørgensen et al. (2009) studied HCO^+ 3-2 and HCN 3-2 emission as a tracer of dense gas in the inner envelope for a sample of Class 0 and Class I sources in Taurus and Ophiuchus, including Elias 29, GSS30-IRS1, IRS 43, IRS 54, IRS 63 and WL 12 of our sample. Elias 29, IRS 43 and IRS 63 show red- and blue shifted material in opposite directions. The contour maps of these three sources as given in Figure 5 of Jørgensen et al. (2009) are presented in Figure 23. Elias 29 and IRS 63 were also observed at high spatial resolution by Lommen et al. (2008) and the velocity gradients were interpreted as Keplerian rotation in the inner envelope or circumstellar disk. Jørgensen et al. (2009) made the same interpretation for IRS 43. The velocity profiles observed by Jørgensen et al. (2009) for IRS 54 and WL 12 are too weak to conclude anything about the direction or orientation of the disk. GSS30-IRS1 displays emission extended from one side relative to the source position. Besides, our outflow observations of GSS30 are too confused by the Class 0 source VLA 1623, so this source is not further discussed.

The velocity gradient for IRS 63 is interpreted as a disk with 30° inclination with the edge in the north-south direction. This is the same angle as used for the outflow inclination: an edge-on disk (i=90°) means an outflow in the plane of the sky, a face-on disk (i=0°) means a pole-on outflow. The interpretation for IRS 63 fits quite well with our outflow result: the same inclination angle was assumed based on the contour map and a position angle of 70° for the outflow indicates a north-south oriented disk for this inclination.

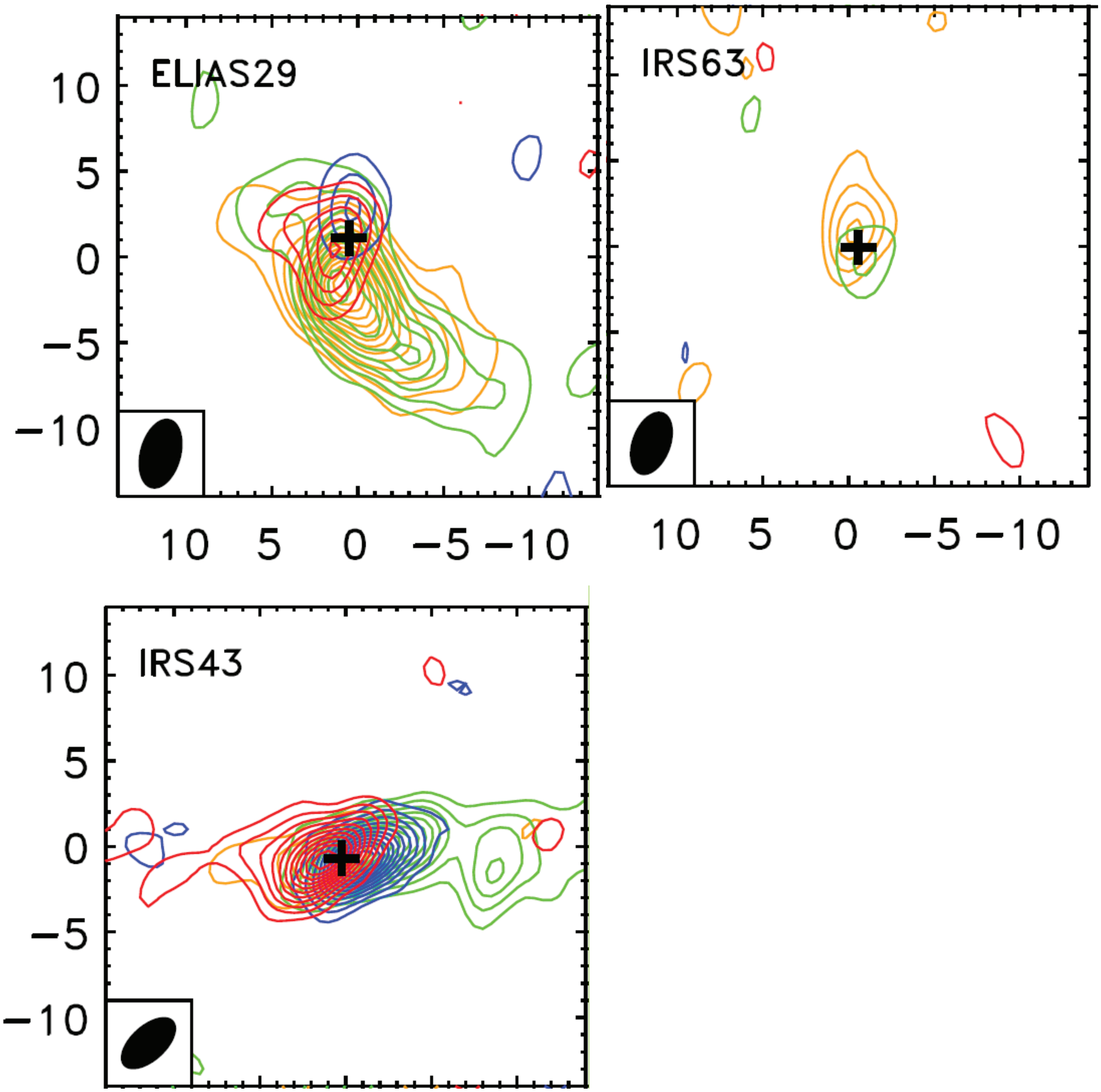

Figure 23: Contour maps of HCO$^+$ 3-2 emission from Elias 29, IRS 63 and IRS 43, taken from Jørgensen et al. (2009). The axes are RA and Dec offset positions in arcseconds. The contours (shown in 3σ intervals) indicate emission integrated over intervals from -4 to -2 km s^{-1} (blue), -2 to 0 km s^{-1} (green), 0 to 2 km s^{-1} (orange) and +2 to +4 km s^{-1} (red) relative to the systemic velocities.

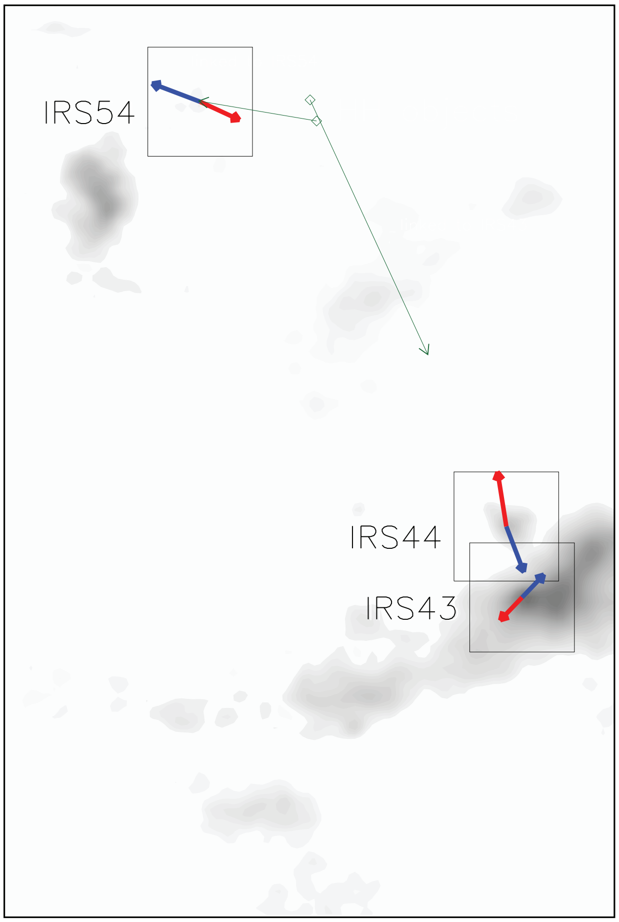

Figure 24: The nearby region of IRS 43 and IRS 44 and the Herbig Haro objects and direction as suggested by Grosso et al. (2001). The outflow directions are marked with blue and red arrows for the blue and red lobes, respectively. The HH objects are marked with green diamonds and green arrows point into the outflow direction, based on the structure of the combined HH objects (see Figure 2 in Grosso et al. (2001)). The left arrow points towards IRS 54, the right arrow towards IRS 43 and IRS 44.

The HCO^+ observations of Elias 29 were interpreted as a disk with 30° inclination (Lommen et al. 2008) with the edge in the north-north-west,south-south-east direction (direction based on Figure 5 in Jørgensen et al. (2009), not explicitly given). This is not entirely consistent with the outflow results: our rough assumption of 50° inclination is still acceptable, but the position angle of the outflow could be determined quite well as 150°, which is north-west,south-east, so nearly parallel with this disk direction. The HCO^+ observations of this source were confused by the presence of a dense ridge, which influences the interpretation. The most extreme red/blue-shifted velocities, indicated by red and blue contours, were interpreted as the tracer of Keplerian rotation by Jørgensen et al. (2009). However, since the direction and orientation of blue and red is equal to the outflow picture, these extreme velocities may actually be swept-up outflow material itself, indicating a small jet very close to the source.

IRS 43 was interpreted (Jørgensen et al. 2009) as a nearly edge-on disk ($i \sim$90°) with a position angle of -70° or west-north-west, east-south-east direction, further supported by the elongated structure of both continuum, HCO^+ and HCN emission, and the direction of nearby Herbig Haro objects (Grosso et al. 2001) and proposed radio thermal jet (Girart et al. 2000). However, this does not fit at all with the outflow result of an outflow nearly pole-on ($i \sim$10°) and a position angle of 135° or north-west, south-east direction. The position angle is a rough guess based on the contour map, since the outflow is nearly pole-on. Several results have to be reconsidered:

- The Herbig Haro objects may not be associated with IRS 43, as claimed by Grosso et al. (2001), but with IRS 44, which is also close by and whose outflow actually points in the right direction. This is shown in Figure 24 and also discussed in Section 6.7.
- It is possible that the CO lines trace the inner, rotating part of envelope just as well as the HCO^+. The CO spectra in the central region are decreasing radially, which is indicative of Keplerian rotation. However, the limited spatial resolution has an important role here. Also the PV diagrams in CO (Figure 4) and HCO^+ (Jørgensen et al. 2009) show similarity.
- If the swept-up material as observed in the contour map in Figure 7 does not trace the outflow and the outflow is in the north-east south-west direction, this real outflow is not observed in CO. However, this may simply be a projection effect: if the disk is nearly edge-on, the outflow will be nearly in the plane of the sky and the wing emission will coincide with the envelope emission because the projected velocity is too small. It may be possible to trace the wing emission as an excessive emission in the envelope spectral profile in lines that are optically thin in the envelope.
- Girart et al. (2000) were not entirely conclusive about the thermal jet VLA1 and suggested some other scenarios, although all of them less likely.
- Brinch et al. (2007) proposed a model for L1489 IRS with a disk inclination of 40° and a surrounding envelope inclination of 74°. They suggested a binary system to explain this misalignment. IRS 43 is observed as a binary radio source with a separation of only 0.6″ (Girart et al. 2000). If a similar model as for L1489 IRS applies for IRS 43, the HCO^+ emission would trace the inner envelope, but not the actual disk.

Summarizing the discussion above, interpreting observations from the inner envelope and disk remains difficult since many aspects have to be taken into account. Especially IRS 43 turns out to be a very special source, with a complex envelope structure. Higher resolution mapping of the inner part of envelope will be necessary to properly interpret the observed velocity structures.

6.5 Outflow direction

For the L1688 part of Ophiuchus, we compare the outflow directions for the different sources. Since these sources are clustered together, they may have experienced the same trigger from the same direction for the core formation and the following star formation. For L1688, the orientation can be divided in three groups: IRAS 16253-2429, IRS 54, IRS 37, WL 6, IRS 44 and IRS 46 are all oriented in a north-east, south-west direction. We may add IRS 43 to this sample, since the orientation of the disk and the radio continuum observations (see Section 6.4) also suggest a north-east, south-west orientation, although we did not observe this in the outflow study. We may even add UFO 2 (near IRS 37), UFO 4 (near IRS 54) and UFO 5 (near IRS 44) to this sample, which are well enough covered to derive their orientation. The second group contains the sources with a north-west, south-east direction: Elias 33, VLA 1623, WL 12 and possibly Elias 29. Finally, the third group contains LFAM 26, with an east-west orientation, although this outflow is so close to Elias 29 that both of their outflow directions are confused, and WL 17, which is very weak and possibly confused as well by the Elias 29/LFAM 26 system. The direction of the first group confirms the results of Anathpindika & Whitworth (2008), who concluded that the outflow direction is in 72% of the cases perpendicular to the filament direction. The implication is the angular momentum delivered to a core forming in a filament, since the angular momentum will eventually drive the outflow. The Ophiuchus ridge in the south is indeed perpendicular to the outflow direction of the first group.

The fact that there are two groups with on average an equal direction, suggests that there have been two separate triggering events causing the star formation. Considering the large values for $L_{\rm bol}$ and $M_{\rm env}$ for the second group compared to the first group (mean of 1.84 $L_{\odot}$ and $0.38M_{\odot}$ versus $0.56L_{\odot}$ and $0.044M_{\odot}$) these two groups may have started star formation at different times, due to different events. This is consistent with the observation of Zhang & Wang (2009) that the star formation in Ophiuchus first took place in the denser northwestern L1689 region. It is further consistent with the suggestion that star formation in Ophiuchus was triggered by ionization fronts and winds from the Upper Scorpius OB association, which is located to the west of the Ophiuchus cloud (Nutter et al. 2006).

6.6 UFOs

The UFOs are newly detected outflows which could not be assigned to a known young stellar object. The partial coverage of these outflows extends the field in which to look for a suitable candidate. First we look at the L1709 field near IRS 63, with UFO 1 and UFO 7.

- In the south west direction, about 2 arcminutes from IRS 63 a submillimeter core (850 μm) is located (SMM J 163133-24032, Jørgensen et al. (2008)) at 16:31:32.8, -24:03:16.91. A likely corresponding YSO candidate observed by Spitzer is SSTc2d J163134.2-240325 (Padgett et al. 2008) or EDJ2009-988 (Evans et al. 2009) at 16:31:34.29, -24:03:25.2, so 24″ offset from the core position. The composition of the different objects is given in Figure 25. This source may be the powering source of UFO 1. $L_{\rm bol}$ is 0.88, $T_{\rm bol}$ is 870 K and $\alpha_{\rm IR}$ is -0.12 (Evans et al. 2009) (flat spectrum, between Class I and II) and with a momentum flux of $1.5{\cdot}10^{-6}M_{\odot}$ km s^{-1}yr^{-1} this may indeed be a Class I source with an outflow. This protostellar system also follows the derived $F_{\rm CO}$-$L_{\rm bol}$ relation. All observed fluxes and derived bolometric luminosities are given in Table 8 and 9.
- For UFO 7, selecting a candidate is somewhat more difficult, since only a small piece of the red lobe is covered and therefore the direction of the originating source is unknown. Figure 25 shows two possibilities: in the north east direction a submillimeter core is located at 16:31:43.7, -24:00:27.1 (J163143.5-240026, Di Francesco et al. (2008)), at a distance of 134″ from IRS 63. However, no IR source has been found at this location. Since the outflow can also be directed towards the south east, another possible candidate is the YSO candidate SSTc2d 163144.5-240212 (Padgett et al. 2008) or EDJ2009-992 (Evans et al. 2009) at 16:31:44.57,-24:02:13.0. $L_{\rm bol}$ is 0.72, $T_{\rm bol}$ is 3100 K and $\alpha_{\rm IR}$ is -0.94 (Evans et al. 2009) (Class II). SEDs of UFO 1 and UFO 7 are provided in Evans et al. (2009).
- UFO 2 is located to the west of IRS 37. The elongated structure and direction of the outflow

suggest that the powering source is located in the south west. A large submillimeter core is located at 16:27:12.7, -24:29:50 (J162712.4-242950, Di Francesco et al. (2008)), see also Figure 26. The shape of this submillimeter ridge is consistent with the outflow direction, which is often found to be perpendicular to the ridge (Anathpindika & Whitworth 2008). The fluxes for 850 μm and 450 μm, taken from Di Francesco et al. (2008) are given in Table 8. No IR source was found near this location. A small-aperture photometry study of IRAC and MIPS data shows that there is indeed no significant detection above 1 mJy for any wavelength at this position. Therefore, an approximate SED was made based on the submillimeter fluxes (Figure 27) as described in the next paragraph.

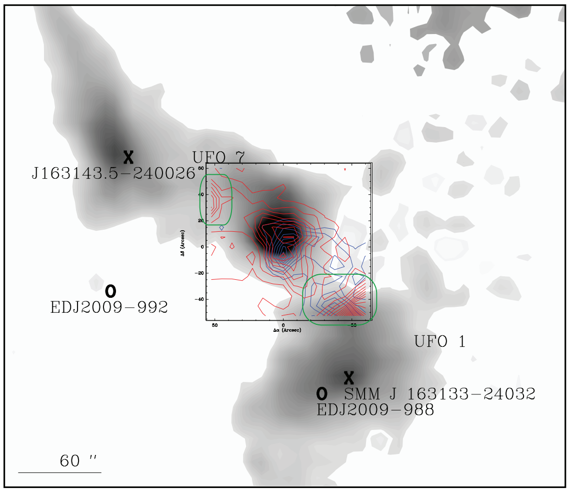

Figure 25: The region around IRS 63, showing the SCUBA 850 μm emission in the background, the contour map of the integrated line wings, and the location of the possible powering sources of UFO 1 and UFO 7 marked by crosses (submm cores) and circles (IR sources). The covered parts of UFO 1 and UFO 7 itself are encircled with a green rectangle. Note that both of these outflows are only partly covered.

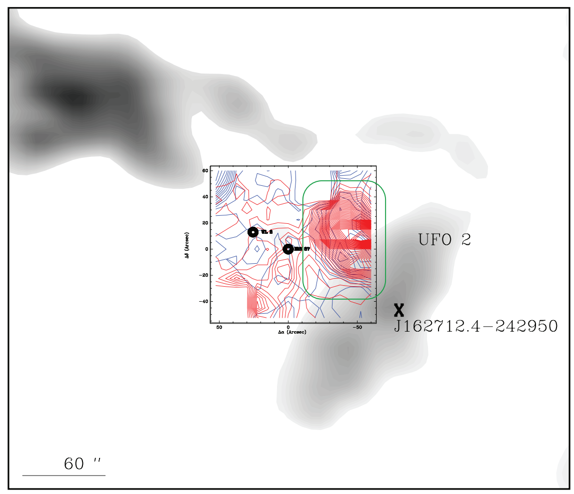

Figure 26: The region around IRS 37, showing the SCUBA 850 μm emission in the background, the contour map of the integrated line wings, and the location of the possible powering source of UFO 2 marked by a cross (submm core). The covered parts of UFO 2 itself is encircled with a green rectangle. No IR source was found at this location.

- The outflow UFO 3 is very clearly visible in the WL 12 contour map. The center of origin is about 16:26:40, -24:35:27. Unfortunately, there are no submillimeter cores, IR sources or YSO candidates nearby. Estimates of a SED or $L_{\rm bol}$ are impossible to achieve.

- UFO 4 has its lobes at opposite sides of IRS 54, so its powering source is most likely in the line of sight or even confused with IRS 54 and therefore impossible to detect.
- UFO 5 is located to the west of IRS 44. Towards the south-west, an elongated structure of submillimeter emission can be seen (Figure 28). This structure can be split up by looking for the two peaking profiles. The core in the north west, centered at 16:27:22.3, -24:40:02 is the most likely candidate source for UFO 5 (J162721.7-244002, Di Francesco et al. (2008)). However, just like UFO 2, there is no IR detection at this position. Again, an estimate of the SED was made based on the submillimeter fluxes, further described below.
- Only a small part of UFO 6 is covered, just like UFO 7 it is impossible to the determine the direction of a potential origin source. The IRS 44 region is actually very crowded with YSO candidates and of course the YSOs IRS 43 and IRS 46 nearby, as can be seen in Figure 28, where candidate YSOs are marked with white crosses. Two candidates for UFO 6 are EDJ-2009 918 and 921, both YSO candidates with $\alpha_{\rm IR}$ ~-0.6 (Evans et al. 2009), or Class II sources. It is however impossible to be entirely conclusive about the powering source.

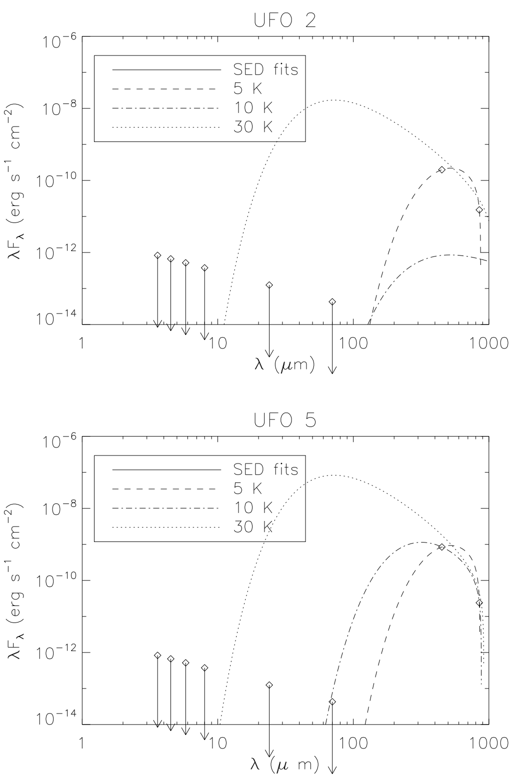

Figure 27: The spectral energy distributions of UFO 2 and UFO 5, based on their submillimeter fluxes and upper limits for the IR fluxes.

SED estimates for UFO 2 and UFO 5 were made based on the submillimeter fluxes for 3 temperatures: 5, 10 and 30 K, as shown in Figure 27. The SED function to be fitted is:

$$\lambda F_\lambda = A + B \frac{2\,h\,c^2}{\lambda^4} \frac{1}{e^{\frac{hc}{\lambda k T}} - 1} \tag{16}$$

This is the well known Planck formula expressed in wavelength. A and B are the constants to be fitted. Considering the low upper limits for the IR fluxes, the flux for UFO 2 is best fitted for a SED at 5 K, while UFO 5 can be fitted for both 5 and 10 K. The total fluxes were calculated using $F = \int \frac{\lambda \cdot F_\lambda}{\lambda} d\lambda$. It follows that $F = 2.8 \cdot 10^{32}$ erg s^{-1} for UFO 2 for 5 K, and $F = 1.2 \cdot 10^{33}$ and $2.1 \cdot 10^{33}$ erg s^{-1} for UFO 5 at 5 and 10 K, respectively. With $L_{\rm bol} = 4\pi D^2 \cdot F$ and a distance of 120 pc, the luminosities are 0.074, 0.31 and 0.54 $L_\odot$. The luminosities are not particularly low compared to the Class I sources in our sample, but the very low temperatures and lack of IR detection indicate that these sources are likely Class 0 objects.

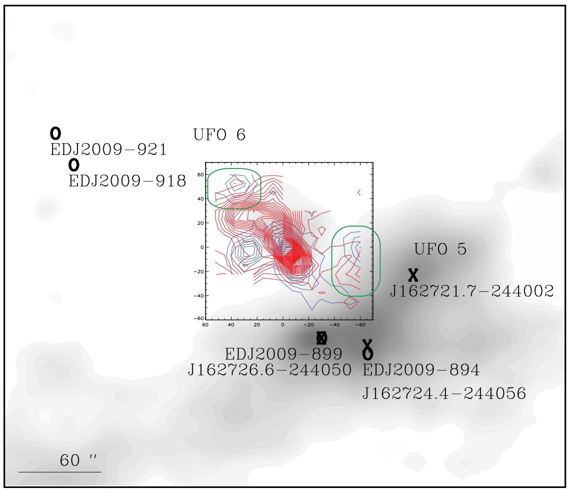

Figure 28: The region around IRS 44, showing the SCUBA 850 μm emission in the background, the contour map of the integrated line wings, and the location of the possible powering source of UFO 5 and UFO 6 marked by crosses (submm cores) and circles (IR sources). The covered parts of UFO 5 and UFO 6 itself are encircled with a green rectangle. Since no definite powering source was chosen, all detected sources that are close by are marked.

The UFOs are clearly very peculiar objects. Only one UFO (UFO 1) could be assigned to a YSO without many uncertainties. UFO 6 and UFO 7 may be assigned to a YSO with actual IR detection, but a larger spatial coverage of these outflows is necessary in order to decide on their shape and center of origin. Most interesting are the UFOs for which no IR powering source could be found, UFO 2, 3 and 5. This lack of detection suggests either a *very* low luminosity or a totally new kind of object, producing an outflow or some other mechanism producing swept-up gas. The derived luminosities based on the submillimeter fluxes for these sources are not particularly small, but considering the very low temperature of the SED these are not ordinary YSOs. Again for these sources, a better spatial coverage of CO low-J lines with higher resolution may provide an answer. Also HCO^+ or another high-density tracer may help to determine the structure of the envelope.

6.7 H_2 knots and Herbig Haro objects

Besides CO line observations, there are other methods to detect outflows. One example is the detection of Herbig-Haro (HH) objects. Outflowing material from YSOs may interact with the surrounding material and result in the development of shocks. After the shock, the gas cools down by line radiation, e.g. Hα or [S II] (optical). Extended regions radiating in these lines but lacking continuum emission, are called Herbig-Haro objects (Phelps & Barsony 2004). Ophiuchus has been mapped in [S II] surveys several times, the most recent study was performed by Phelps & Barsony (2004).

Table 8: Fluxes from possible source candidates (submm cores) for the UFOs, taken from literature.

Outflow	Region	Submm core	Coordinates core (J2000)	Fluxes (mJy) 450μm	850μm
UFO 1	IRS 63	SSM J163133-24032	16:31:32.8, -24:03:16.91	-	1600[a]
UFO 2	IRS 37	J162712.4-242950	16:27:12.7, -24:29:50	30000[b]	4300[b]
UFO 3	WL 12	-	-	-	-
UFO 4	IRS 54	Origin of outflow confused by IRS 54			
UFO 5	IRS 44	J162721.7-244002	16:27:22.3, -24:40:30	130000[b]	6800[b]
UFO 6	IRS 44	Unable to determine direction of potential source due to small coverage			
UFO 7	IRS 63	J163143.5-240026	16:31:43.7,-24:00:27.1	87000[b]	3900[b]

a Jørgensen et al. (2008)

b Di Francesco et al. (2008)

Table 9: Fluxes from possible source candidates (IR sources) for the UFOs, taken from literature.

Outflow	Region	IR source candidate	Coordinates (J2000)	Fluxes (mJy) 3.6μm	4.5μm	5.8μm	8.0μm	24μm	70μm
UFO 1	IRS 63	EDJ2009-988	16:31:34.29, -24:03:25.2	270[a]	340[a]	510[a]	600[a]	720[a]	-
UFO 2	IRS 37	-	-	<1	<1	<1	<1	<1	<1
UFO 3	WL 12	-	16:26:40, -24:35:27[b]	<1	<1	<1	<1	<1	<1
UFO 4	IRS 54	Origin of outflow confused by IRS 54							
UFO 5	IRS 44	-	-	<1	<1	<1	<1	<1	<1
UFO 6	IRS 44	Unable to determine direction of potential source due to small coverage							
UFO 7	IRS 63	EDJ2009-992	16:31:44.57,-24:02:13.0[c]	87[a]	98[a]	120[a]	270[a]	640[a]	-

a Evans et al. (2009)

b The coordinates are an estimate of the origin of the outflow UFO 3, there is no IR source candidate.

c The IR source is a different candidate than the submillimeter core, see text.

Another method is the observation of H_2 knots in the near-infrared, tracing shock-excited knots and jets. An interesting property of H_2 knots is that they are often shaped in the shock direction, e.g. a bow shape following a bow shock, although optical HH objects can also have a bow shock shape. H_2 maps of small regions of Ophiuchus have been taken before, but the most recent study covered the entire L1688 area (Khanzadyan et al. 2004). In this study, the H_2 knots were not only compared to known outflows and potential candidate YSOs, but also to the HH objects as studied by Phelps & Barsony (2004).

Combining the results for Herbig-Haro objects, H_2 knots and our CO outflow results provides more insight in the outflow activity in Ophiuchus. The results are plotted in Figure 29. In this map, suggested outflow directions by Khanzadyan et al. (2004) (purple) and Phelps & Barsony (2004) (light blue) are drawn as well. From this map it becomes clear that many of the HH and H_2 objects can be associated with the newly detected outflows. Only sources from our sample are drawn: several of the HH and H_2 knots are already associated with a driving source, although not all of these sources are in the map.

- The newly discovered outflow of IRAS 16253-2429 follows the H_2 knots and its elongated direction perfectly, so these can definitely be associated with the YSO. Khanzadyan et al. (2004) suggest that the discovered Class 0 source MMS126 (Stanke et al. 2006) is located at this position as well and responsible for the outflow and H_2 knots, but it was decided in this study to associate the outflow to the Class I source IRAS 16253-2429, due to its outflow strength. The HH object HH 417 located towards the north is also along the line of sight of the IRAS 16253 outflow, but considering the distance of 9′ they may not be related.

- The outflow of IRS 54 is also perfectly coinciding with the H_2 knots, confirming the suggestion by Khanzadyan et al. (2004). The double HH object towards the north (HH 677) may be related to UFO 4, being in a north-south orientation.

- The WL 6 outflow direction is NE-SW, confirming the suggestion (Khanzadyan et al. 2004) that two of the H_2knots in the 'clump' south west of WL 6 are connected to this source, also including the H_2 knot in the north east of WL 6. The clump may be related to UFO 2, although the outflow would be very extended in that case (over 4′). The other H_2 knot in the north east is probably not related to WL 6, considering its NW directed bow shape.

- To the east of LFAM 26, two H_2 knots with a bow shock shape towards the south west direction lie along the line of the western lobe of LFAM 26. The two HH objects in this region were suggested to be linked to a flow in the NE-SW direction (Phelps & Barsony 2004), but lacking an outflow in this direction and the orientation of the bow shape it is more likely that the HH objects are related to the LFAM 26 lobe in the NE-SW direction. This confirms the connection as proposed by Khanzadyan et al. (2004).

- In the region with IRS 43 and IRS 44, two parallel flows are suggested in the NE-SW direction originating from these two YSOs. Although they do not exactly line up with IRS 44, the direction of this outflow is not completely certain, since the map was confused by the nearby outflow of IRS 46 and two UFOs from which the direction can not be derived without larger spatial coverage. The outflow direction of IRS 43 was discussed extensively in Section 6.4: the CO arrows may not be tracing the outflow. The third arrow (to the west of IRS 43 and 44) connects two H_2 knots and may follow the direction of UFO 5 although this cannot be confirmed without a larger spatial coverage. The presence of the nearby UFOs confuses the area, so we suggest to map this region first over a larger area before concluding anything.

Several suggestions by Khanzadyan et al. (2004) for linking HH objects and H_2 knots to protostars could be confirmed with the new outflow observations. However, in order to connect all objects to driving outflows, the entire L1688 region should be

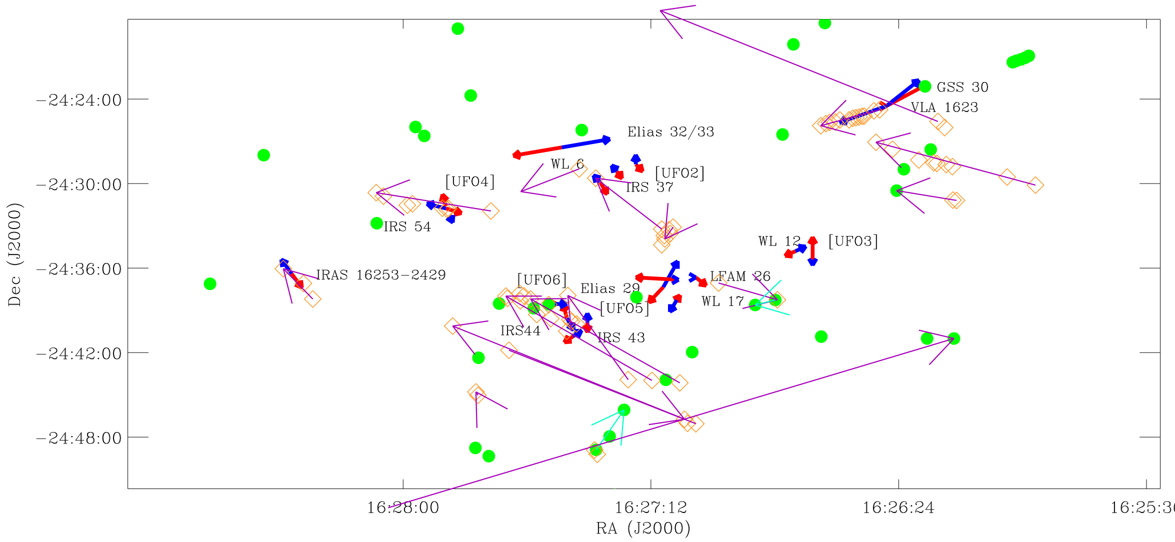

Figure 29: Overview of the outflow activity in L1688. The CO outflows as found in this study are marked with blue and red arrows, the same as Figure 1 and names of the sources are added. The UFOs are included as well. HH objects taken from Phelps & Barsony (2004) are labeled with green circles, H_2 knots taken from Khanzadyan et al. (2004) are labeled with orange diamonds. Purple arrows indicate the outflow directions as proposed by Khanzadyan et al. (2004), based on the shape of the H_2 knots and the alignment of sources, HH objects and H_2 knots. Light blue arrows indicate suggested directions as proposed by Phelps & Barsony (2004), based on the HH objects.

mapped by a direct outflow tracer such as low-J CO lines, as recently performed for Perseus (Curtis et al. 2010). Since Class II sources also show outflow activity, and possibly even very cold cores (the UFOs), a lot of outflow activity is to be expected, also considering the amount of unlinked HH objects and H_2 knots.

7 Conclusions

We have searched for molecular outflows towards all 16 Stage 1 sources in Ophiuchus as classified by van Kempen et al. (2009c) and in addition studied the T Tauri star RNO 91. The main results of this study are the following:

1. All sources show a bipolar outflow activity, except for those that are so close to another source that their outflows are confused. Therefore, the classification in Stages based on physical properties provides a very good tool for characterizing young stellar objects, although the transitional phase (Stage 1 to Stage 2) is not reflected in the outflow strength. Five outflows assigned to a Stage 1 source were new detections.

2. The well-known correlation of momentum flux with bolometric luminosity could not be extended to the three lowest luminosity sources ($L_{\rm bol} < 0.5 L_\odot$) in this study. Instead, the momentum flux becomes constant for these luminosities. Although the reliability of the calculated values for these three sources is somewhat debatable, the break suggests that the accretion rate may not be directly related to the outflow strength, as previously thought. Episodic accretion is a likely possibility to explain this phenomenon. The correlations of momentum flux with envelope mass and with dense gas as traced by HCO^+ are present, confirming a decline of outflow strength with evolution.

3. Comparing the outflow observations for three sources with recently obtained disk studies (Jørgensen et al. 2009) leads to revision of these

disk structures. IRS 63 shows an excellent agreement for the disk orientation (perpendicular to the outflow direction), but for Elias 29 the assumed disk emission is most likely originating from the outflow material itself, close to the source, consistent with non detection in millimetre continuum at long baselines. IRS 43 is even more complex: the assumed outflow direction is inconsistent with the disk orientation, suggesting that the ^{12}CO emission actually traces large scale rotation in the envelope.

4. The outflows in the L1688 region can be divided into two groups, based on preferred outflow direction and significantly different evolutionary properties. This suggests a scenario with star formation in two separately triggered events, starting in the north west, supporting conclusions from previous work, i.e. Zhang & Wang (2009).

5. Seven new outflows (UFOs) were detected which could not be assigned to a nearby confirmed YSO. Due to the small spatial coverage of these outflows, assigning candidate IR sources was only possible for three outflows. For two others, the only suitable candidates were submillimeter cores without IR detection, suggesting very young and deeply embedded sources. For the final two outflows, no candidate was found.

6. Mapping H_2 knots and HH objects in L1688 together with the outflow directions, confirm several suggestions from Khanzadyan et al. (2004) to link these objects to outflows.

For further outflow studies, it is recommended to focus on low luminosity objects ($L_{\rm bol} < 0.5 L_\odot$) to confirm the $F_{\rm CO} - L_{\rm bol}$ relation as found in this study. For Ophiuchus studies we suggest to map the entire L1688 region by low-J CO lines, as recently performed for Perseus (Curtis et al. 2010). This provides a more complete view of outflow activity, both for known as for new sources (such as the UFOs) and a more complete view of outflows from Stage 2 sources. Furthermore, the envelope surrounding IRS 43 should be explored in very high spatial resolution in order to understand the complex velocity structure.

References

Anathpindika, S. & Whitworth, A. P. 2008, A&A, 487, 605

Andre, P. & Montmerle, T. 1994, ApJ, 420, 837

Andre, P., Ward-Thompson, D., & Barsony, M. 2000, Protostars and Planets IV, 59

Arce, H. G. & Sargent, A. I. 2006, ApJ, 646, 1070

Avery, L. W., Hayashi, S. S., & White, G. J. 1990, ApJ, 357, 524

Bachiller, R. & Perez Gutierrez, M. 1997, ApJ, 487, L93+

Bachiller, R. & Tafalla, M. 1999, in NATO ASIC Proc. 540: The Origin of Stars and Planetary Systems, ed. C. J. Lada & N. D. Kylafis, 227–+

Beckford, A. F., Lucas, P. W., Chrysostomou, A. C., & Gledhill, T. M. 2008, MNRAS, 384, 907

Bontemps, S., Andre, P., Terebey, S., & Cabrit, S. 1996, A&A, 311, 858

Boogert, A. C. A., Hogerheijde, M. R., Ceccarelli, C., et al. 2002, ApJ, 570, 708

Brinch, C., Crapsi, A., Jørgensen, J. K., Hogerheijde, M. R., & Hill, T. 2007, A&A, 475, 915

Bussmann, R. S., Wong, T. W., Hedden, A. S., Kulesa, C. A., & Walker, C. K. 2007, ApJ, 657, L33

Cabrit, S. & Andre, P. 1991, ApJ, 379, L25

Cabrit, S. & Bertout, C. 1990, ApJ, 348, 530

Cabrit, S. & Bertout, C. 1992, A&A, 261, 274

Ceccarelli, C., Boogert, A. C. A., Tielens, A. G. G. M., et al. 2002, A&A, 395, 863

Chen, H., Myers, P. C., Ladd, E. F., & Wood, D. O. S. 1995, ApJ, 445, 377

Crapsi, A., van Dishoeck, E. F., Hogerheijde, M. R., Pontoppidan, K. M., & Dullemond, C. P. 2008, A&A, 486, 245

Curtis, E. I., Richer, J. S., Swift, J. J., & Williams, J. P. 2010, ArXiv e-prints

Dent, W. R. F., Matthews, H. E., & Walther, D. M. 1995, MNRAS, 277, 193

Di Francesco, J., Johnstone, D., Kirk, H., MacKenzie, T., & Ledwosinska, E. 2008, ApJS, 175, 277

Evans, N. J., Dunham, M. M., Jørgensen, J. K., et al. 2009, ApJS, 181, 321

Furuya, R. S., Kitamura, Y., Wootten, A., Claussen, M. J., & Kawabe, R. 2003, ApJS, 144, 71

Gagné, M., Skinner, S. L., & Daniel, K. J. 2004, ApJ, 613, 393

Girart, J. M., Rodríguez, L. F., & Curiel, S. 2000, ApJ, 544, L153

Greene, T. P., Wilking, B. A., Andre, P., Young, E. T., & Lada, C. J. 1994, ApJ, 434, 614

Grosso, N., Alves, J., Neuhäuser, R., & Montmerle, T. 2001, A&A, 380, L1

Gurney, M., Plume, R., & Johnstone, D. 2008, PASP, 120, 1193

Hatchell, J., Fuller, G. A., & Richer, J. S. 2007, A&A, 472, 187

Hogerheijde, M. R., van Dishoeck, E. F., Blake, G. A., & van Langevelde, H. J. 1998, ApJ, 502, 315

Johnstone, D., Wilson, C. D., Moriarty-Schieven, G., et al. 2000, ApJ, 545, 327

Jørgensen, J. K., Johnstone, D., Kirk, H., et al. 2008, ApJ, 683, 822

Jørgensen, J. K., van Dishoeck, E. F., Visser, R., et al. 2009, A&A, 507, 861

Kamazaki, T., Saito, M., Hirano, N., & Kawabe, R. 2001, ApJ, 548, 278

Kamazaki, T., Saito, M., Hirano, N., Umemoto, T., & Kawabe, R. 2003, ApJ, 584, 357

Khanzadyan, T., Gredel, R., Smith, M. D., & Stanke, T. 2004, A&A, 426, 171

Lahuis, F., van Dishoeck, E. F., Boogert, A. C. A., et al. 2006, ApJ, 636, L145

Leous, J. A., Feigelson, E. D., Andre, P., & Montmerle, T. 1991, ApJ, 379, 683

Loinard, L., Torres, R. M., Mioduszewski, A. J., & Rodríguez, L. F. 2008, ApJ, 675, L29

Lommen, D., Jørgensen, J. K., van Dishoeck, E. F., & Crapsi, A. 2008, A&A, 481, 141

Loren, R. B. 1989, ApJ, 338, 902

Matsumoto, T. & Tomisaka, K. 2004, ApJ, 616, 266

Nutter, D., Ward-Thompson, D., & André, P. 2006, MNRAS, 368, 1833

Padgett, D. L., Rebull, L. M., Stapelfeldt, K. R., et al. 2008, ApJ, 672, 1013

Phelps, R. L. & Barsony, M. 2004, AJ, 127, 420

Richer, J. S., Shepherd, D. S., Cabrit, S., Bachiller, R., & Churchwell, E. 2000, Protostars and Planets IV, 867

Robitaille, T. P., Whitney, B. A., Indebetouw, R., Wood, K., & Denzmore, P. 2006, ApJS, 167, 256

Sekimoto, Y., Tatematsu, K., Umemoto, T., et al. 1997, ApJ, 489, L63+

Snell, R. L., Loren, R. B., & Plambeck, R. L. 1980, ApJ, 239, L17

Stanke, T., Smith, M. D., Gredel, R., & Khanzadyan, T. 2006, A&A, 447, 609

Terebey, S., Vogel, S. N., & Myers, P. C. 1989, ApJ, 340, 472 van Kempen, T. A., van Dishoeck, E. F., Güsten, R., et al. 2009a, A&A, 501, 633

van Kempen, T. A., van Dishoeck, E. F., Hogerheijde, M. R., & Güsten, R. 2009b, A&A, 508, 259

van Kempen, T. A., van Dishoeck, E. F., Salter, D. M., et al. 2009c, A&A, 498, 167

Whitney, B. A., Wood, K., Bjorkman, J. E., & Cohen, M. 2003, ApJ, 598, 1079

Wilking, B. A., Gagné, M., & Allen, L. E. 2008, Star Formation in the ρ Ophiuchi Molecular Cloud, ed. Reipurth, B., 351–+

Wilson, T. L. 1999, Reports on Progress in Physics, 62, 143

Wilson, T. L. & Rood, R. 1994, ARA&A, 32, 191

Yu, T. & Chernin, L. M. 1997, ApJ, 479, L63+

Zhang, M. & Wang, H. 2009, AJ, 138, 1830